Heavy Ion-, Pulsed Laser-, and Focused X-Ray-Induced Single Event Transients: An Exploration of Charge Collection Mechanisms in an Epitaxial Silicon Diode

By

Kaitlyn Lyle Ryder

Dissertation
Submitted to the Faculty of the
Graduate School of Vanderbilt University
in partial fulfillment of the requirements
for the degree of
DOCTOR OF PHILOSOPHY
In
Electrical Engineering
June 30, 2021
Nashville, Tennessee

Approved:

Robert A. Reed, Ph.D
Sharon M. Weiss, Ph.D
Ronald D. Schrimpf, Ph.D
Andrew L. Sternberg, Ph.D
Sokrates T. Pantelides, Ph.D

To Naja McCutchen and Monroe Moore.

"Space is big. Really big."

-The Hitchhiker's Guide to the Galaxy

ACKNOWLEDGEMENTS

This work would not have been possible without the support, encouragement, and collaboration of my colleagues, both past and present. Thank you to all current RER graduate students for your support, encouragement, and camaraderie. Special thanks to current graduate students Rachel Brewer and Brandon Smith for listening to my rants on electric fields and potential modulation at all hours of the night and continuing to be my friends anyway. To past graduate students Isaak Samsel, Charles Arutt, Rebekah Austin, and Andrew Tonigan, thank you for your guidance and mentorship, and for helping learn how to navigate the murky waters of graduate school.

Thank you to the faculty and staff of the RER group for the work and guidance you provided. Thank you to Enxia Zhang for all your help in preparing and packaging my devices for testing; without you there would be no experimental results. Thank you to Mike McCurdy for everything you do to make testing trips happen, from shipping the equipment to-and-fro to collaborating with the facilities to make sure everything is where it needs to be. Special thanks to Dr. Weller for your enthusiasm and encouragement and friendship.

Scientific exploration could not happen without financial support. I would like to thank to various funding agencies who have made this work happen: to the Defense Threat Reduction Agency, to Sandia National Labs, and to the NASA Electronics Parts and Packaging Program.

Special thanks to my committee members for all their support and advice. Thank you Dr. Pantelides for always asking the hard questions and keeping me on my toes. To Dr. Schrimpf, thank you for sharing your expertise on band diagrams. Thank you to Dr. Sternberg for all the conversations in the lab and introducing me to VEX robotics. Thank you, Dr. Weiss, for your expertise on optics and for keeping the meetings somewhat on topic. Special thanks to my advisor, Dr. Reed, for your advice and guidance, for the opportunities you provided me, and for sharing pizza with me one fateful testing trip at a proton facility in Hampton, VA.

Thank you to my friends and family who have supported me throughout my academic career, and to my parents, David and Lisa Lyle, who have always encouraged me to pursue my dreams. Finally, my heartfelt thanks to my supportive husband and colleague, Landen Ryder. Without you, this work would not exist; thank you.

TABLE OF CONTENTS

Page

ACKNOWLEDGEMENTS iv

LIST OF TABLES vii

LIST OF FIGURES viii

Chapter

INTRODUCTION 1

BACKGROUND 5

A. **Space Radiation Environment** 5

B. **Single Event Effects** 7

GROUND-BASED SEE TESTING METHODS 12

A. **Heavy Ions** 12

B. **Pulsed Lasers** 15

C. **Focused X-Rays** 18

D. Current State of Correlating Radiation Sources 20

SETUP AND PROCEDURES 22

A. **Experimental Setup** 22

1) *Diode Test Structure* 22

2) *Experimental Conditions* 23

B. **Data Processing Methodology** 31

C. **Simulation Device, Setup, and Models** 33

EXPERIMENTAL RESULTS FOR EACH RADIATION SOURCE 37

A. **Heavy Ion** 37

B. **Pulsed Laser** 43

C. **Focused X-Ray** 52

COMPARISON OF RESULTS FROM DIFFERENT RADIATION SOURCES 59

A. **Comparison of Sensitive Volumes** 59

B. **Comparison of SETs at Comparable Charge Generated Values** 62

C. **Comparison of SET Shape Trends Across Radiation Sources** 72

D. **Mechanisms** 79

1) *Temporal Duration of Charge Injection* 81

2) *Radial Width of Charge Injection* 82

3) *Range of Charge Injection* 83

4) *Starting Location of Charge Injection* 85

CONCLUSIONS AND FUTURE WORK 87

REFERENCES 89

APPENDIX A – SET CHARACTERISTICS PROCESSING CODE 97

APPENDIX B – SIMULATED DOPING PROFILE VS EXPERIMENTAL DOPING PROFILE 100

APPENDIX C – SENTAURUS TCAD PHYSICS MODEL PARAMETERS 101

LIST OF TABLES

Table		Page
I.1.	Comparison of Radiation Sources……………………………………………..	2
III.1.	Attenuation lengths for common materials from [64]……………………………	19
IV.1.	LBNL heavy ions used for testing……………………………………………….	25
IV.2.	NRL TPA laser testing conditions used…………………………………….........	27
IV.3.	APS focused X-ray testing conditions used………………………………………	29
IV.4.	Physics models used in Sentaurus TCAD simulations…………………………...	33
VI.1.	Summary of sensitive volume depths and funnel lengths………………………...	61
VI.2.	Summary of -5 V SETs resulting from ~5.8 pC of generated charge……………..	63
VI.3.	Summary of -90 V SETs resulting from ~5.8 pC of generated charge…………..	67
VI.4.	Summary of -5 V SETs resulting from ~15 pC of generated charge……………...	68
VI.5.	Summary of -90 V SETs resulting from ~15 pC of generated charge……………	70

LIST OF FIGURES

Figure Page

II.1. An artist's rendition of the near-earth radiation environment, showing the solar transient environment (Solar Protons & Heavier Ions), the transient Galactic Cosmic Ray environment, and the trapped environment (Protons, Electrons, Heavy Ions). [12] 6

II.2. (Left) Total mission dose in krad(Si) for an ISS orbit (solid lines) and a GEO orbit (dashed lines) during solar minimum (black) and solar maximum (red). (Right) LET integral flux spectra for the same orbits. Graphs generated using SPENVIS [20]. 7

II.3. An ion passes through a p-n junction and loses energy to the surrounding lattice (left). This lost energy generates electron-hole pairs (middle), which are then collected through drift-diffusion processes (right). 8

II.4. A typical SET that occurs after an ion strikes a *pn* junction. The initial, prompt collection occurs via drift and is evident by the fast rise time and initially fast fall time. A combination of drift and diffusion are responsible for the longer exponential tails in the fall time. 9

II.5. An example SEU. Before the ion strike (red dashed line), the device is maintaining a constant initial value. After the ion strike, the device's voltage level decreases until it falls below the error threshold. The device maintains this new, incorrect state until the power is reset (dashed blue line) and the device returns to its nominal initial value. 10

III.1. LET curves from SRIM [42] for a 1.2 GeV xenon ion (black), 660 MeV copper ion (red), and 290 MeV silicon ion (blue) in silicon. 13

III.2. LET integral flux spectra for an ISS orbit (solid lines) and a GEO orbit (dashed lines) during solar minimum (black) and solar maximum (red). Graphs generated using SPENVIS [17]. The greyed portion of the spectra shows the LET range that conventional heavy ion facilities can achieve. 14

III.3. (Top) SPA. A single photon with energy greater than the semiconductor's bandgap energy is absorbed and creates a single electron-hole pair. (Bottom) TPA. Two

photons with a combined energy greater than the semiconductor's bandgap energy are absorbed and create a single electron-hole pair. 16

III.4. (Left) 2D, time-integrate carrier density distribution output from Lumerical FDTD Solutions for a 990 pJ laser focused 14 μm into silicon. (Right) Radially integrated line charge distribution of the carrier density distribution, giving the amount of charge generated per unit length. 18

III.5. Charge generated per unit length curves for 8 keV (black), 10 keV (red), and 12 keV (blue) X-ray photon energies at APS. Curves are for pulses with the maximum available flux on July 25, 2019. 20

IV.1. Basic drawing of diode test structure (left) and detailed doping profile (right). The diode has a 25 μm active region (p^+ and n^- layers) that lies on top of heavily doped substrate. The metallurgical junction occurs approximately 6 μm into the silicon. The vertical dashed and solid lines on the doping profile show the location of the junction and the substrate, respectively. 23

IV.2. Band diagrams of the diode biased at 0 V (top), -5 V (bottom left), and -90 V (bottom right). The dashed lines with the arrow between show the depletion region and the solid vertical line shows the beginning of the substrate. These diagrams were made using TCAD. 244

IV.3. Schematic of experimental setup. All devices were mounted in custom high-speed packages. The purple lines represent the high-speed connections for the SET path from device to oscilloscope. The black lines represent the BNC power connections. A personal computer is used to control the power supplies via ethernet connection and to collect data from the oscilloscope via USB connection. 24

IV.4. LET curves for the xenon (black), copper (red), and silicon (blue) ions used during heavy ion testing. LET was converted to charge generated on the right y-axis. The dashed grey line shows the cutoff for integration. 25

IV.5. Charge generated in diode's active region versus focal position for the pulsed laser at 990 pJ (black circles), 750 pJ (red squares), and 400 pJ (blue triangles). A focal position of 0 μm corresponds to the focus being at the surface of silicon on the diode's anode. 26

IV.6. Charge generated per unit length curves for the 990 pJ focal positions. Focal positions run from -4 μm out of the silicon to 24.5 μm into the silicon. The dashed grey line shows the cutoff for integration....27
IV.7. Charge generated per unit length curves for the 750 pJ focal positions. Focal positions run from -3 μm out of the silicon to 24.5 μm into the silicon. The dashed grey line shows the cutoff for integration....28
IV.8. Charge generated per unit length curves for the 400 pJ focal positions. Focal positions run from -4 μm out of the silicon to 24.5 μm into the silicon. Note that the y-axis scale for this graph is much smaller than the scale on the 750 pJ and 990 pJ graphs. The dashed grey line shows the cutoff for integration. 28
IV.9. Charge generated per unit length curves for the 8 keV X-ray pulses at full flux (black), ½ flux (red), and ¼ flux (blue). The dashed grey line shows the cutoff for integration. 30
IV.10. Charge generated per unit length curves for the 10 keV X-ray pulses at full flux (black), ½ flux (red), and ¼ flux (blue). The dashed grey line shows the cutoff for integration....30
IV.11. Charge generated per unit length curves for the 12 keV X-ray pulses at full flux (black), ½ flux (red), and ¼ flux (blue). The dashed grey line shows the cutoff for integration....31
IV.12. Typical SET (black) and its associated fitted SET (red) from a heavy ion (left), focused X-ray (middle), and pulsed laser (right) experiment. All SETs are from the -5 V bias condition. The fits shown here have R^2 values ≥0.97....32
IV.13. Two-dimensional cross-section of the simulated diode structure. The x-y plane shown here is rotated about the y-axis during simulations to produce a 2D cylindrical simulation. 34
IV.14. Experimental (black) and TCAD simulated (red) IV curves. The reverse leakage currents show good agreement. 34
IV.15. Circuit schematic of the bias tee attached to the diode's anode. The components in the dark grey box form the bias tee, which has a dominant capacitance of 82 nF and an inductance of 10 μH. The black box denotes the oscilloscope connections, which has a 50 Ω impedance. The cathode bias tee is identical [114]....35

IV.16. Experimentally averaged SET (black) and TCAD simulated SET (red) for the Xe ion (left), 8 keV full flux X-ray (middle), and 990 pJ laser at a focal position of 3.5 µm (right) at a bias of -5 V. 36
IV.17. Experimentally averaged SET (black) and TCAD simulated SET (red) for the Xe ion (left), 8 keV full flux X-ray (middle), and 990 pJ laser at a focal position of 3.5 µm (right) at a bias of -90 V. 36
V.1. Heavy ion-induced collected charge as a function of charge generated for -5 V (closed circles) and -90 V (open circles) bias conditions. Collected charge shows a linear relationship with charge generated. 38
V.2. Heavy ion-induced peak current as a function of charge generated for -5 V (closed circles) and -90 V (open circles) bias conditions. Peak current shows a linear relationship with charge generated. 38
V.3. Heavy ion-induced transient rise time as a function of charge generated for -5 V (closed circles) and -90 V (open circles) bias conditions. Rise time decreases at as reverse bias increases. 39
V.4. Heavy ion-induced transient fall time as a function of charge generated for -5 V (closed circles) and -90 V (open circles) bias conditions. Fall time decreases at as reverse bias increases. 40
V.5. Heavy ion-induced transient FWHM as a function of charge generated for -5 V (closed circles) and -90 V (open circles) bias conditions. FWHM decreases at as reverse bias increases. 40
V.6. Heavy ion TCAD simulation results from the -5 V bias condition. Conduction band potential (left) and electric field (right) are shown at two time steps: at peak charge injection (top) and 1 ns post peak charge injection (bottom). Nominal conditions are denoted by the dashed grey lines. 41
V.7. Heavy ion TCAD simulation results from the -90 V bias condition. Conduction band potential (left) and electric field (right) are shown at two time steps: at peak charge injection (top) and 5 ns post peak charge injection (bottom). Nominal conditions are denoted by the dashed grey lines. 42

V.8. Pulsed laser-induced collected charge as a function of charge generated for pulse energies 400 pJ (black circles) 750 pJ (red squares), and 990 pJ (green triangles) at -5 V. Collected charge shows a linear relationship with charge generated. 44
V.9. Pulsed laser-induced collected charge as a function of charge generated for pulse energies 400 pJ (black circles) 750 pJ (red squares), and 990 pJ (green triangles) at -90 V. Collected charge shows a linear relationship with charge generated. 44
V.10. Pulsed laser-induced peak current as a function of charge generated for pulse energies 400 pJ (black circles) 750 pJ (red squares), and 990 pJ (green triangles) at -5 V. Peak current shows a linear relationship with charge generated. 45
V.11. Pulsed laser-induced peak current as a function of charge generated for pulse energies 400 pJ (black circles) 750 pJ (red squares), and 990 pJ (green triangles) at -90 V. Peak current shows a linear relationship with charge generated. 45
V.12. Pulsed laser-induced transient rise time as a function of charge generated for pulse energies 400 pJ (black circles) 750 pJ (red squares), and 990 pJ (green triangles) at -5 V. The black arrow shows the direction of focal positions moving further into the diode...46
V.13. Pulsed laser-induced transient rise time as a function of charge generated for pulse energies 400 pJ (black circles) 750 pJ (red squares), and 990 pJ (green triangles) at -90 V. Rise time is consistent as a function of charge generated and focal position......47
V.14. Pulsed laser-induced transient fall time as a function of charge generated for pulse energies 400 pJ (black circles) 750 pJ (red squares), and 990 pJ (green triangles) at -5 V. The black arrow shows the direction of focal positions moving further into the diode...48
V.15. Pulsed laser-induced transient fall time as a function of charge generated for pulse energies 400 pJ (black circles) 750 pJ (red squares), and 990 pJ (green triangles) at -90 V. Fall time is consistent as a function of charge generated and focal position.......48
V.16. Pulsed laser-induced transient FWHM as a function of charge generated for pulse energies 400 pJ (black circles) 750 pJ (red squares), and 990 pJ (green triangles) at -90 V. FWHM increases with increased charge generated and shows a slight dependence on focal position...49

V.17. Pulsed laser-induced transient FWHM as a function of charge generated for pulse energies 400 pJ (black circles) 750 pJ (red squares), and 990 pJ (green triangles) at -90 V. FWHM is consistent as a function of charge generated and focal position.........49
V.18. Pulsed laser TCAD simulation results from the -5 V bias condition. Conduction band potential (left) and electric field (right) are shown at two time steps: at peak charge injection (top) and 1 ns post peak charge injection (bottom). Nominal conditions are denoted by the dashed grey lines. 51
V.19. Pulsed laser TCAD simulation results from the -90 V bias condition. Conduction band potential (left) and electric field (right) are shown at two time steps: at peak charge injection (top) and 1 ns post peak charge injection (bottom). Nominal conditions are denoted by the dashed grey lines...52
V.20. Focused X-ray-induced collected charge as a function of charge generated for 8 keV (black circles), 10 keV (red squares), and 12 keV (green triangles) photon energies. Closed shapes show -5 V data, while open shapes show -90 V. Collected charge shows a linear relationship with charge generated. 53
V.21. Focused X-ray-induced peak current as a function of charge generated for 8 keV (black circles), 10 keV (red squares), and 12 keV (green triangles) photon energies. Closed shapes show -5 V data, while open shapes show -90 V. Peak current shows a linear relationship with charge generated. 54
V.22. Focused X-ray-induced transient rise time as a function of charge generated for 8 keV (black circles), 10 keV (red squares), and 12 keV (green triangles) photon energies. Closed shapes show -5 V data, while open shapes show -90 V. Rise time is constant with respect to charge generated..55
V.23. Focused X-ray-induced transient fall time as a function of charge generated for 8 keV (black circles), 10 keV (red squares), and 12 keV (green triangles) photon energies. Closed shapes show -5 V data, while open shapes show -90 V. Fall time is constant with respect to charge generated. 55
V.24. Focused X-ray-induced transient FWHM as a function of charge generated for 8 keV (black circles), 10 keV (red squares), and 12 keV (green triangles) photon energies. Closed shapes show -5 V data, while open shapes show -90 V. FWHM is constant with respect to charge generated...56

V.25. Focused X-ray TCAD simulation results from the -5 V bias condition. Conduction band potential (left) and electric field (right) are shown at two time steps: at peak charge injection (top) and 1 ns post peak charge injection (bottom). Nominal conditions are denoted by the dashed grey lines. 57
V.26. Focused X-ray TCAD simulation results from the -90 V bias condition. Conduction band potential (left) and electric field (right) are shown at two time steps: at peak charge injection (top) and 1 ns post peak charge injection (bottom). Nominal conditions are denoted by the dashed grey lines. 58
VI.1. Sensitive volumes for the -5 V (left) and -90 V (right) experiments. Heavy ion volumes are shown in black, pulsed laser volumes in blue, and focused X-ray volumes in red. The translucent grey boxes show the nominal depletion region at that bias condition. 61
VI.2. Averaged transients from the copper heavy ion (black), 750 pJ pulsed laser at a focal position of -1 µm (blue), and 12 keV, ½ flux focused X-ray (red) at a reverse bias of 5 V. Each of these SEE sources generated approximately 5.8 pC of charge in the diode's active region. 63
VI.3. Copper heavy ion (black), 12 keV ½ flux focused X-ray (red), and 750 pJ -1 µm pulsed laser (blue) TCAD simulation results from the -5 V bias condition. Conduction band potential (left) and electric field (right) are shown at two time steps: at peak charge injection (top) and 1 ns post peak charge injection (bottom). Nominal conditions are denoted by the dashed grey lines. 64
VI.4. Averaged transients from the copper heavy ion (black), 750 pJ pulsed laser at a focal position of -1 µm (blue), and 12 keV, ½ flux focused X-ray (red) at a reverse bias of 90 V. Each of these SEE sources generated approximately 5.8 pC of charge in the diode's active region. 65
VI.5. Copper heavy ion (black), 12 keV ½ flux focused X-ray (red), and 750 pJ -1 µm pulsed laser (blue) TCAD simulation results from the -90 V bias condition. Conduction band potential (left) and electric field (right) are shown at two time steps: at peak charge injection (top) and 1 ns post peak charge injection (bottom). Nominal conditions are denoted by the dashed grey lines. 66

VI.6. Averaged transients from the xenon heavy ion (black), 990 pJ pulsed laser at a focal position of 3.5 µm (blue), and 8 keV, full flux focused X-ray (red) at a reverse bias of 5 V. Each of these SEE sources generated approximately 15 pC of charge in the diode's active region. 68

VI.7. Xenon heavy ion (black), 8 keV full flux focused X-ray (red), and 990 pJ 3.5 µm pulsed laser (blue) TCAD simulation results from the -5 V bias condition. Conduction band potential (left) and electric field (right) are shown at two time steps: at peak charge injection (top) and 1 ns post peak charge injection (bottom). Nominal conditions are denoted by the dashed grey lines. 69

VI.8. Averaged transients from the xenon heavy ion (black), 990 pJ pulsed laser at a focal position of 3.5 µm (blue), and 8 keV, full flux focused X-ray (red) at a reverse bias of 90 V. Each of these SEE sources generated approximately 15 pC of charge in the diode's active region. 70

VI.9. Xenon heavy ion (black), 8 keV full flux focused X-ray (red), and 990 pJ 3.5 µm pulsed laser (blue) TCAD simulation results from the -90 V bias condition. Conduction band potential (left) and electric field (right) are shown at two time steps: at peak charge injection (top) and 1 ns post peak charge injection (bottom). Nominal conditions are denoted by the dashed grey lines. 71

VI.10. Peak current as a function of charge generated at -5 V (left) and -90 V (right) for heavy ion-, focused X-ray-, and pulsed laser-induced SETs. 72

VI.11. Collected charge as a function of charge generated at -5 V (left) and -90 V (right) for heavy ion-, focused X-ray-, and pulsed laser-induced SETs. 73

VI.12. Transient rise time as a function of charge generated at -5 V (left) and -90 V (right) for heavy ion-, focused X-ray-, and pulsed laser-induced SETs. 74

VI.13. Transient fall time as a function of charge generated at -5 V (left) and -90 V (right) for heavy ion-, focused X-ray-, and pulsed laser-induced SETs. 75

VI.14. Transient FWHM as a function of charge generated at -5 V (left) and -90 V (right) for heavy ion-, focused X-ray-, and pulsed laser-induced SETs. 76

VI.15. Electric field cuts from the -5 V TCAD simulations at the time of peak injection (left) and 1 ns post peak injection (right) for heavy ions (top), focused X-ray (middle), and pulsed laser (bottom). 77

VI.16. Electric field cuts from the -90 V TCAD simulations at the time of peak injection (left) and 1 ns post peak injection (right) for heavy ions (top), focused X-ray (middle), and pulsed laser (bottom). 78
VI.17. Normalized 2D charge generation profiles for heavy ions (top), focused X-rays (2nd to top), pulsed laser focused at3.5 μm into the silicon (2nd to bottom), and pulsed laser focused at 21 μm into the silicon (bottom). 79
VI.18. Illustration of the charge generation profile aspects. Temporal duration refers to the length of time over which the charge is injected and is Gaussian in shape. Range refers to how long the charge generation profile is. Radial width refers to the radial Gaussian width of the initial charge injection. Starting location refers to the location in the diode where the charge injection begins. 80
VI.19. Electric field cuts for the -5 V (top) and -90 V (bottom) TCAD simulations examining pulse duration at the time of peak charge injection (left) and 1 ns post peak injection (right). 81
VI.20. Electric field cuts for the -5 V (top) and -90 V (bottom) TCAD simulations examining radial distribution width at the time of peak charge injection (left) and 1 ns post peak injection (right). 83
VI.21. Electric field cuts for the -5 V (top) and -90 V (bottom) TCAD simulations examining the range of charge injection at the time of peak charge injection (left) and 1 ns post peak injection (right). 84
VI.22. Electric field cuts for the -5 V (top) and -90 V (bottom) TCAD simulations examining starting location of charge injection at the time of peak charge injection (left) and 1 ns post peak injection (right). 86

CHAPTER I

INTRODUCTION

In 1969, Man went to the Moon. This was a part of the great Space Race, which launched the United States' space program. The National Aeronautics and Space Administration (NASA) was started in 1958 as part of it. Since the launch of the first satellite, the harshness of the space radiation environment has been an obstacle in space exploration [1]. Since then, ground-based radiation testing of electronics has become standard procedure during the development of spacecraft to increase the reliability of payloads and the probability of mission success. Testing techniques and our understanding of potential failure mechanisms have grown since then, as has the complexity of electronics being considered for spaceflight. As commercial interest in space grows, so does the need for ground-based radiation effects testing.

The space radiation environment causes both long-term degradation and instantaneous effects in electronics. The instantaneous effects, called single event effects (SEEs), are caused by single ionizing particles passing through sensitive regions in electronic devices. SEEs cause a variety of effects in electronics, from recoverable flipped bits in memory cells to permanent device failures like gate rupture or burnout in power devices [2]. As electronics become smaller and more densely populated, SEEs on-orbit are becoming more common and ground-based testing is becoming more critical. Many of the facilities being using for ground-based testing, particularly those used for studying high energy particles, were built during the early days of spaceflight, and are aging [3]. A non-trivial portion of these facilities are also not used primarily for radiation effects testing, so availability is limited. Despite these challenges, SEE testing is of increasing interest as more companies begin to explore the profitability of space and as commercial electronics become increasingly complex.

Increased demand for ground-based SEE testing has led to the need for alternative testing methods to alleviate strain on the conventional heavy ion-based testing infrastructure. Two alternative testing methods that have been identified are the femtosecond pulsed laser and the picosecond focused X-ray. These sources are photon-based and generate charge through the absorption of photons, which then create SEEs similarly to heavy ions. Photon-based radiation sources have advantages over heavy ion radiation sources, such as increased spatial and temporal

control of charge generation, prompting interest in using these radiation sources beyond just as a solution to the accelerator shortage [4]. Table I.1 summarizes some key differences between the radiation sources. Heavy ions are the gold standard for spaceflight radiation effects testing, in large part due to how well correlated they are to the space radiation environment, but it is still unclear how these alternative methods correlate to heavy ions and the space radiation environment. While there is an availability shortage of heavy ion facilities, it is relatively inexpensive and simple to develop an appropriate pulsed laser setup. Photon-based SEE testing sources can provide greater control over the location of the generated charge compared to heavy ions and have more predictable repetition rates. Pulsed lasers cannot generate charge in oxides at the photon energies used for SEE testing, and so there is no accumulation of total ionizing dose (TID), but they are unable to penetrate metals. Focused X-rays, on the other hand, can penetrate through metal layers, but can also cause large amounts of location TID damage. Overall, it may prove that these techniques are not direct substitutions for each other, but instead enhance the overall ability for SEE mechanism exploration.

Table I.1. Comparison of Radiation Sources

Source	Heavy Ions	Pulsed Laser	Focused X-Ray
Known correlation to space radiation environment	✓	✗	✗
Facility accessibility in U.S.	**Few**	**Many**	**Few**
Spatial, temporal control over charge generation	✗	✓	✓
No accumulation of TID	✗	✓	✗
Penetration of metal	✓	✗	✓

This dissertation explores differences in single event transients (SETs) resulting from charge generation from heavy ions, pulsed lasers, and focused X-rays using an epitaxial silicon diode as a common test structure. SET experiments are performed on the diode using heavy ions, pulsed lasers, and focused X-rays, and trends in SET shape are compared as a function of bias condition and the amount of charge generated in the diode's active region. By comparing SET shape characteristics, such as peak current, collected charge, transient rise time, transient fall time, and

transient full width at half maximum (FWHM), assumptions about differences between the charge generation sources can be drawn. In this dissertation, it is observed that the different radiation sources interact with the diode's internal electric field differently, resulting in differences in SET shape and trends in SET shape. The physical mechanisms behind the differences are discussed and applied to other types of SEEs.

Chapter II provides a general background on the space radiation environment and radiation effects. Special attention is given to SEEs, the focus of this dissertation. The different types of SEEs are discussed.

Chapter III contains detailed descriptions of the charge generation process for heavy ions, femtosecond pulsed laser, and picosecond focused X-rays. Much work has been done using the alternative radiation sources, comparing the different sources, and trying to correlate the different sources. A review of that work is presented at the end of the chapter.

Chapter IV documents experimental procedures and simulation setup. The diode test structure and relative bias conditions are presented. The experimental setup was kept as consistent as possible between the different experiments and is shown in detail. All experimental test conditions are provided for each radiation source, including charge generation profiles found using the methods discussed in ***Chapter III***. A double exponential fit is used to ensure consistency when comparing SETs from different sources; the function and data processing methodology is discussed. The Sentaurus technology computer aided design (TCAD) simulation space is described.

Chapter V presents the experimental SET results organized by radiation source. SET shape characteristics such as peak current, collected charge, transient rise time, transient fall time, and transient FWHM are graphed as a function of charge generated in the diode's active region for all experimental conditions. Trends in shape characteristics are analyzed for each radiation source and TCAD simulations are provided to support the experimental observations.

Chapter VI compares the SET shape characteristics from different radiation sources. It is observed that the different radiation sources result in both different SET shape characteristics, and different trends in SET shape characteristics as a function of both bias condition and amount of charge generated in the diode's active region. TCAD simulations are used to explain and explore the mechanisms causing the observed differences.

Chapter VII highlights the important conclusions for this dissertation and provides thoughts on how to further explore the various radiation sources.

CHAPTER II

BACKGROUND

A. Space Radiation Environment

Space-based electronics play a large role today – from weather tracking to national security to exploring our universe – and its role is only increasing. The commercial space industry is rapidly growing, looking to capitalize on asteroid mining, private satellites, and space-tourism [5-8]. NASA is aiming to go back to the moon by 2028 and establish a permanent presence, and space agencies across the world are striving to increase their presence on Mars [9-11]. This growth has increased the need for a greater understanding of how electronic devices respond to the harsh space radiation environment.

Figure II.1 gives an artist's depiction of the radiation environment near Earth. There are two distinct radiation environments of concern for Earth-orbiting spacecraft: the trapped environment and the transient environment. The trapped environment consists of protons, electrons, and some heavy ions that are trapped within the Van Allen Belts due to the Earth's magnetic field. The transient space radiation environment consists of galactic cosmic rays (GCRs) and the solar transient environment. GCRs are composed of all naturally occurring elements, though most GCRs are elements iron or lighter, and can have energies as high as 10^{11} GeV, while the solar transient environment is comprised primarily of protons and heavy ions [13-15].

The different types of space radiation result in three types of radiation effects in semiconductors. Total ionizing dose (TID) is the gradual degradation of performance from the buildup of defects within semiconductors and oxides, and at semiconductor-oxide interfaces. Displacement damage dose (DDD) is the gradual degradation of performance resulting from the displacement of atoms within the semiconductor lattice. Single event effects (SEEs) are transient effects caused by a single ionizing particle passing through a semiconductor device and can result in a wide range of observable effects. TID is primarily caused by protons and electrons, DDD is typically the result of protons, and SEEs can be caused by protons and heavy ions [16-19]. Single event effects are the focus of this dissertation.

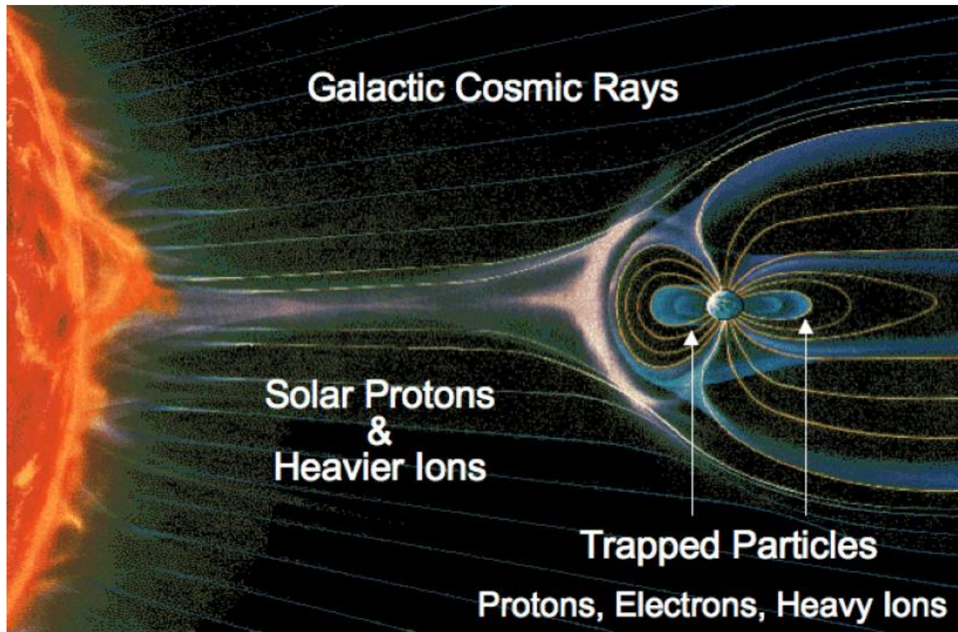

Figure II.1. An artist's rendition of the near-earth radiation environment, showing the solar transient environment (Solar Protons & Heavier Ions), the transient Galactic Cosmic Ray environment, and the trapped environment (Protons, Electrons, Heavy Ions). [12]

The abundance of the different types of radiation varies with distance from Earth and solar cycle. Spacecraft are shielded from GCRs and solar wind while within the Earth's magnetosphere, so the trapped environment is the dominate radiation source in orbits closer to Earth. Orbits outside of the magnetosphere have radiation environments dominated by the transient environment. The Sun's solar cycle plays a large role in regulating the relative abundance of protons, electrons, and heavy ions in the space radiation environment. During solar maximum, solar proton fluxes increase and GCR fluxes decrease due to push back from the stronger solar wind, while the reserve occurs during solar minimum.

Figure II.2 demonstrates how changes in spacecraft orbit and solar cycle can affect the observed radiation environment by comparing the TID dose-depth curves (left) and LET flux spectra (right) for the International Space Station (ISS) orbit and a geostationary orbit (GEO) during solar maximum and solar minimum. The TID dose-depth curves show how TID changes as a function of aluminum shield thickness, with the most common value of 100 mils denoted by the grey dashed line. The GEO orbits have significantly higher TID levels, due to the lack of shielding from the magnetosphere, and solar maximum results in slightly higher TID levels compared to solar minimum from the increase in solar protons. The LET spectra curves show the particle integral

fluxes for the different orbits. The main feature of note is the higher flux of high LET particles for the GEO orbits, which increases the rate of SEEs. The dashed grey line shows the "iron cutoff," where particle fluxes decrease significantly due to the smaller abundance of elements heavier than iron in the universe.

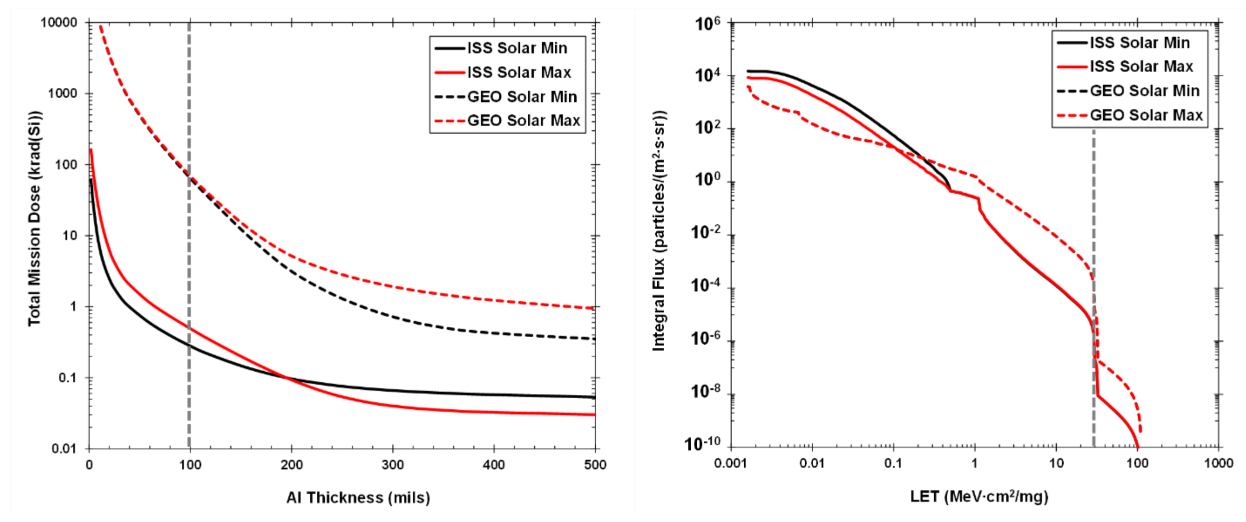

Figure II.2. (Left) Total mission dose in krad(Si) for an ISS orbit (solid lines) and a GEO orbit (dashed lines) during solar minimum (black) and solar maximum (red). (Right) LET integral flux spectra for the same orbits. Graphs generated using SPENVIS [20].

B. Single Event Effects

Single event effects occur when an ionizing particle, such as a proton or heavy ion, passes through a semiconductor and generates charge. The ionizing particle transfers energy to the surrounding lattice via Coulombic interactions, and this transferred energy generates electron-hole pairs. The electron-hole pairs separate and can be collected at device contacts or can recombine, depending on the device operating conditions. Figure II.3 shows the general process and associated timescales for an occurring SEE. First, an ion passes through the device and deposits energy, occurring on the order of femtoseconds (Figure II.3 left). That deposited energy generated electron-hole pairs on a timescale of femtoseconds to picoseconds (Figure II.3 middle). Finally, the generated charge is separated by internal electric fields and is either collected at the device contacts via drift-diffusion processes or recombines (Figure II.3 right). Charge collection occurs over picoseconds or longer [21-23].

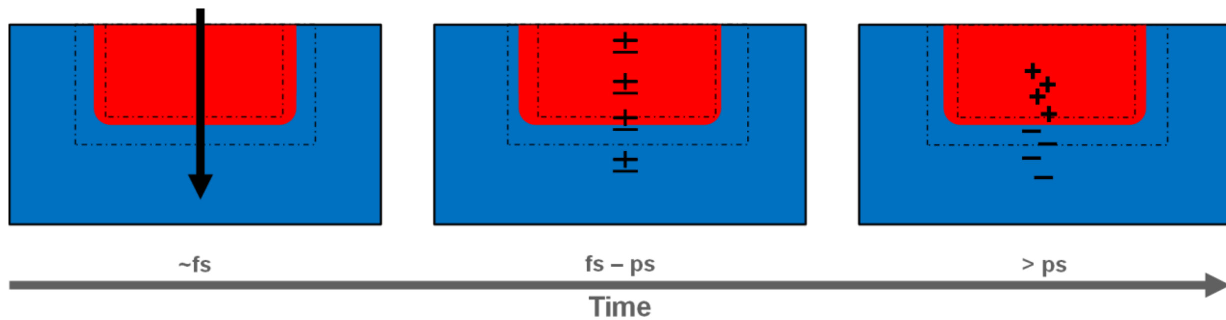

Figure II.3. An ion passes through a p-n junction and loses energy to the surrounding lattice (left). This lost energy generates electron-hole pairs (middle), which are then collected through drift-diffusion processes (right).

The result of an SEE depends on the device affected. There are two broad categories of SEEs: non-destructive and destructive. Non-destructive SEEs do not cause permanent device failure and can be recovered from, either on their own or through a power cycle. Types of non-destructive SEEs include single event transients (SETs), single event upsets (SEUs), multiple bit upsets (MBUs), and singe event functional interrupts (SEFIs). Destructive single event effects cause permanent device or circuit failure and are non-recoverable. Single event burnout (SEB), single event gate rupture (SEGR), and single event latch-up (SEL) are main types of destructive SEEs [2, 24].

Single event transients (SET) are voltage or current transients that result from SEEs. Figure II.4 shows a typical SET for a basic *pn* junction, with a characteristic double-exponential shape. Charge that is generated in an electric field region, such as *pn* junction, is collected first through drift. This is the dominant collection mechanism during the fast rise time of the SET and part of the fall time. After the prompt collection ends, charge continues to be collected as it diffuses to an electric field region where it is then collected through drift. This "diffusion + drift" collection mechanism is responsible for the long tails seen in the fall times of some SETs. It is possible for charge to recombine before it diffuses to an electric field, causing the amount of collected charge to be less than the generated charge, or for avalanching to occur, causing a greater amount of charge to be collected [25, 26]. SETs are considered recoverable, or "soft", errors as the transient self recovers. While this work focuses on SETs, the mechanisms behind them can be generalized to other SEEs.

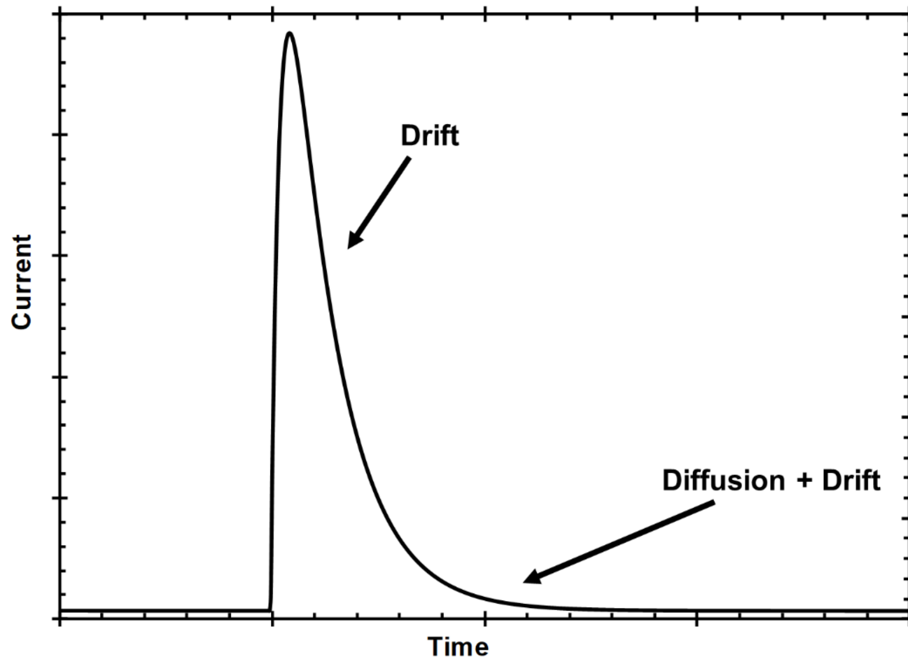

Figure II.4. A typical SET that occurs after an ion strikes a *pn* junction. The initial, prompt collection occurs via drift and is evident by the fast rise time and initially fast fall time. A combination of drift and diffusion are responsible for the longer exponential tails in the fall time.

When a critical amount of charge is collected in a sensitive region of a device, single event upsets (SEUs) occur [27, 28]. SEUs occur in analog, digital, and optical devices and present as a change from one logic state to another. In memory devices, SEUs typically present as bit flips [29, 30]. In some cases, an SEU can flip the bits in multiple memory cells; this is called a multiple bit upset (MBU) [31, 32]. SEUs typically persist until the device is power cycled or until the device naturally recovers, but they do not induce permanent changes to the device [33]. SEUs that result in bit flips can be corrected using error detection and correction (EDAC) coding. As such, they are considered soft errors. Figure II.5 is a representative example of an SEU occurring. The device is at a nominal state before the SEE occurs, after which the device falls below the error threshold where it remains until the power is cycled and the device is reset.

Single event functional interrupt (SEFI) is a special type of SEU that occurs in microcircuits and causes a disruption in the nominal operating conditions. SEFIs are generally found when testing for other types of SEEs and are identified when all other possible SEEs are ruled out as explanations for the observed effect. SEFIs typically persist until the registry is reset, either through a power cycle or by reinitiating the program and are considered soft errors [34].

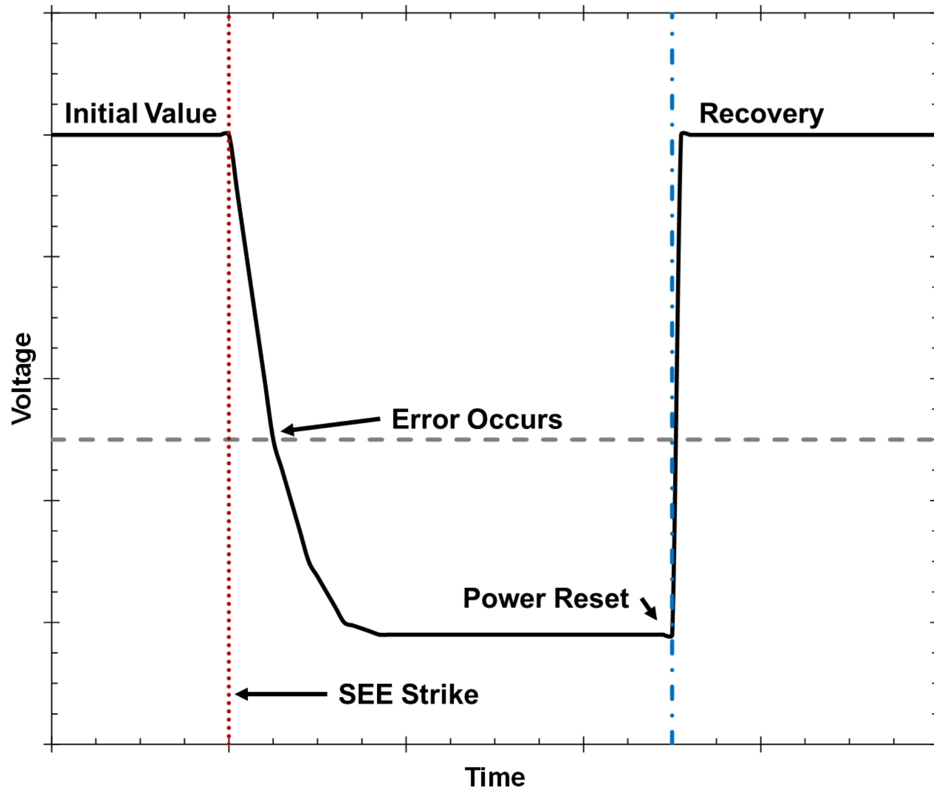

Figure II.5. An example SEU. Before the ion strike (red dashed line), the device is maintaining a constant initial value. After the ion strike, the device's voltage level decreases until it falls below the error threshold. The device maintains this new, incorrect state until the power is reset (dashed blue line) and the device returns to its nominal initial value.

Single event burnout (SEB) and single event gate rupture (SEGR) are destructive SEEs that typically occur in power devices [35-37]. SEB can be identified by a resistive short between the drain and source nodes on power MOSFETs, visible discoloration or damage of the die, and threshold voltage becoming independent of off-state gate bias. SEB occurs when the drain-source voltage exceeds the second breakdown voltage of the MOSFET or when the voltage potential in the source region exceeds the built-in potential of the parasitic bipolar junction transistor (BJT) [26, 38]. SEGR can be identified by a measurable gate current increase and typically does not present with visible damage to the die. While the underlying mechanisms for SEGR are still being investigated, the main area of concern is in the epitaxial area of power MOSFETs underneath the gate oxide, known as the neck region [37, 39, 40].

Single event latch-up (SEL) is a sustained high current state induced by an ion strike. SEL occurs when an ionizing particle generates enough charge to turn on the parasitic bipolar structure of a CMOS device [41, 42]. While the sustained high current state can be recovered from by power

cycling the device, SEL is typically considered a destructive SEE because the runaway high current can quickly damage other parts in the circuit before there is a chance to power cycle. Because CMOS technology plays a large role in modern devices, SEL is a major concern for spacecraft.

CHAPTER III

GROUND-BASED SEE TESTING METHODS

SEEs have the potential to induce failures into spacecraft systems, both hard and soft failures. To reduce the potential scientific and economic impact of SEE-induced failures, sensitive electronics are typically tested at ground-based facilities before being used in spacecraft systems. Accelerator-based heavy ion test facilities are the conventional choice for ground-based SEE testing due in large part to their known correlation to the space radiation environment. An increased demand and aging infrastructure, however, has led to an availability shortage of these facilities, increasing the use of alternative testing methods [3]. This chapter discusses the three most common types of ground-based SEE testing methods currently used: heavy ions, pulsed lasers, and focused X-rays. The current state of correlation efforts between these testing techniques is discussed at the end of the chapter.

A. Heavy Ions

Heavy ions, and the SEE environment, are characterized by an ion's *linear energy transfer* (LET). LET is the rate of energy lost through Coulombic interactions by the incident ion per unit length as it travels through a semiconductor. LET is normalized to the density of the semiconductor, allowing for comparison of LETs amongst different semiconductor materials. Equation III.1 is the mathematical expression for LET, where ρ is the semiconductor density (2.329 g/cm^3 for Si) and $E_{elec}(x)$ is the electronic stopping energy of the ion.

$$LET(x) = -\frac{1}{\rho}\frac{dE_{elec}(x)}{dx} \qquad (III.1)$$

LET curves can be found using software like SRIM [43], which calculates an ion's LET curve for user defined material stacks. Figure III.1 shows example LET curves for 1.2 GeV xenon, 660 MeV copper, and 290 MeV silicon in silicon. An ion's LET is typically reported as the surface incident value (59, 21, and 6 MeV·cm^2/mg for the xenon, copper, and silicon in Figure III.3, respectively).

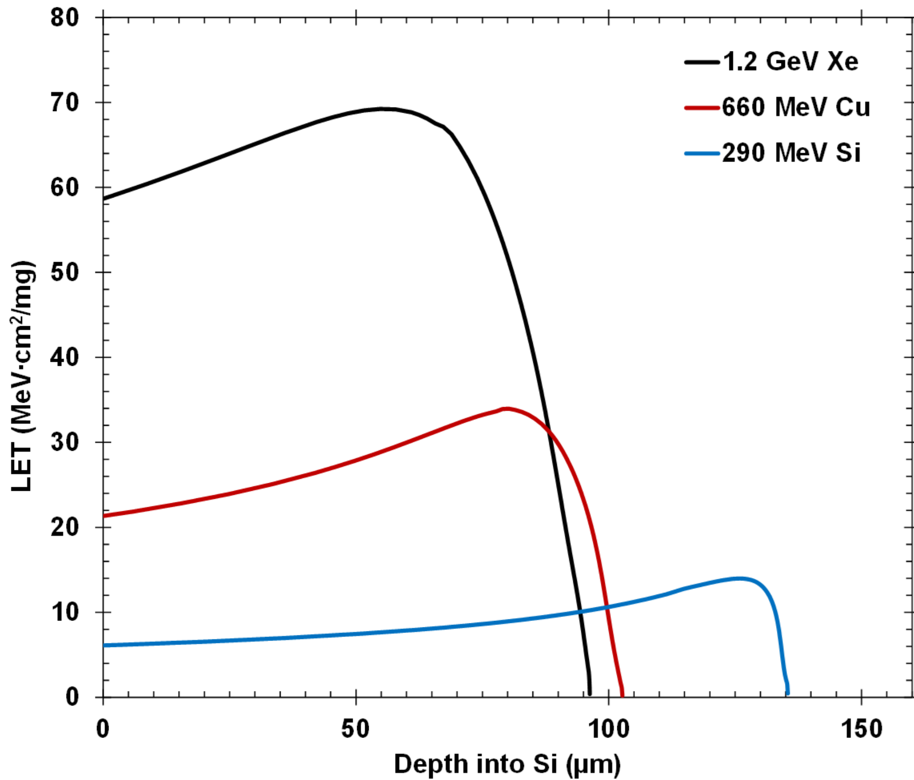

Figure III.1. LET curves from SRIM [42] for a 1.2 GeV xenon ion (black), 660 MeV copper ion (red), and 290 MeV silicon ion (blue) in silicon.

There are several accelerator-based heavy ion facilities in North America and Europe that are regularly used for testing spacecraft electronics [44-47]. These facilities provide a range of LETs for users that span a typical space radiation environment. The LET spectra for the ISS and geosynchronous orbits from Figure II.2 has been reprinted in Figure III.2 and the range of LETs available at the referenced facilities is shown in blue, illustrating the good correlation between these ground-based facilities and the space radiation environment. The lower LETs that are seen in space can be simulated on the ground using protons and light ions [48], thus filling out the whole LET spectra.

The amount of charge generated from heavy ions is directly related to an ion's LET and can be found by integrating the LET curve and normalizing to the materials electron-hole pair creation energy. The electron-hole pair creation energy is the average amount of energy necessary to free one electron-hole pair (3.6 eV/ehp in silicon). The total amount of charge generated is shown mathematically in Equation III.2, where q is the elementary charge, ρ is the density of the semiconductor, E_{ehp} is the semiconductor's electron-hole pair creation energy, and l is the path

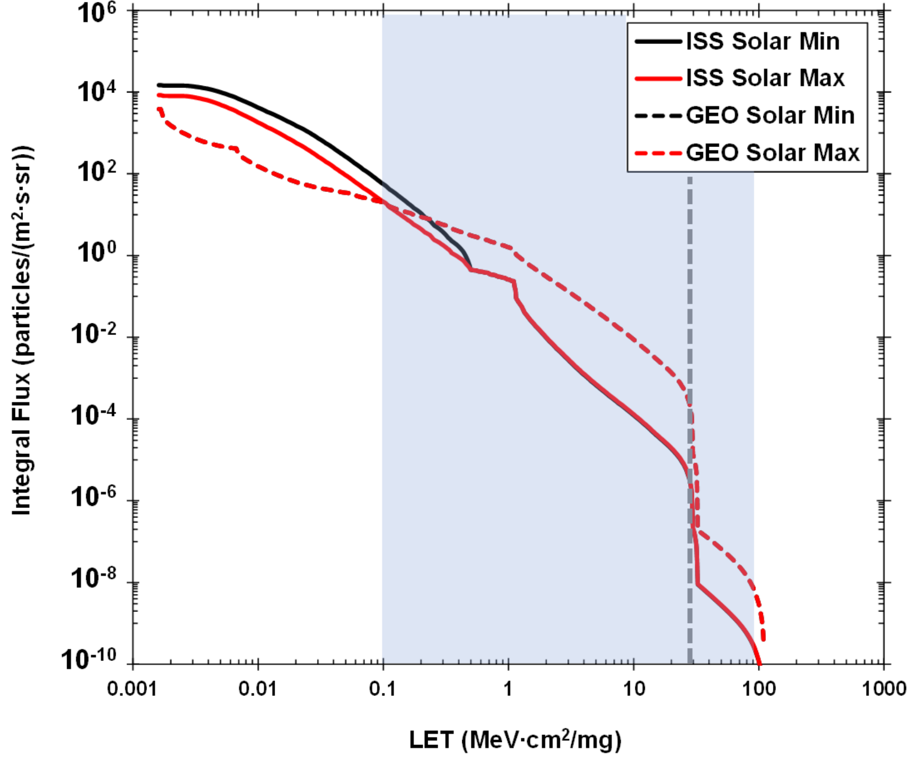

Figure III.2. LET integral flux spectra for an ISS orbit (solid lines) and a GEO orbit (dashed lines) during solar minimum (black) and solar maximum (red). Graphs generated using SPENVIS [17]. The greyed portion of the spectra shows the LET range that conventional heavy ion facilities can achieve.

length of interest. Because semiconductor devices are typically very small compared to a heavy ion's range, only the portion of the LET curve that passes through the device is of interest.

$$Q_{gen,ion} = \frac{q\rho}{E_{ehp}} \int_l LET(x)dx = -\frac{q}{E_{ehp}} \int_l \frac{dE_{elec}}{dx} dx \qquad (III.2)$$

Charge collection from heavy ions occurs as freed carriers move through a *pn* junction. Under low-carrier injection conditions, when the excess minority carrier density is less than the doping density, excess carriers move via diffusion in regions without an electric field and move via drift within an electric field. When the excess minority carrier density is much greater than the doping density, high-carrier injection conditions occur. Large densities of excess carriers near and within *pn* junctions cause the electric field region to be modulated, extending further than under equilibrium conditions, and resulting in the collection of more charge than would be seen in low-carrier injection conditions [49, 50]. This potential modulation is commonly referred to as

"funneling," due to the funnel-like shape of the modulated region from the ion charge-track and is generally thought of as an extension of the depletion region beyond the equilibrium position. However, potential modulation also refers to the perturbation of the internal potential from its nominal condition, as will be seen later in this dissertation. Ions typically result in high-carrier injection conditions [51, 52].

B. Pulsed Lasers

Pulsed lasers have been the subject of investigation for use in SEE testing since the late-1980s [4, 53]. Charge is generated through the absorption of photons, resulting in a heavy ion-like SEE. There are two main types of laser SEE testing, named after the number of photons necessary to create an electron-hole pair. Single photon absorption (SPA) is a linear optical process, generating an electron-hole pair when a single photon is absorbed. Two photon absorption (TPA) is a nonlinear optical process that generates an electron-hole pair when two photons are absorbed nearly simultaneously. SPA only occurs when the photons have energy greater than the bandgap energy of the semiconductor; TPA occurs when the photons have energy less than the bandgap energy, but greater than half the bandgap. These relationships are shown mathematically in Equations III.3 and III.4, where h is Planck's constant, c is the speed of light, E_G is the semiconductor bandgap energy, and ν_X and λ_X are the frequency and wavelength of the photons, respectively. In silicon, SPA occurs when using wavelengths less than 1100 nm and TPA occurs when using wavelengths between 1100 nm and 2210 nm. Figure III.3 shows SPA (top) and TPA (bottom) processes.

$$h \cdot \nu_{SPA} = \frac{hc}{\lambda_{SPA}} > E_G \qquad (III.3)$$

$$E_g > h \cdot \nu_{TPA} = \frac{hc}{\lambda_{TPA}} > \frac{E_G}{2} \qquad (III.4)$$

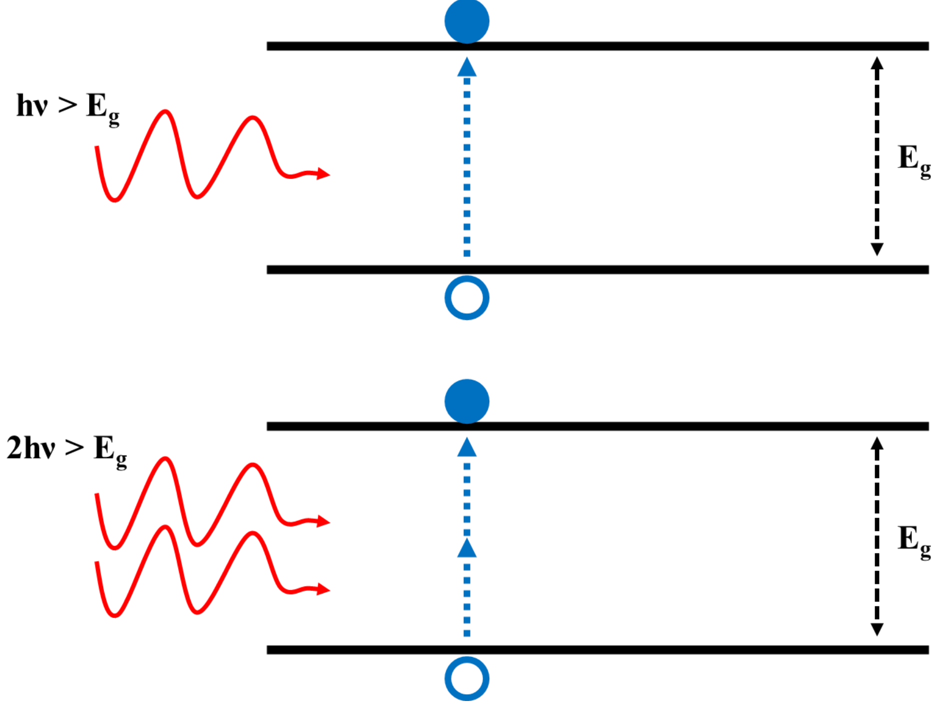

Figure III.3. (Top) SPA. A single photon with energy greater than the semiconductor's bandgap energy is absorbed and creates a single electron-hole pair. (Bottom) TPA. Two photons with a combined energy greater than the semiconductor's bandgap energy are absorbed and create a single electron-hole pair.

As a linear optical process, charge from SPA-induced generation decreases exponentially with depth, following Beer's law for the absorption of light within a material ($I = I_0 e^{-\alpha z}$). The absorption coefficient, α, characterizes how quickly photons are absorbed by a material, and is material and wavelength dependent [54]. More will be said about SPA-induced charge generation in the following subsection on focused X-rays.

Nonlinear optical processes, like TPA, are intensity dependent processes that rely on focused pulsed lasers to achieve necessary photon densities [55]. Focused, femtosecond pulsed lasers allowed for the necessary carrier densities to induced SEEs. Charge generation from TPA is a complex process involving the temporal and spatial evolution of a laser pulse as it propagates through a semiconductor. It can be described by three coupled differential equations the describe the temporal and spatial evolution of the intensity, phase, and free carriers of the laser pulse [4, 56].

$$\frac{dI(r,z)}{dz} = -\alpha_0\, I(r,z) - \beta_2\, I^2(r,z) - \sigma_{FCA}\, N(r,z)\, I(r,z) \qquad (III.5)$$

$$\frac{d\Phi(r,z)}{dz} = k_0\, n_0 + k_0\left(n_2\, I(r,z,t) + \Delta n_{FCR}\, N(r,z,t)\right) \tag{III.6}$$

$$\frac{dN(r,z)}{dt} = \frac{\alpha_0}{\hbar\omega} I(r,z) + \frac{\beta_2}{2\hbar\omega} I^2(r,z) - \frac{1}{\tau} N(r,z,t) \tag{III.7}$$

In these equations, I is the intensity, α_0 is the linear absorption coefficient, β_2 is the TPA absorption coefficient, σ_{FCA} is the coefficient of free carrier absorption, N is the number of free carriers, Φ is the phase of the light, k_0 is the vacuum wave vector (2π/λ), n_0 is the refractive index at that wavelength, n_2 is the Kerr coefficient, Δn_{FCR} is the change in refractive index due to free-carrier refraction, and $\hbar\omega$ is the photon energy.

The complexity of TPA-induced charge generation necessitates the use of computer aided tools for modeling the charge generation. Two commonly used tools for TPA-induced SEE modeling are Nonlinear Optical Beam Propagation Method (NLOBPM) [57] and Lumerical Finite-Difference Time-Domain (FDTD) Solutions [58]. Lumerical FDTD Solutions accounts for optical phenomena that can affect charge generation, such as surface reflections and interference [56, 60], and is the tool used in this work. An example output from Lumerical FDTD Solutions is given in Figure III.4, which shows a time-integrated charge generation profile (left) and a line charge profile (right). A 990 pJ laser pulse focused 14 μm into silicon is used for the simulation. Perturbations and a discontinuity at 25 μm in the carrier density are due to change in doping density from lightly doped to heavily doped in the substrate. The perturbations are from reflections at the interface at 25 μm and the discontinuity is from the presence of free carrier absorption in the substrate that is not present in the lightly doped region. The line charge profile is found by radially integrating the time-integrated profile, producing a curve that can be more directly compared to an ion's LET curve. The total amount of charge generated can be found by integrating the time-integrated charge profiles over the desired volume.

Typical focused femtosecond pulsed laser systems use optics that produce a charge generation profile described by Gaussian TPA, as demonstrated in Figure III.4, [61]. Recently, an optical configuration has been developed by the U.S. Naval Research Laboratory (NRL) that uses a quasi-Bessel beam to generate an extended charge generation profile [62]. This work focused on Gaussian TPA pulsed laser experiments and does not evaluate quasi-Bessel beam TPA or SPA pulsed laser techniques.

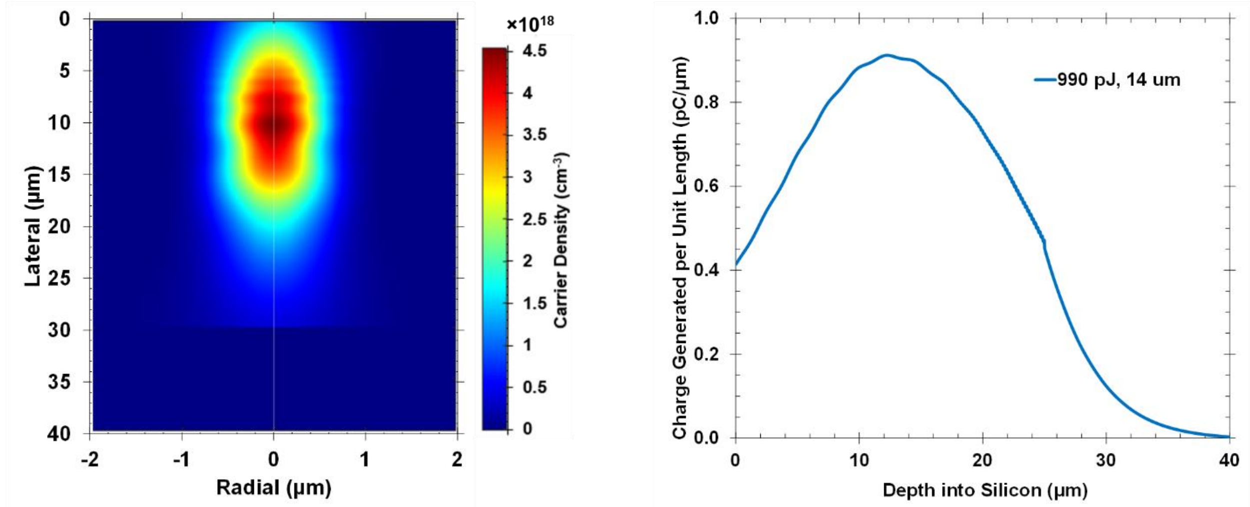

Figure III.4. (Left) 2D, time-integrate carrier density distribution output from Lumerical FDTD Solutions for a 990 pJ laser focused 14 μm into silicon. (Right) Radially integrated line charge distribution of the carrier density distribution, giving the amount of charge generated per unit length.

C. Focused X-Rays

Focused X-rays are a relatively newer SEE testing technique compared to heavy ions and pulsed lasers, gaining interest in the 1990s [63]. Focused X-rays generate charge in semiconductors through SPA, resulting in charge generation curves that follow Beer's Law [64]:

$$\frac{dQ_{gen,x-ray}}{dx} = \frac{E_p}{E_{ehp}} \cdot \alpha e^{-\alpha z} \qquad (III.8)$$

where E_p is the energy of a single X-ray pulse, E_{ehp} is the electron-hole pair creation energy (3.6 eV/ehp in silicon), and α is the absorption coefficient. Table III.1 gives the attenuation lengths, which is equal to $1/\alpha$, for several common semiconductors and metals at various X-ray energies. E_p depends on the X-ray source being used. In this work, Argonne National Lab's Advanced Photon Source (APS) was used, and E_p can be calculated as [64]:

$$E_p = \left(\frac{16}{101.9}\right) \cdot \left(\frac{Calibration\ Constant \cdot Equivalent\ Flux \cdot Scaling\ Factor}{Rep\ Rate}\right) \times Photon\ Energy. \qquad (III.9)$$

$Calibration\ Constant$, $Equivalent\ Flux$, $Scaling\ Factor$, and $Rep\ Rate$ are all parameters that are measured at the facility before testing begins. The amount of charge generated within a region can be found by integrating Equation III.8, resulting in:

$$Q_{gen,X-ray} = \frac{E_p}{E_{ehp}} \cdot (e^{-\alpha z_1} - e^{-\alpha z_2}) \qquad (III.10)$$

where z_1 is the depth closest to the surface of the device (often assumed to be 0) and z_2 is the depth furthest into the semiconductor. Figure III.5 shows the charge generated per unit length profiles for three X-ray energies commonly used at APS (8 keV, 10 keV, and 12 keV).

Table III.1. Attenuation lengths for common materials from [64]

Material/Compound	$1/\alpha$ (μm) @ 8 keV	$1/\alpha$ (μm) @ 10 keV	$1/\alpha$ (μm) @ 12 keV
Silicon	69.6	133.7	228.7
SiC	69.9	134.3	229.8
GaN	31.4	59.4	12.6
$Si_{80}Ge_{20}$	67.2	127.4	55.7
Aluminum	77.6	149.6	256.6
Copper	21.9	5.1	8.2
Tungsten	3.1	5.5	2.5

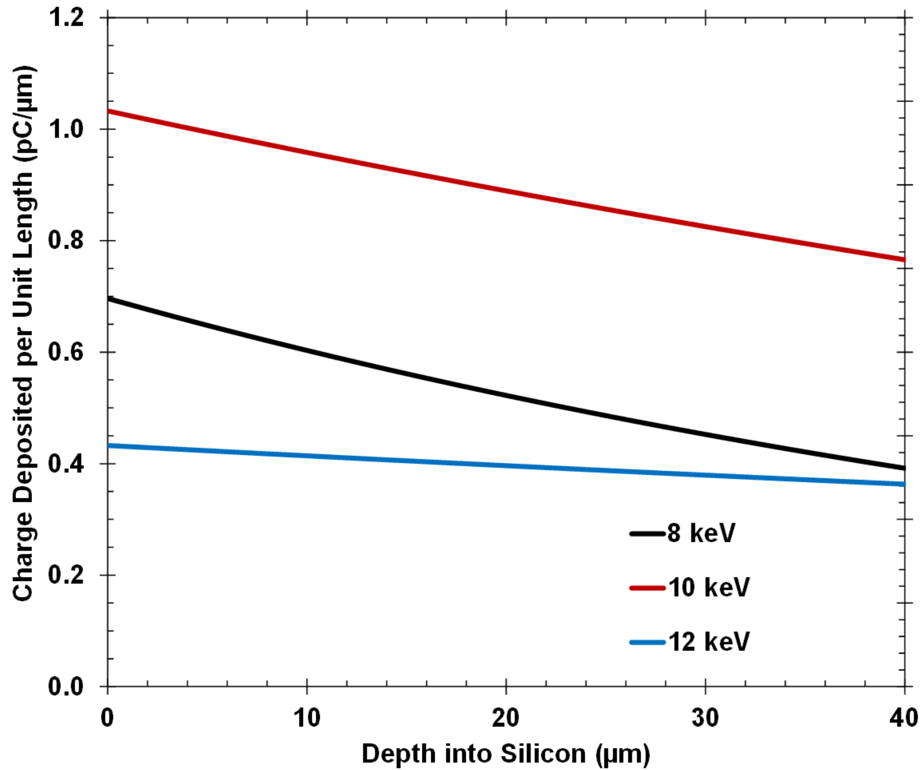

Figure III.5.Charge generated per unit length curves for 8 keV (black), 10 keV (red), and 12 keV (blue) X-ray photon energies at APS. Curves are for pulses with the maximum available flux on July 25, 2019.

D. Current State of Correlating Radiation Sources

As was discussed previously in this chapter, heavy ions are the conventional source for ground-based SEE testing due to their ability to mimic the space radiation environment. However, a combination of the growing space industry and aging facilities has led to an availability shortage [3]. There are also technical limitations to heavy ions that are increasingly problematic as devices become smaller and denser. Most heavy ion facilities are broad beam facilities, with target spot sizes on the order of an inch or more [44-47], making it difficult to identify specific areas on a chip or circuit that are exhibiting SEEs. Microbeam facilities [65-67], with beam spot sizes on the order of micrometers, are used for more targeted SEE experiments [68-70], but still suffer from accessibility issues and produce less energetic ions.

Pulsed laser and focused X-ray testing have been extensively studied as alternative methods to heavy ion SEE testing, both to help alleviate the facility shortage and for the advantages they offer over heavy ions [4, 61, 71-75]. Both alternative methods produce smaller spot sizes than ion beam

facilities, on the order of micrometers, allowing for increased spatial resolution when investigating SEEs. Capitalizing on this, numerous studies have been done using pulsed lasers and focused X-rays for spatial mapping of SEE sensitive regions in devices [76-79]. The lateral confinement of generated charge from Gaussian TPA laser pulses (see Figure III.4 for an example) allows for 3D mapping of sensitive areas, targeted SEE testing of buried structures, and through-substrate SEE testing [80, 81]. Increased availability of these alternative sources makes them useful for scientific exploration of SEEs in new and emerging technologies, from highly scaled FinFETs to III-V devices [59, 82-90].

The increased prevalence of alternative testing methods has led to the desire to correlate these alternative methods to heavy ions, thereby leading to a correlation to the space radiation environment. Initial correlation methods were straightforward comparisons of results, wherein experiments from multiple SEE generation methods would be performed on the same device and the results compared [91-96]. To pave a path toward predictive correlation methods, much work has gone into simulating the alternative testing methods, particularly the pulsed laser [97-101]. These simulations show good agreement with experimental results and allow for more detailed understanding of the physical mechanisms at play with the different radiation sources. Research efforts have now switched to developing more predictive correlation methods through a variety of approaches, including through the development of mathematical relationship between the sources [102, 103], creating laser charge generation profiles that look more like heavy ion profiles [62, 104], and by comparing the physical mechanisms behind observed differences [105]. Limitations of the alternative sources also need to be considered when evaluating correlation efforts. Pulsed lasers are limited in their ability to penetrate through metal layers and generate charge in oxides; focused X-rays can lead to significant amounts of total ionizing dose accumulation and have significantly longer pulse durations than ions or pulsed lasers. Overall, it may prove that these techniques are not direct substitutions for each other, but instead enhance the overall ability for SEE mechanism exploration.

This work examines the physical mechanisms responsible for observed differences in SET shape from heavy ion, pulsed laser, and focused X-ray SEE experiments in an epitaxial silicon diode. While the results shown here are not directly generalizable to all devices, they highlight the importance of understanding collection and carrier transport mechanisms when comparing different radiation sources.

CHAPTER IV

SETUP AND PROCEDURES

This work uses an epitaxial silicon diode manufactured by the Beijing Microelectronics Technology Institute (BMTI) as a test structure to explore the physical mechanisms responsible for observed differences in heavy ion-, pulsed laser-, and focused X-ray-induced SET shapes. Sentaurus technology computer aided design (TCAD) simulations [106] were used to verify the conclusions drawn from experiments and identify possible mechanisms behind them.

Adapted with permission from K. L. Ryder *et al.*, "Comparison of Sensitive Volumes Associated with Ion- and Laser-Induced Charge Collection in an Epitaxial Silicon Diode," *IEEE Trans. Nucl. Sci.*, vol. 67, no. 1, pp. 57-62, Jan. 2020 and K. L. Ryder *et al.*, "Comparison of Single Event Transients in an Epitaxial Silicon Diode Resulting from Heavy Ion-, Focused X-Ray-, and Pulsed Laser-Induced Charge Generation," *IEEE Trans. Nucl. Sci.*, vol. 68, no. 5, pp. 626-633, May 2021.

A. Experimental Setup

1) Diode Test Structure

The epitaxial silicon diode shown in Figure IV.1 was used as the test structure for this work. The general device structure is shown on the left and a detailed doping profile is shown on the right. The diode's active region, the p^+ layer and n^- epitaxial layer, lies on top of a heavily doped n^+ substrate which limits the amount of potential modulation [108, 109] that can occur. The diode is 2.2 mm^2 and 220 μm thick. The top metal contact has 18 holes that are 154 μm^2 each; the total area of the holes account for ~0.1% of the total contact area. These holes allow for direct illumination of the silicon near the metallurgical junction, allowing for top-side pulsed laser testing. The holes in the metallization are small enough to perturb the laser profile via beam attenuation and diffraction when the laser is focused far from the surface of the device. Effects resulting from the optical perturbations and surface reflections on the silicon are accounted for in the optical simulations when estimating the charge generated by laser pulses.

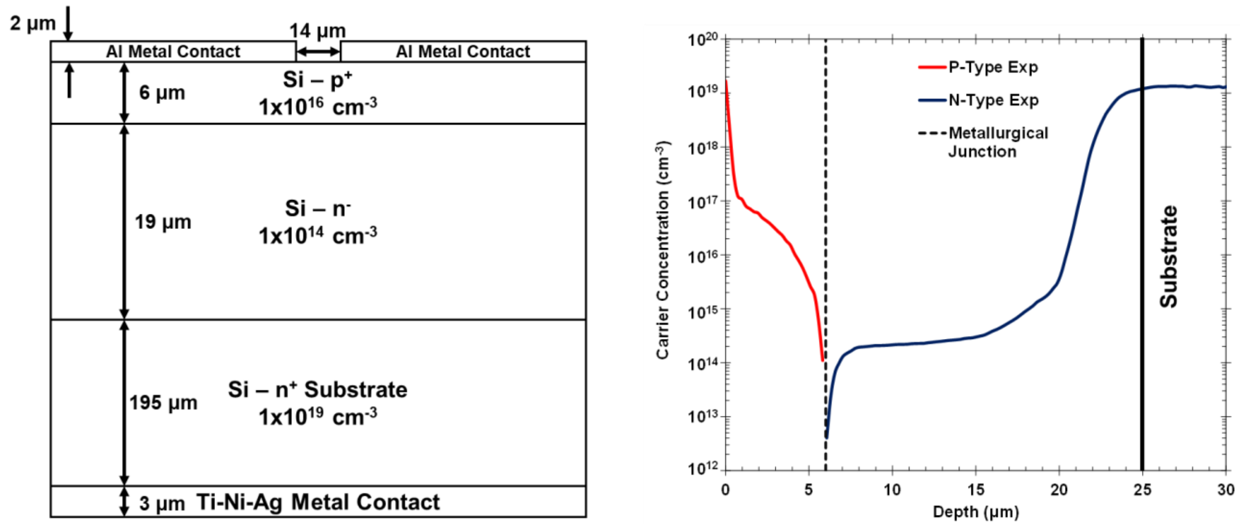

Figure IV.1. Basic drawing of diode test structure (left) and detailed doping profile (right). The diode has a 25 µm active region (p^+ and n^- layers) that lies on top of heavily doped substrate. The metallurgical junction occurs approximately 6 µm into the silicon. The vertical dashed and solid lines on the doping profile show the location of the junction and the substrate, respectively.

The diode was reverse biased at 5 V and 90 V, resulting in depletion region widths of 5.5 µm and 14.7 µm, respectively. These bias conditions allow for exploration of the effects of different electric field strengths and charge collection mechanisms. Figure IV.2 shows the band diagrams for the diode at bias conditions of 0 V (top), -5 V (bottom left), and -90 V (bottom right). The depletion region of the -90 V bias condition is closer to the heavily doped substrate region than the -5 V depletion region, which truncates the amount of lateral potential modulation that occurs.

2) Experimental Conditions

A high-speed transient capture setup was used with 12.5 GHz bias tees, 40 GHz Gore cables, and custom milled high-speed packages for all the experiments. More detailed descriptions of the setup and packages and be found in [110] and [111]. Different oscilloscopes were used for heavy ion (12.5 GHz Tektronix), pulsed laser (16 GHz Tektronix), and focused X-ray (16 GHz Tektronix) experiments, all with bandwidths equal to or greater than that of the bias tees. Ion experiments were run in vacuum, while laser and X-ray experiments were run in air. Figure IV.3 gives a schematic of the general setup, including the connections for in-vacuum testing for ions.

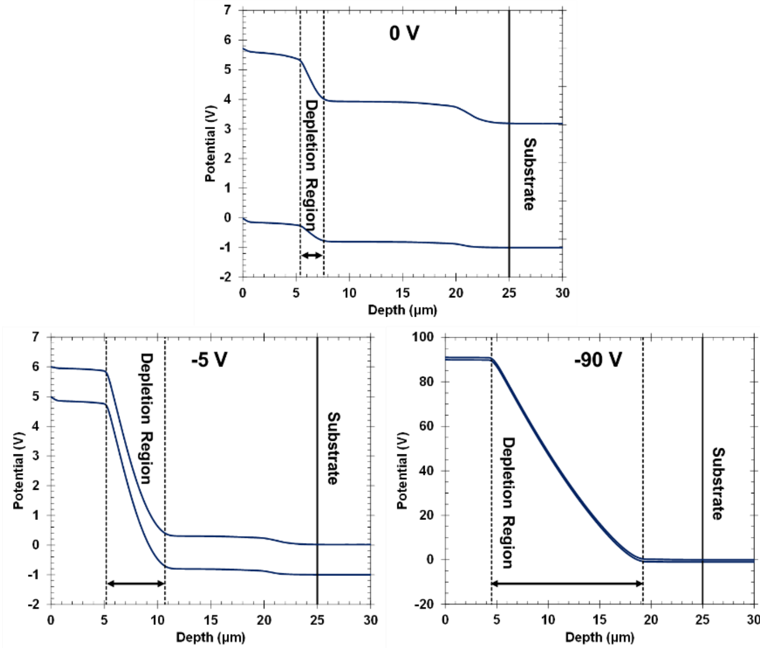

Figure IV.2. Band diagrams of the diode biased at 0 V (top), -5 V (bottom left), and -90 V (bottom right). The dashed lines with the arrow between show the depletion region and the solid vertical line shows the beginning of the substrate. These diagrams were made using TCAD.

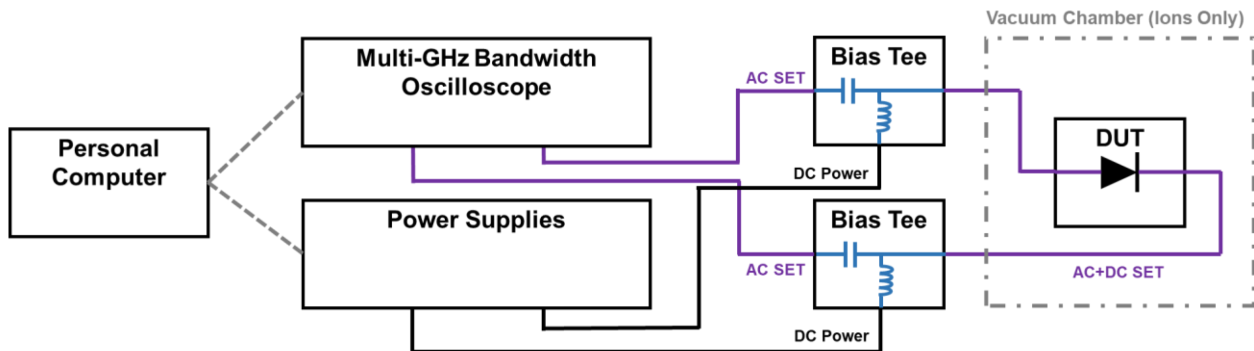

Figure IV.3. Schematic of experimental setup. All devices were mounted in custom high-speed packages. The purple lines represent the high-speed connections for the SET path from device to oscilloscope. The black lines represent the BNC power connections. A personal computer is used to control the power supplies via ethernet connection and to collect data from the oscilloscope via USB connection.

Heavy ion experiments were performed at Lawrence Berkley National Lab's (LBNL) 88" cyclotron [44] using the 10 MeV/u cocktail. All experiments were performed under vacuum. A 100 µm think stainless-steel pinhole (200 µm diameter) was used to isolate ion strikes to the center of the device. For all ions, the flux was approximately 10^7 particles·cm^{-2}·s^{-1}. Three ions were used for the experiments: xenon, copper, and silicon. These ions have different LETs and ranges in silicon, though they are all long-range ions that stop well outside the diode's active region.

Table IV.1 summarizes information on the ions and Figure IV.4 shows the ions' LET curves. Charge generated in active region was calculated by integrating each ion's LET curve using Equation III.2 over 25 μm, the diode's active region. For heavy ion testing, 10,000 SETs were captured for each LET and bias condition.

Table IV.1. LBNL heavy ions used for testing

Ion	Energy (MeV)	Surface Incident LET ($MeV \cdot cm^2/mg$)	Range in Silicon (μm)	Range in Stainless Steel (μm)	Charge Generated in Active Region (pC)
Xe	1230	59	90	35	15.9
Cu	660	21	108	41	5.84
Si	29	6	142	54	1.65

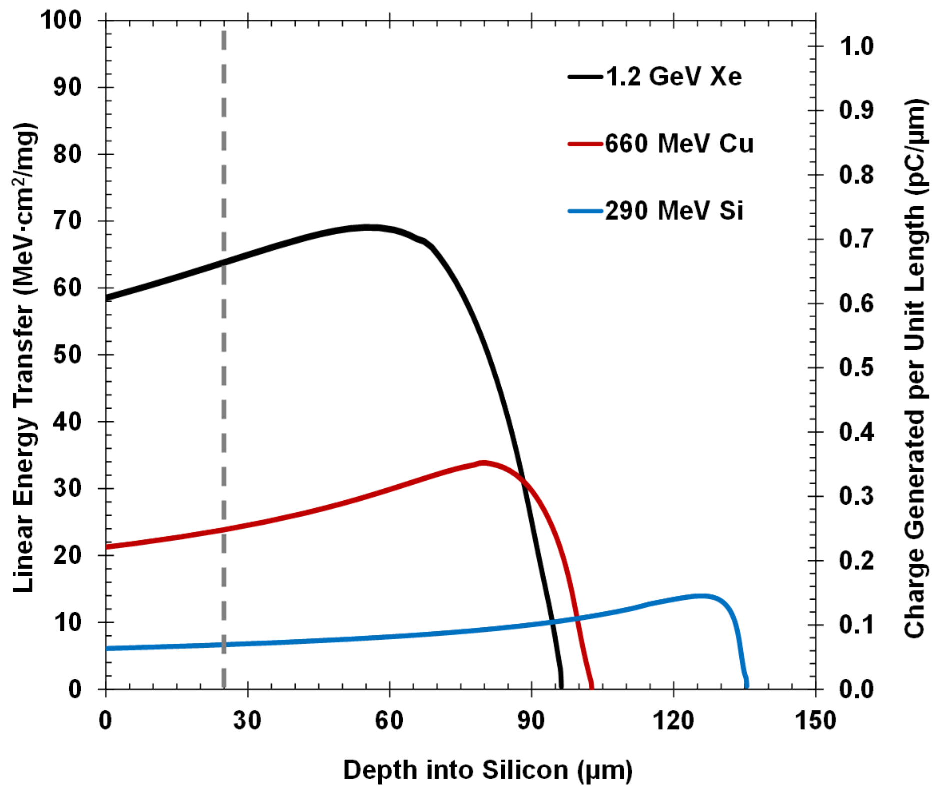

Figure IV.4. LET curves for the xenon (black), copper (red), and silicon (blue) ions used during heavy ion testing. LET was converted to charge generated on the right y-axis. The dashed grey line shows the cutoff for integration.

TPA pulsed laser experiments were done at the Naval Research Lab's (NRL) Ultrafast Laser Facility. Experiments were performed using laser pulses with a Gaussian input beam profile, full width at half maximum (FWHM) spot size diameter of 1.36 μm, and FWHM temporal width of 130 fs [112]. The depth of focus for this laser configuration is approximately 8.1 μm. Three laser pulse energies were used during testing: 400 pJ, 750 pJ, and 990 pJ. A series of measurements made by changing the depth of the laser focus within a device, called a depth scan, was performed for each pulse energy and bias condition [60]. Table IV.2 summarizes information on the pulsed laser testing conditions, Figure IV.5 shows the amount of charge generated versus focal position for all pulse energies, and Figures IV.6 – 8 show the charge generated per unit length curves for the pulse energies and focal positions used. The 0 μm position in these figures corresponds to a focal position at the surface of the silicon of the diode's anode. Lumerical FDTD Solutions was used to create the curves. The discontinuity that occurs in the profiles at 25 μm is due to interactions with the heavily doped substrate. For pulsed laser testing, 200 SETs were captured for each focal position, pulse energy, and bias condition.

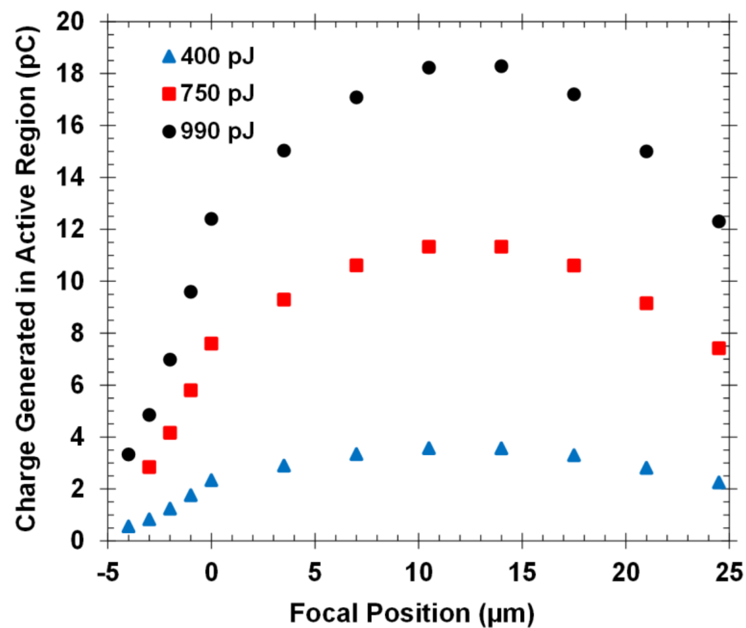

Figure IV.5. Charge generated in diode's active region versus focal position for the pulsed laser at 990 pJ (black circles), 750 pJ (red squares), and 400 pJ (blue triangles). A focal position of 0 μm corresponds to the focus being at the surface of silicon on the diode's anode.

Table IV.2. NRL TPA laser testing conditions used

Pulse Energy (pJ)	Focal Positions (µm)	Charge Generated in Active Region (pC)
990	-4, -3, -2, -1, 0, 3.5, 7, 10.5, 14, 17.5, 21, 24.5	3.3, 4.9, 7.0, 9.6, 12.4, 15.0, 17.1, 18.2, 18.3, 17.2, 15.0, 12.3
750	-3, -2, -1, 0, 3.5, 7, 10.5, 14, 17.5, 21, 24.5	2.8, 4.2, 5.8, 7.6, 9.3, 10.6, 11.3, 11.3, 10.6, 9.2, 7.4
400	-4, -3, -2, -1, 0, 3.5, 7, 10.5, 14, 17.5, 21, 24.5	0.6, 0.8, 1.2, 1.8, 2.3, 2.9, 3.3, 3.6, 3.6, 3.3, 2.8, 2.3

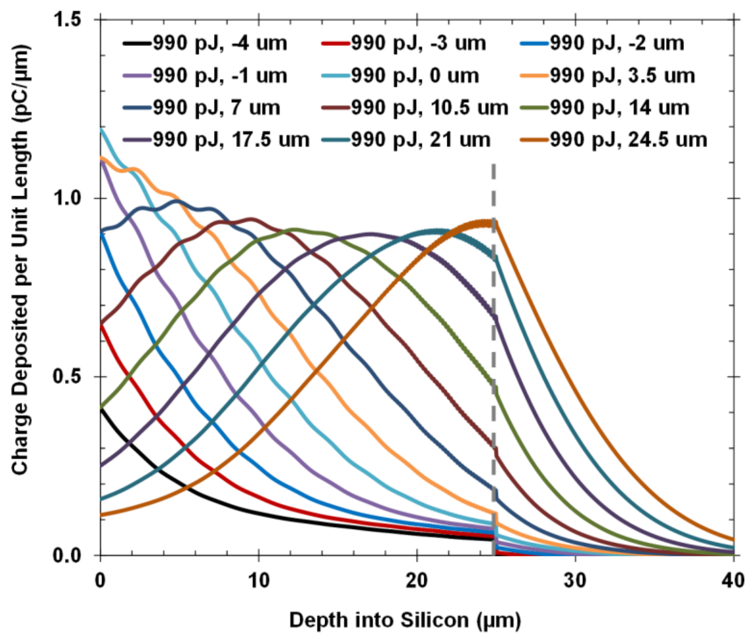

Figure IV.6. Charge generated per unit length curves for the 990 pJ focal positions. Focal positions run from -4 µm out of the silicon to 24.5 µm into the silicon. The dashed grey line shows the cutoff for integration.

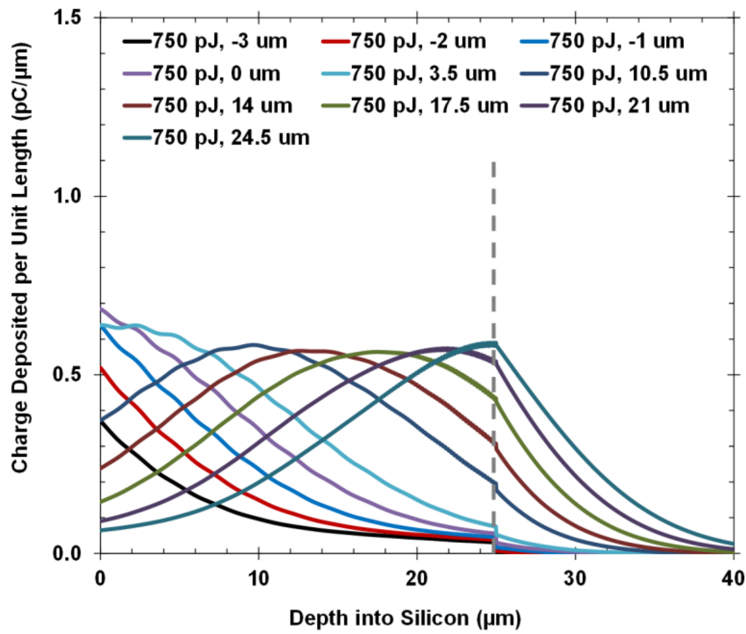

Figure IV.7. Charge generated per unit length curves for the 750 pJ focal positions. Focal positions run from -3 µm out of the silicon to 24.5 µm into the silicon. The dashed grey line shows the cutoff for integration.

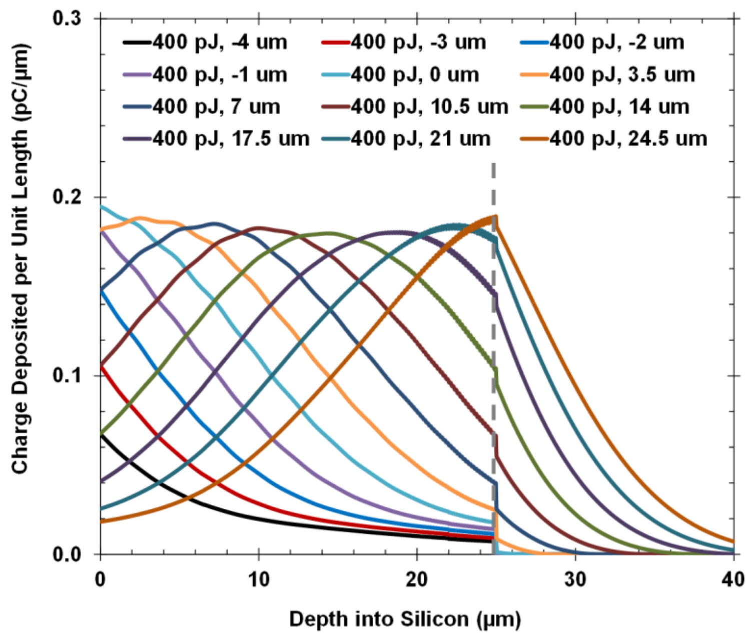

Figure IV.8. Charge generated per unit length curves for the 400 pJ focal positions. Focal positions run from -4 µm out of the silicon to 24.5 µm into the silicon. Note that the y-axis scale for this graph is much smaller than the scale on the 750 pJ and 990 pJ graphs. The dashed grey line shows the cutoff for integration.

Argonne National Lab's Advances Photon Source (APS) was used to perform focused X-ray experiments. Photon energies of 8 keV, 10 keV, and 12 keV were used. The flux of the pulses (number of photons per pulse) was varied by inserting attenuators in the beamline before the diode, resulting in full flux, ½ flux, and ¼ flux testing conditions for each photon energy. The X-ray pulses have a FWHM spot size of 1.7 µm × 1.9 µm, FWHM pulse width of 120 ps, and repetition rate of 424.3 Hz [64]. Table IV.3 summarizes information on the focused X-ray testing conditions and Figures IV.9 – 11 show the charge generated per unit length curves for the photon energies and fluxes used. Equation III.8 was used to create the curves. For focused X-ray testing, 500 SETs were captured for each photon energy, flux, and bias condition.

Table IV.3. APS focused X-ray testing conditions used

Photon Energy (keV)	Flux (photons/pulse)	Charge Generated in Active Region (pC)
8	4.5×10^4	4.78
8	7.8×10^4	8.35
8	1.4×10^5	14.62
10	8.3×10^4	6.26
10	1.7×10^5	13.05
10	3.1×10^5	23.54
12	5.4×10^4	2.96
12	1.0×10^5	5.52
12	1.9×10^5	10.24

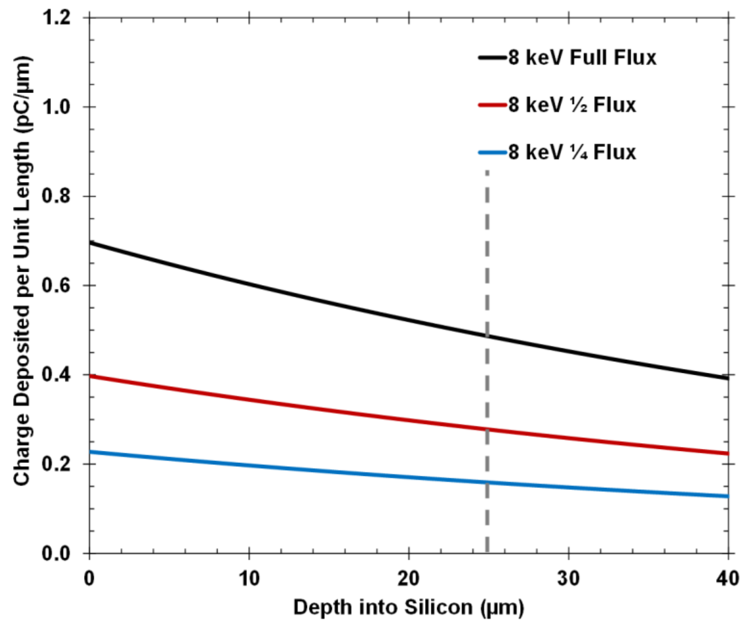

Figure IV.9. Charge generated per unit length curves for the 8 keV X-ray pulses at full flux (black), ½ flux (red), and ¼ flux (blue). The dashed grey line shows the cutoff for integration.

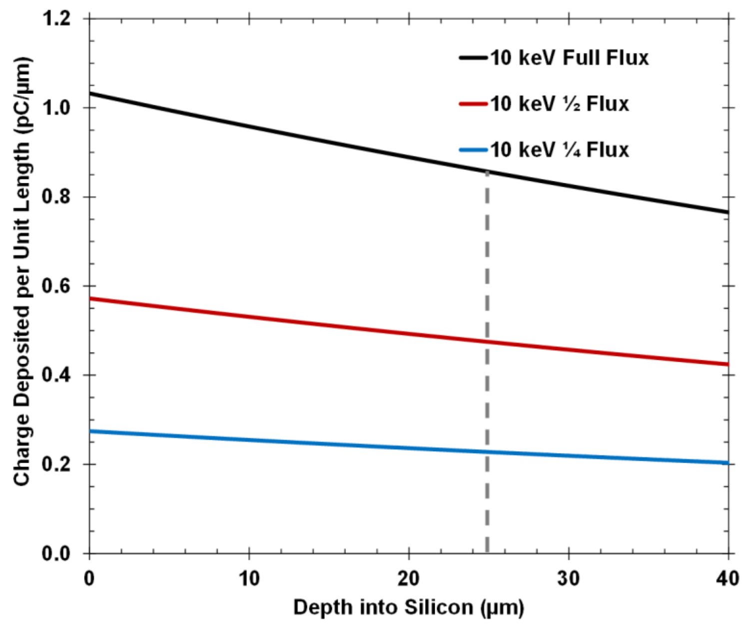

Figure IV.10. Charge generated per unit length curves for the 10 keV X-ray pulses at full flux (black), ½ flux (red), and ¼ flux (blue). The dashed grey line shows the cutoff for integration.

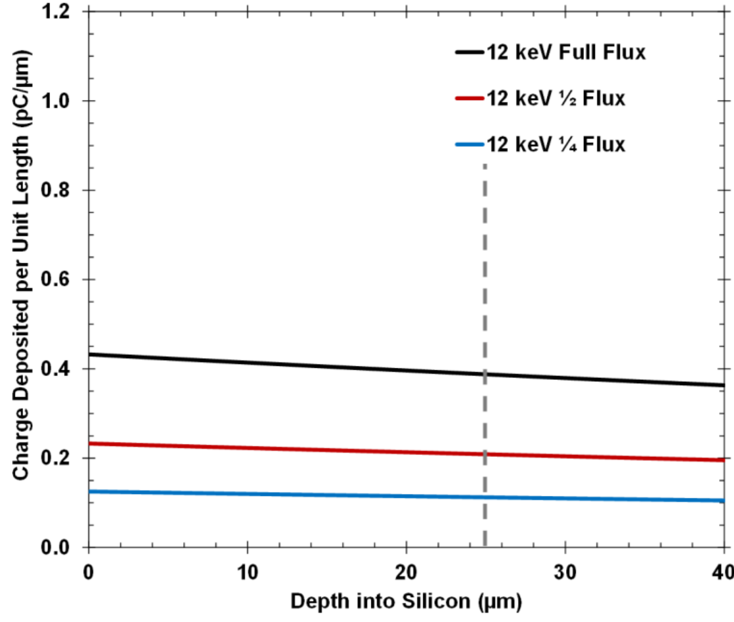

Figure IV.11. Charge generated per unit length curves for the 12 keV X-ray pulses at full flux (black), ½ flux (red), and ¼ flux (blue). The dashed grey line shows the cutoff for integration.

B. Data Processing Methodology

Each of the experimental SETs was fit to a double exponential function to remove noise and ensure consistency when determining SET shape characteristics. Given the size of the diode, the double exponential function from [23, 27] was used and is given in Equation IV.1. In Equation IV.1, $b + ct$ is used to capture the noise associated with the setup, I is proportional to the amplitude, a is the horizontal offset on the oscilloscope (time the SET starts), and τ_1 and τ_2 are related to the rise and fall times. Before SET shape analysis is done, the noise component of the fitted SET is removed, and the fitted SET become Equation IV.2, where $f_2(t)$ is in mA and t is in ns. Figure IV.12 shows an experimental SET (black) from each of the charge deposition methods and its associated fitted SET (red). The fitted SETs have R^2 values ≥0.97, which is considered a good fit, and the lowest observed R^2 value was 0.7. It should be noted that $f_2(t) = 0$ when $t < a$.

$$f_1(t) = b + ct + I\left(\mathrm{e}^{-\tau_1(t-a)} - e^{-\tau_2(t-a)}\right) \qquad (IV.1)$$

$$f_2(t) = I\left(e^{-\tau_1(t-a)} - e^{-\tau_2(t-a)}\right) \qquad (IV.2)$$

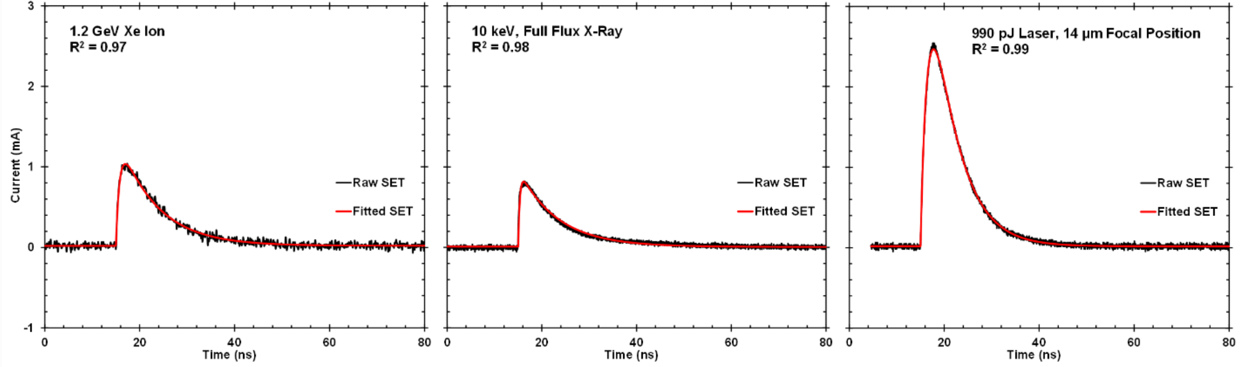

Figure IV.12. Typical SET (black) and its associated fitted SET (red) from a heavy ion (left), focused X-ray (middle), and pulsed laser (right) experiment. All SETs are from the -5 V bias condition. The fits shown here have R^2 values ≥0.97.

Once $f_2(t)$ was found for an SET, the peak current, collected charge, rise time, fall time, and FWHM (PC, CC, RT, FT, and FWHM, respectively) were calculated. Peak current is found by taking the maximum of $f_2(t)$, Equation IV.3. Collected charge is found by integrating $f_2(t)$, using the Trapezoidal rule, Equation V.4. The error associated with the Trapezoidal rule is inversely proportional to the square of number of increments; given that the SETs all contain at least 2000 points, the error is considered negligible. While a closed form solution exists for the rise time, it does not exist for the fall time or FWHM. So, it was decided to use the same analytical solution for all three characteristics for consistency, by solving for the time at which $f_2(t)$ is equal to a value or when the difference between $f_2(t)$ and that value becomes negative. Equations IV.5, IV.6, and IV.7 show this logic for rise time, fall time and FWHM, respectively. Rise time is calculated as the time it takes for the fitted SET to go from 1% of the peak value to the peak value. Fall time is the time it takes to go from the peak value to 1% of the peak. FWHM is the time between the 50% of peak values. The python data-processing code used for the mathematical calculations can be found in Appendix A.

$$PC = \max\left(f_2(t)\right) \qquad (IV.3)$$

$$CC = \int f_2(t)dt \approx \sum_i (x_{i+1} - x_i) * \frac{f_2(x_i) + f_2(x_{i+1})}{2} \qquad (IV.4)$$

$$RT_{left\ bound} = t\ |[\ (f_2(t) - 0.01PC) = 0\ ] \cup [(f_2(t) - 0.01PC) \times (f_2(t) - 0.01PC) < 0] \quad (IV.5)$$

$$FT_{right\ bound} = t\ |[\ (f_2(t) - 0.01PC) = 0\ ] \cup [(f_2(t) - 0.01PC) \times (f_2(t) - 0.01PC) < 0] \quad (IV.6)$$

$$FWHM_{bound} = t\ |[\ (f_2(t) - 0.5PC) = 0\ ] \cup [(f_2(t) - 0.01PC) \times (f_2(t) - 0.5PC) < 0] \quad (IV.7)$$

C. Simulation Device, Setup, and Models

A full-scale replica of the diode structure was used for the TCAD simulations to better capture the junction capacitance of the diode. A cross section of the simulated diode structure is shown in Figure IV.13. The simulated diode is 220 μm thick (y-direction) and has a radius of 846 μm (x-direction). Because two-dimensional cylindrical simulations were performed, the radius of the diode needed to be a factor of $1/\sqrt{\pi}$ the experimental width for the simulated and experimental areas to be equivalent. The doping profiles shown in Figure IV.1 were used to create the simulated doping profiles. Appendix B shows the agreement between the simulated doping profile and experimental doping profiles. Table IV.4 shows the mobility and recombination models used during the simulations. The Shockley-Read-Hall (SRH) recombination lifetimes were modified by a factor of ×0.125, allowing for good agreement between the experimental and simulation reverse leakage currents, shown in Figure IV.14. The disagreement between the simulated IV curves and experimental IV curves at voltages near 0 V is due to the auto-scaling for the resolution of the parameter analyzer used to make the measurements. Appendix C provides tables of the default model parameters used during the simulations; values were taken from the TCAD user manual [113].

Table IV.4. Physics models used in Sentaurus TCAD simulations

Mobility	Philips Unified Model, High Field Saturation
Recombination-Generation	SRH: Doping Dependence, SRH: Electric Field Dependence, Auger, Avalanche

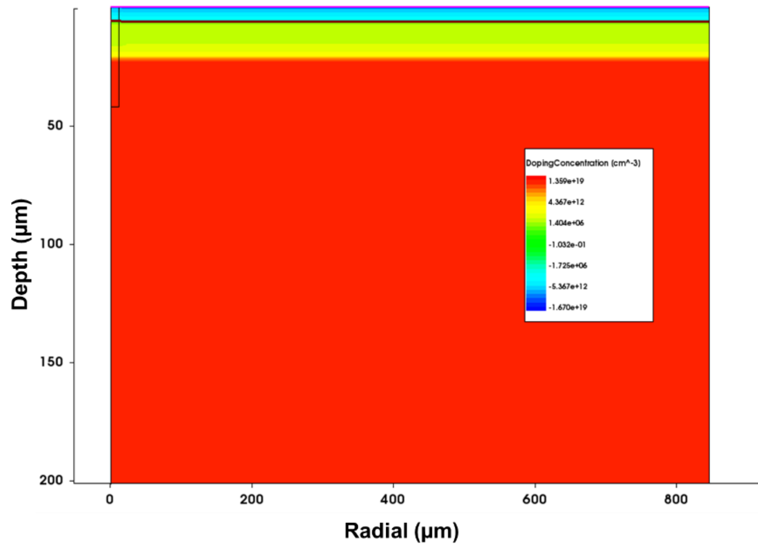

Figure IV.13. Two-dimensional cross-section of the simulated diode structure. The x-y plane shown here is rotated about the y-axis during simulations to produce a 2D cylindrical simulation.

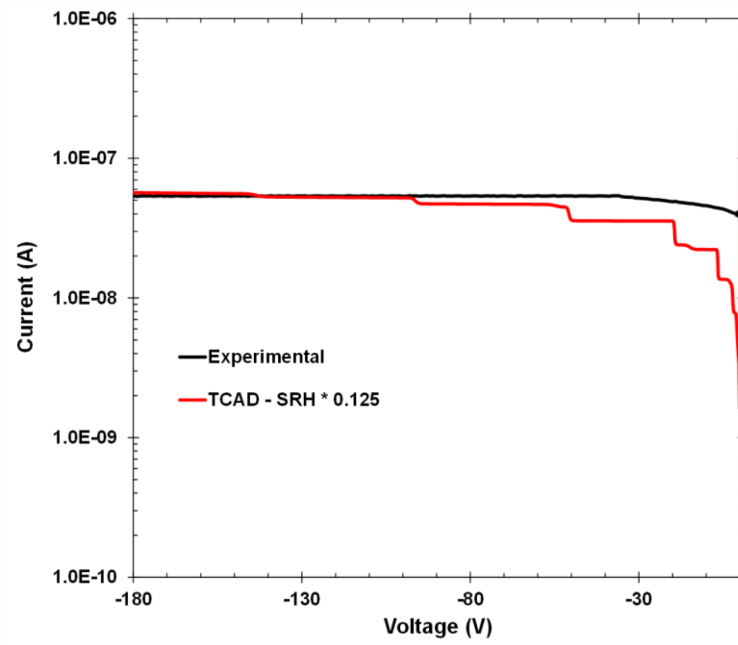

Figure IV.14. Experimental (black) and TCAD simulated (red) IV curves. The reverse leakage currents show good agreement.

Heavy ion, pulsed laser, and focused X-rays transient simulations were run using TCAD's mixed mode simulation, allowing for the experimental bias tees to be accounted for in a circuit model. Figure IV.14 shows the circuit diagram for the bias tee on the anode of the diode [114]. A 50 Ω resistor is used to emulate the 50 Ω impedance of the oscilloscopes. Simulated SETs are measured off node N2, analogous to measuring the current on the oscilloscope. An identical bias tee is connected to the diode's cathode, with the bias is set to ground. While the SETs reported here were measured off N2, it was confirmed that the current through the diode and the current at N2 are equal.

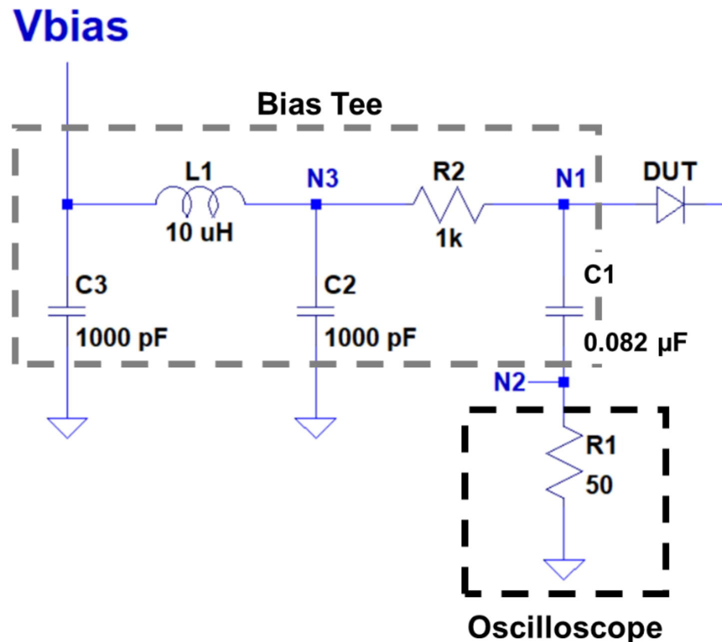

Figure IV.15. Circuit schematic of the bias tee attached to the diode's anode. The components in the dark grey box form the bias tee, which has a dominant capacitance of 82 nF and an inductance of 10 μH. The black box denotes the oscilloscope connections, which has a 50 Ω impedance. The cathode bias tee is identical [114].

The charge generation curves from ***Experimental Conditions*** (Figures VI.4, VI.6 – VI.7, and VI.9 – VI.11) were used as the SEE stimuli in the simulations. TCAD's *HeavyIon* physics model was used to generate the heavy ion-based SETs using the standard $1/e^2$ time envelope of 4 ps and a FWHM radial extent of 42 nm, the default values for heavy ions. The pulsed laser and focused X-ray charge generation distributions were imported as *tdr* files using TCAD's *OpticalGeneration* physics model. The $1/e^2$ time envelopes for the pulsed laser and focused X-ray are based on their

experimental pulse lengths (***Chapter IV.A.2***), and are 20 ps and 144 ps, respectively. The radial extent of their charge profiles was determined by the optical simulations and calculations that created the *tdr* profiles (see ***Chapter 2.A***) and is not an input in the TCAD physics model. The SETs resulting from these simulations show good agreement with the experimental SETs, demonstrated in Figures VII.4 and VII.5 that compare the experimentally averaged SET with the TCAD SET. Plus, and minus one standard deviation of the experimentally averaged SETs is shown in grey, showing the consistency of experimental SETs.

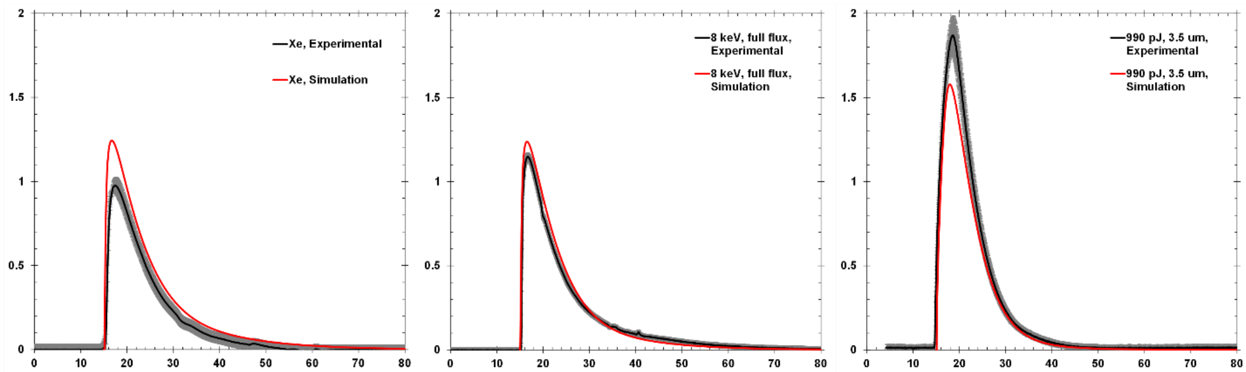

Figure IV.16. Experimentally averaged SET (black) and TCAD simulated SET (red) for the Xe ion (left), 8 keV full flux X-ray (middle), and 990 pJ laser at a focal position of 3.5 µm (right) at a bias of -5 V.

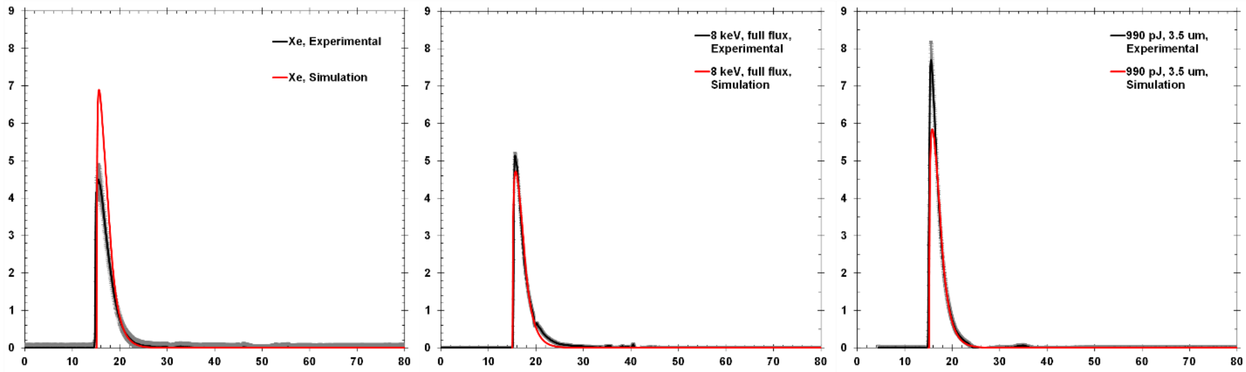

Figure IV.17. Experimentally averaged SET (black) and TCAD simulated SET (red) for the Xe ion (left), 8 keV full flux X-ray (middle), and 990 pJ laser at a focal position of 3.5 µm (right) at a bias of -90 V.

CHAPTER V

EXPERIMENTAL RESULTS FOR EACH RADIATION SOURCE

Experimental results from heavy ion (***V.A***), pulsed laser (***V.B***), and focused X-ray (***V.C***) SET experiments on the diode are presented. Peak current, collected charge, transient rise time, transient fall time, and transient FWHM are given as functions of charge generated in the diode's active region for both bias conditions. All data have error bars showing ±1 standard deviation from the mean. Basic analysis of the data is presented for each radiation source, while a comparative analysis is given in ***Chapter VI***. Some results presented here have been published previously in [60, 105, 107]. Sentaurus TCAD simulation analysis is presented, where applicable, to augment experimental evidence.

Adapted with permission from K. L. Ryder *et al.*, "Comparison of Sensitive Volumes Associated with Ion- and Laser-Induced Charge Collection in an Epitaxial Silicon Diode," *IEEE Trans. Nucl. Sci.*, vol. 67, no. 1, pp. 57-62, Jan. 2020 and K. L. Ryder *et al.*, "Comparison of Single Event Transients in an Epitaxial Silicon Diode Resulting from Heavy Ion-, Focused X-Ray-, and Pulsed Laser-Induced Charge Generation," *IEEE Trans. Nucl. Sci.*, vol. 68, no. 5, pp. 626-633, May 2021.

A. Heavy Ion

Figures V.1 and V.2 give the experimental collected charge and peak current results from the heavy ion experiments (For all heavy ion data, results from the -5 V bias condition are denoted by closed black circles, while the -90 V bias results are denoted by open black circles). Both collected charge and peak current have a linear relationship with charge generated, and both increase with increased reverse bias. The rate of collected charge versus charge generated (also called "collection efficiency") is 0.64 at -5 V and 1.00 at -90 V, resulting in a 56% increase in collection efficiency. A unity collection efficiency is shown by the dashed grey line in Figure V.1. An increase in collection efficiency is related to an increase in the collected charge sensitive volume, which will be discussed further in ***Chapter VI***. The ratio of peak current to charge generated is 0.06 mA/pC at -5 V and 0.31 mA/pC at -90 V, resulting in a 417% increase. The increases in both collection

efficiency and peak current are consistent with the stronger electric fields associated with the larger reverse bias condition.

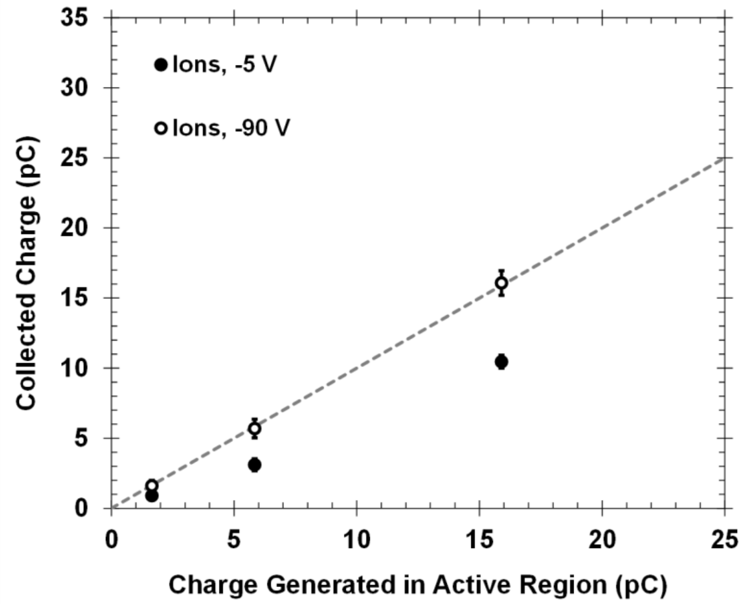

Figure V.1. Heavy ion-induced collected charge as a function of charge generated for -5 V (closed circles) and -90 V (open circles) bias conditions. Collected charge shows a linear relationship with charge generated.

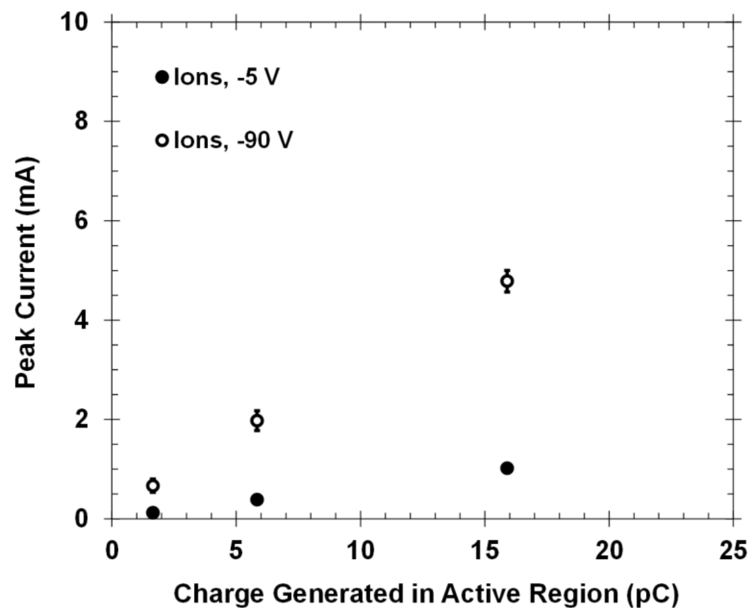

Figure V.2. Heavy ion-induced peak current as a function of charge generated for -5 V (closed circles) and -90 V (open circles) bias conditions. Peak current shows a linear relationship with charge generated.

Figures V.3 – 5 show the experimental transient rise time, fall time, and FWHM. The three timing characteristics all show similar trends with respect to both charge generated and bias condition. There is an increase in timing characteristics as the generated charge increases, between 27% and 40%, and a decrease with increased reversed bias, between 57% and 70%. The decrease in timing characteristics with increased reverse bias is consistent with the stronger electric fields, and therefore greater amount of drift, associated with the larger reverse bias condition. The increase in timing characteristics with increased charge generated indicates a decrease in electric field strength due to increased potential modulation.

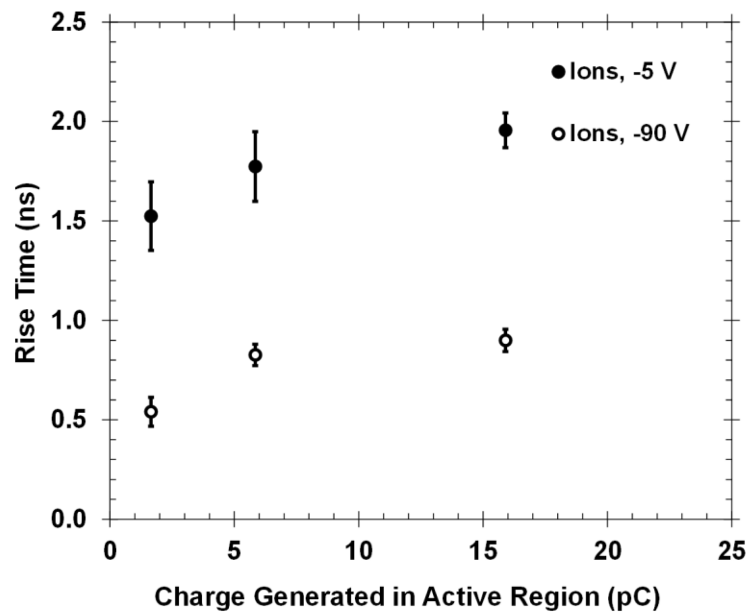

Figure V.3. Heavy ion-induced transient rise time as a function of charge generated for -5 V (closed circles) and -90 V (open circles) bias conditions. Rise time decreases at as reverse bias increases.

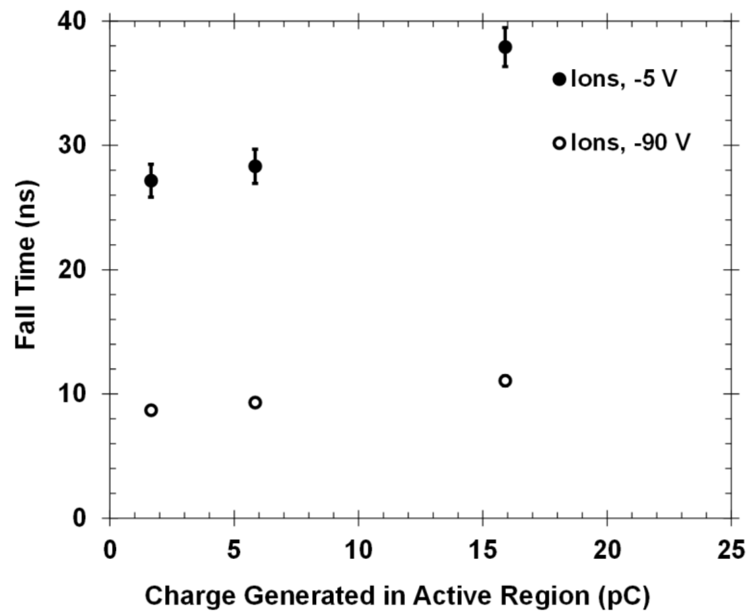

Figure V.4. Heavy ion-induced transient fall time as a function of charge generated for -5 V (closed circles) and -90 V (open circles) bias conditions. Fall time decreases at as reverse bias increases.

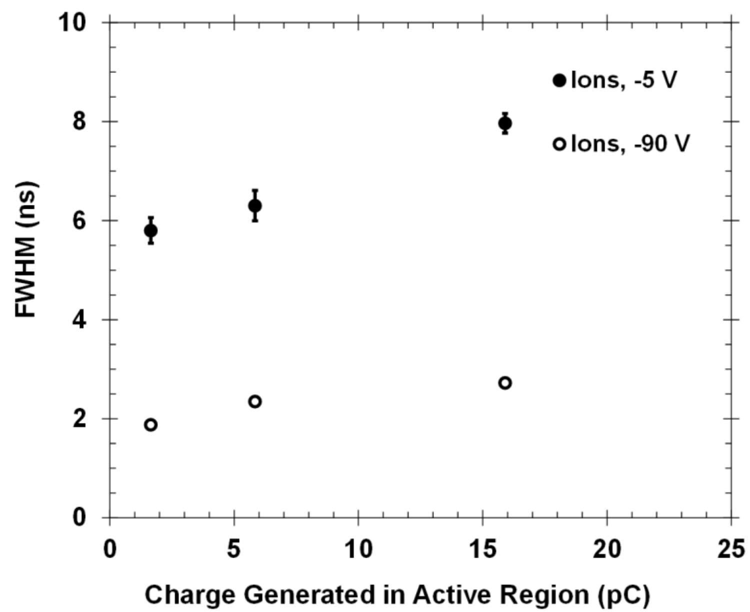

Figure V.5. Heavy ion-induced transient FWHM as a function of charge generated for -5 V (closed circles) and -90 V (open circles) bias conditions. FWHM decreases at as reverse bias increases.

TCAD simulations support the conclusion that increasing the amount of charge generated from ions increases the amount of potential modulation. Figure V.6 shows cuts of the conduction band potential (left) and electric field (right) for the -5 V simulations at two different points in time during the transient. These cuts were taken at the center of the charge injection tracks. At the time of peak charge injection, the conduction band energies show different amounts of modulation from nominal, with xenon's modulation > copper's modulation > silicon's modulation. This corresponds to the differences in electric field seen in the figures on the right, with the silicon simulations showing a stronger initial electric field, and this is consistent with the observed rise times. Silicon has the fastest rise time of the ion experiments, shows the least amount of

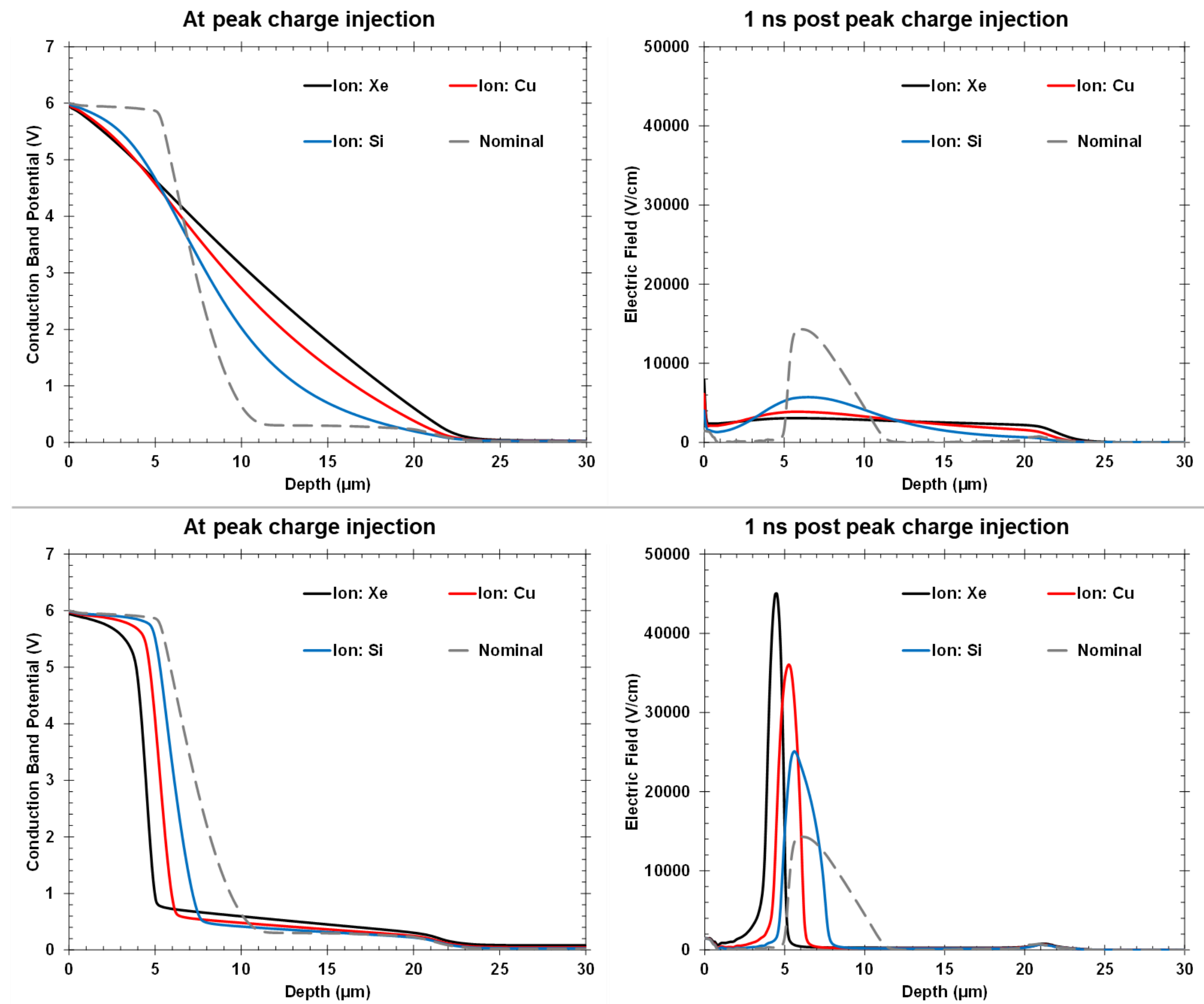

Figure V.6. Heavy ion TCAD simulation results from the -5 V bias condition. Conduction band potential (left) and electric field (right) are shown at two time steps: at peak charge injection (top) and 1 ns post peak charge injection (bottom). Nominal conditions are denoted by the dashed grey lines.

perturbation in the potential from nominal conditions, and has the largest initial electric field during the transient. As time moves forward in the simulations, silicon returns to nominal conditions more quickly than the other ions, as shown in the "Time = 1 ns" simulation results, while xenon takes the longest to return to normal. This is consistent with the observed fall times, with silicon and copper having faster fall times than xenon. All ions return to nominal conditions (not shown in figure) at some time between 10 ns and 100 ns post peak charge injection, which is expected from the experimental fall times of 20 – 40 ns.

Conduction band potential and electric field cuts are shown for the -90 V simulations in Figure V.7, and the results agree with those from the -5 V simulations and experiments. The xenon

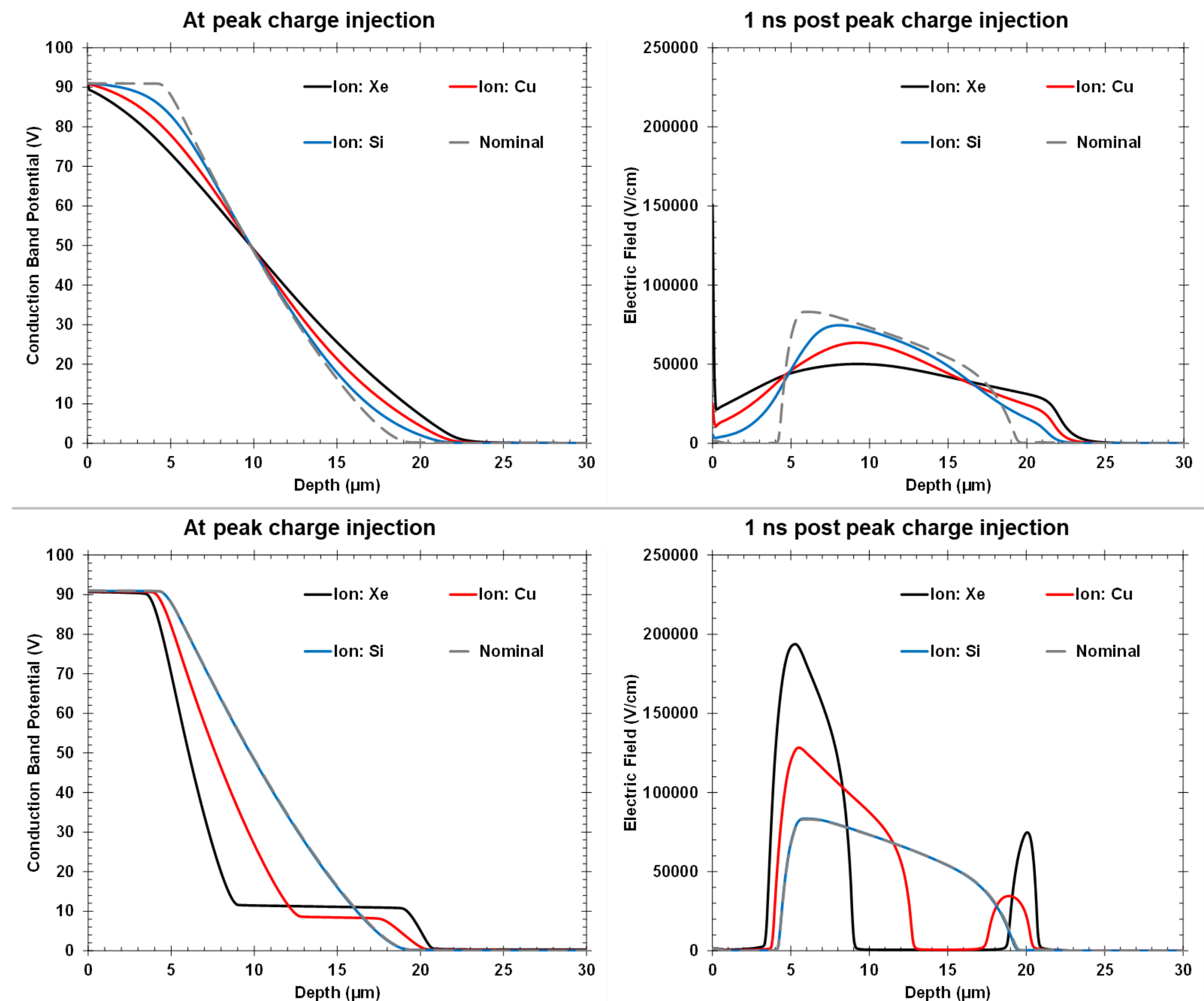

Figure V.7. Heavy ion TCAD simulation results from the -90 V bias condition. Conduction band potential (left) and electric field (right) are shown at two time steps: at peak charge injection (top) and 5 ns post peak charge injection (bottom). Nominal conditions are denoted by the dashed grey lines.

ion, which has the largest amount of generated charge for the ions, creates the most potential modulation and thus has the weakest initial electric field, and takes the longest to recover to nominal conditions. Silicon leads to the least potential modulation, has the strongest initial electric field, and recovers to nominal conditions fastest. Overall, the -90 V simulations return to nominal conditions faster than the -5 V simulations, owing to the dominance of the stronger nominal electric field at this bias condition, which is consistent with experimental observations. This is seen in the simulations with the -5 V simulations still showing modulation for as long as 10 ns after peak charge injection, while the -90 V simulations have returned to nominal by 5 ns post peak injection.

B. Pulsed Laser

The amount of pulsed laser data necessitates separating the -5 V and -90 V results into separate plots. Vertical axes are kept constant for comparisons. The data is organized by pulse energy: black circles for 400 pJ, red squares for 750 pJ, and green triangles for 990 pJ.

Figures V.8 and V.9 show the pulsed laser-induced collected charge for the -5 V and -90 V experiments, respectively, and show linear relationships with charge generated. Amount of generated charge was varied by changing the focal position and the pulse energy. All pulse energies show similar collections efficiencies within a bias condition, though -90 V focal positions that generate similar amounts of charge appear to have slightly different collection efficiencies. At -5 V, the collection efficiency is roughly 1.0, indicated by the dashed grey line, and the -90 V collection efficiency is approximately 1.2, resulting in a 20% increase. Peak current results are shown in Figures V.10 and V.11 and show linear relationships to charge generated, with peak current to charge generated ratios of 0.12 mA/pC and 0.46 mA/pC, respectively, a 283% increase. The increase in collection efficiency and peak current are due to an increase in electric field strength at the larger reverse bias condition.

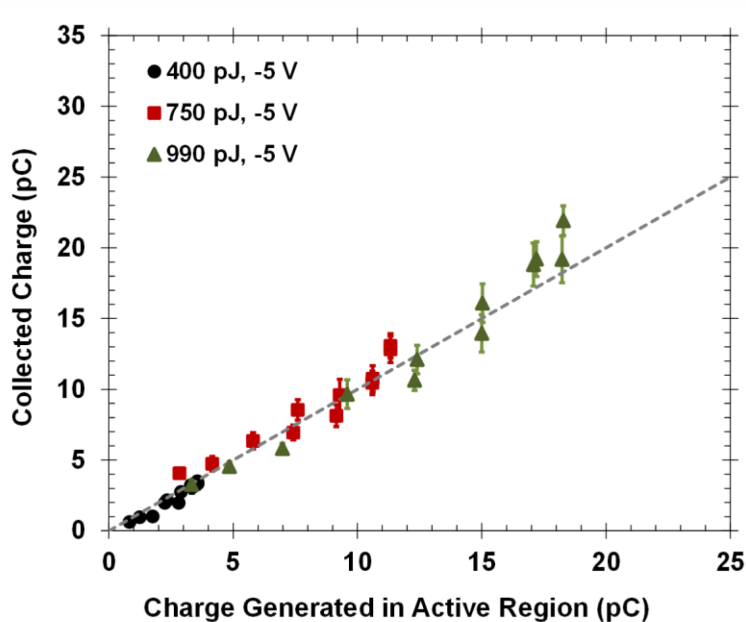

Figure V.8. Pulsed laser-induced collected charge as a function of charge generated for pulse energies 400 pJ (black circles) 750 pJ (red squares), and 990 pJ (green triangles) at -5 V. Collected charge shows a linear relationship with charge generated.

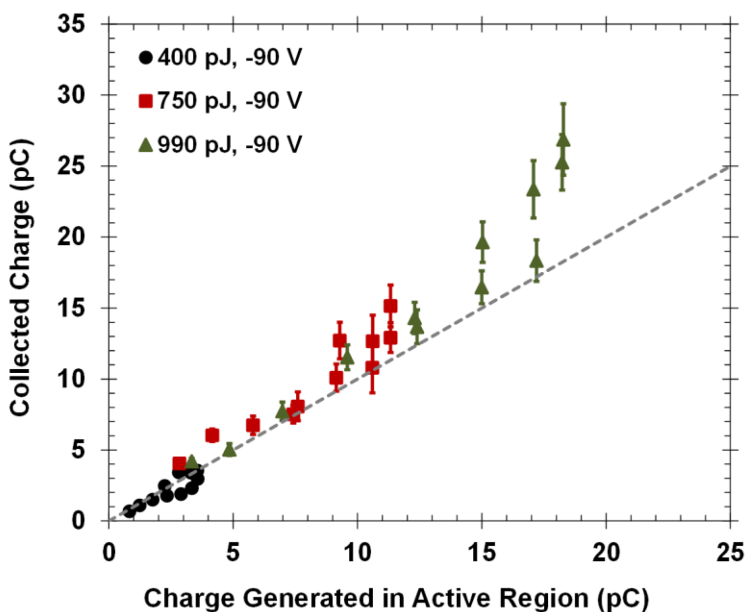

Figure V.9. Pulsed laser-induced collected charge as a function of charge generated for pulse energies 400 pJ (black circles) 750 pJ (red squares), and 990 pJ (green triangles) at -90 V. Collected charge shows a linear relationship with charge generated.

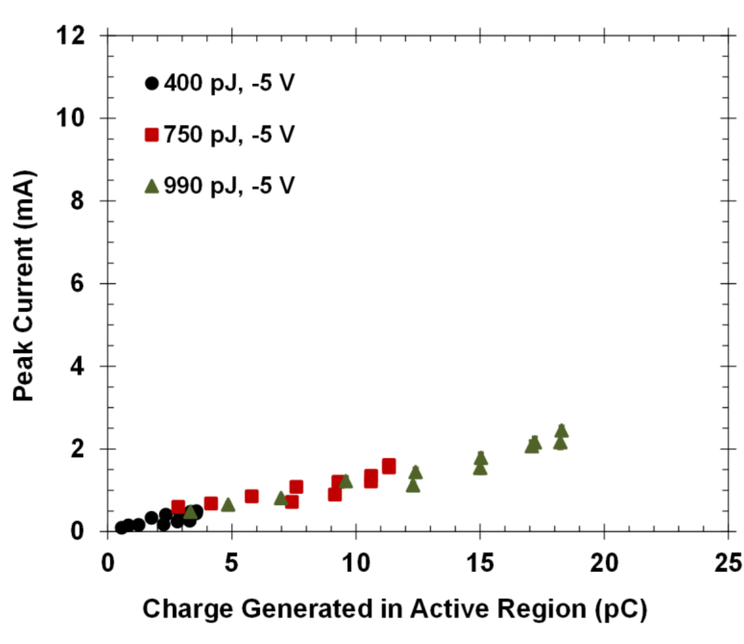

Figure V.10. Pulsed laser-induced peak current as a function of charge generated for pulse energies 400 pJ (black circles) 750 pJ (red squares), and 990 pJ (green triangles) at -5 V. Peak current shows a linear relationship with charge generated.

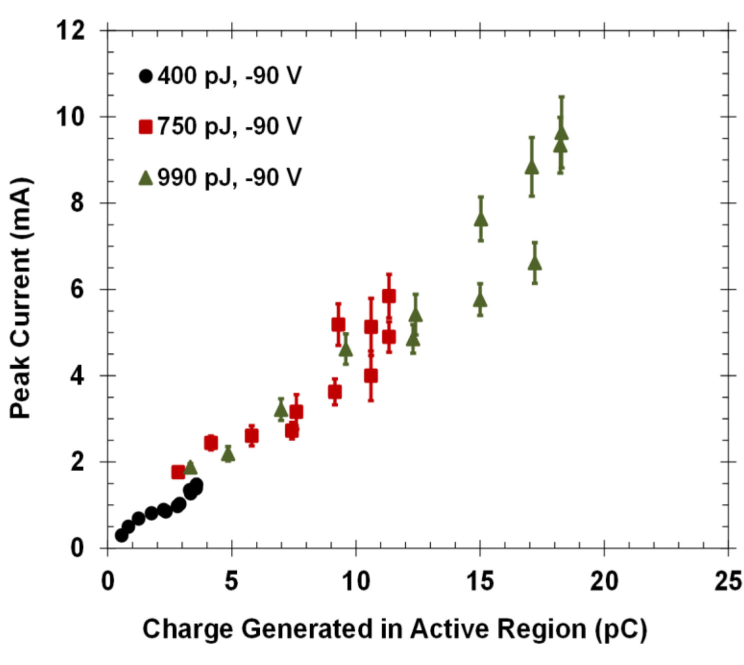

Figure V.11. Pulsed laser-induced peak current as a function of charge generated for pulse energies 400 pJ (black circles) 750 pJ (red squares), and 990 pJ (green triangles) at -90 V. Peak current shows a linear relationship with charge generated.

The transient rise times are shown in Figures V.12 and V.13 for -5 V and -90 V, respectively. The black arrow in Figure V.12 shows the direction of moving the focal position deeper into the diode; for other transient shape characteristics (peak current and collected charge), the difference between focal positions with the same generated charge is not as noticeable. At -5 V, there is a large variation in rise time based on charge generated and focal position. For the same amount of charge generated, focal positions deeper into the diode have faster rise times. Given that rise time is dominated by drift, and therefore the internal electric field, this indicates a stronger electric field is present in the experiments with deeper focal positions. There is no distinct difference in transient rise times at different focal positions in the -90 V experiments and more consistency in rise time with respect to charge generated. Both observations are consistent with the stronger internal electric field dominating the response compared to the -5 V results.

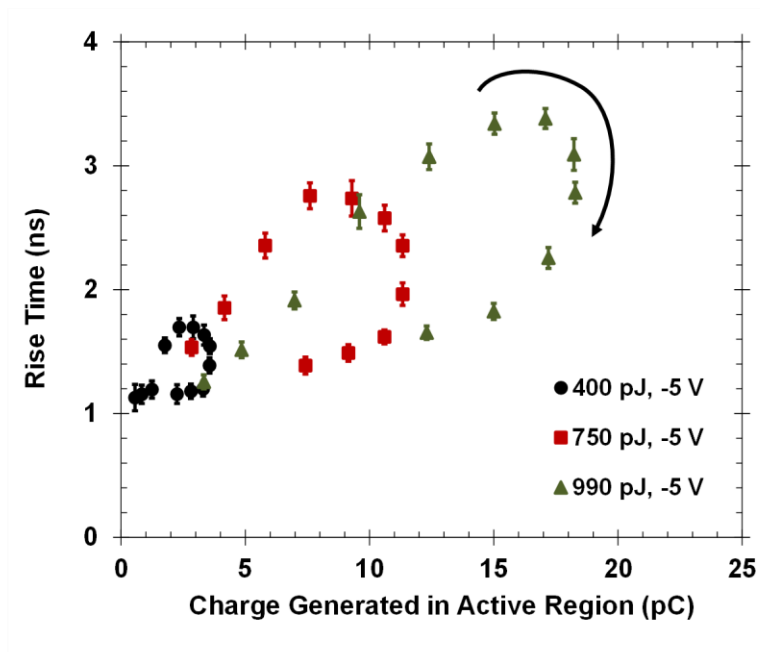

Figure V.12. Pulsed laser-induced transient rise time as a function of charge generated for pulse energies 400 pJ (black circles) 750 pJ (red squares), and 990 pJ (green triangles) at -5 V. The black arrow shows the direction of focal positions moving further into the diode.

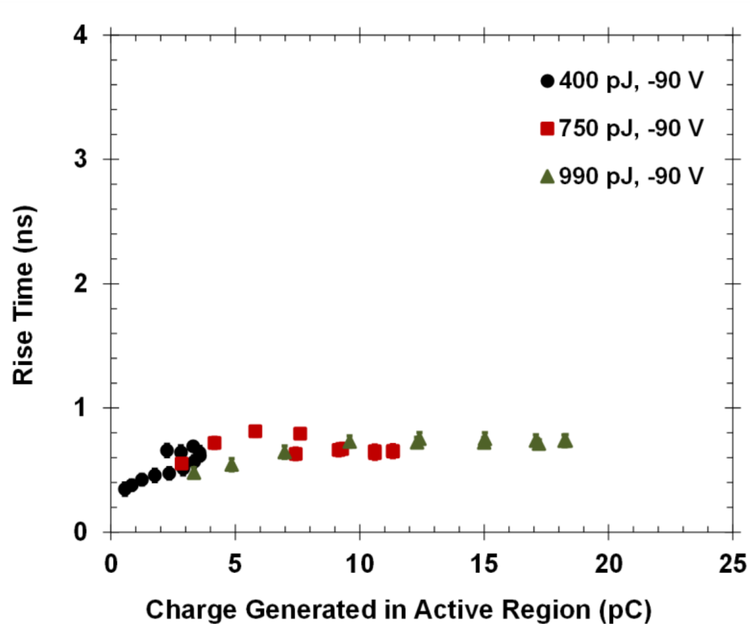

Figure V.13. Pulsed laser-induced transient rise time as a function of charge generated for pulse energies 400 pJ (black circles) 750 pJ (red squares), and 990 pJ (green triangles) at -90 V. Rise time is consistent as a function of charge generated and focal position.

Pulsed laser-induced transient fall time is shown in Figures V.14 and V.15. Like the rise times, the -5 V fall times show a dependence on both charge generated and focal position, with focal positions deeper into the diode having longer fall times, while the -90 V fall times are consistent with charge generated and focal position. This further highlights the dominance of the internal electric field at -90 V. An interesting observation is that the focal positions that result in faster rise times at -5 V, result in slower fall times. This has an interesting effect on the transient FWHM values at -5 V, shown in Figure V.16, in that there is much less variation with respect to focal position. FWHM does increase with increased charge generated, which is consistent with the rise and fall time trends. The -90 V transient FWHMs are shown in Figure V.17 and display the same trends observed in the -90 V rise and fall times: consistent times across both charge generated and focal position. Taken together, the -5 V pulsed laser-induced timing characteristics demonstrate how different charge profiles interact with the internal electric field differently. The -90 V timing characteristics demonstrate how a strong internal electric field can dominate the device response when potential modulation is limited.

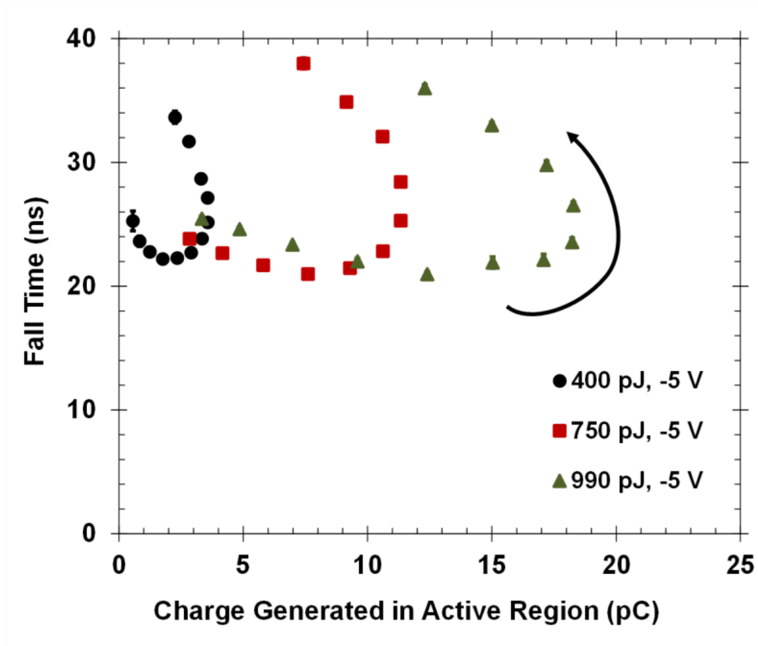

Figure V.14. Pulsed laser-induced transient fall time as a function of charge generated for pulse energies 400 pJ (black circles) 750 pJ (red squares), and 990 pJ (green triangles) at -5 V. The black arrow shows the direction of focal positions moving further into the diode.

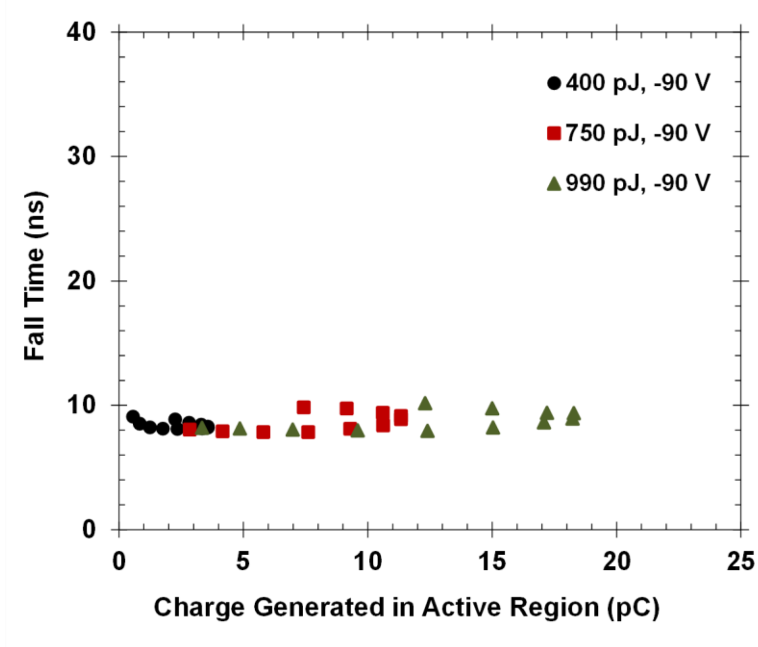

Figure V.15. Pulsed laser-induced transient fall time as a function of charge generated for pulse energies 400 pJ (black circles) 750 pJ (red squares), and 990 pJ (green triangles) at -90 V. Fall time is consistent as a function of charge generated and focal position.

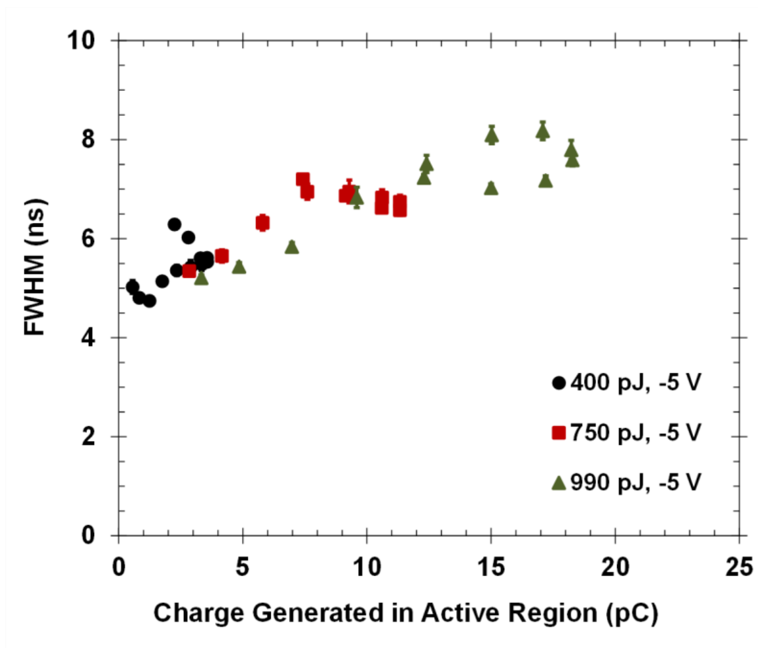

Figure V.16. Pulsed laser-induced transient FWHM as a function of charge generated for pulse energies 400 pJ (black circles) 750 pJ (red squares), and 990 pJ (green triangles) at -90 V. FWHM increases with increased charge generated and shows a slight dependence on focal position.

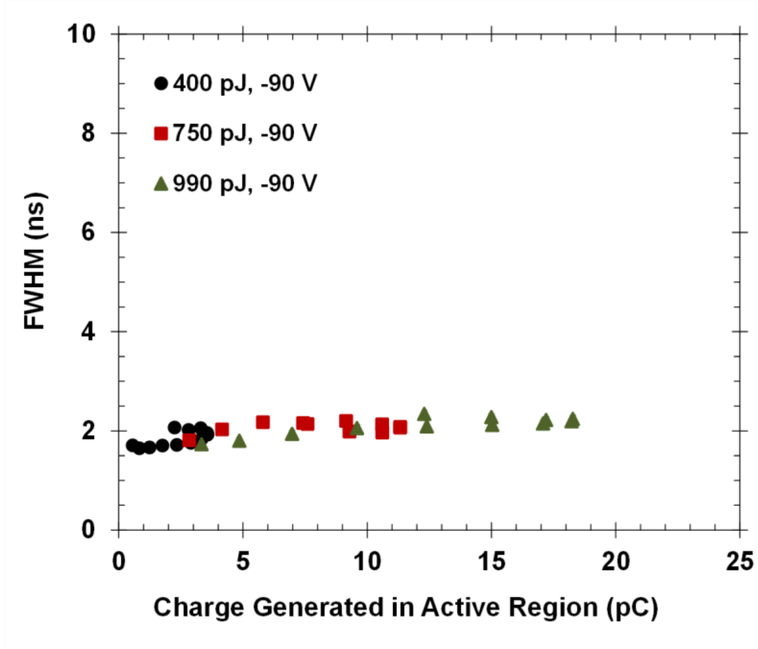

Figure V.17. Pulsed laser-induced transient FWHM as a function of charge generated for pulse energies 400 pJ (black circles) 750 pJ (red squares), and 990 pJ (green triangles) at -90 V. FWHM is consistent as a function of charge generated and focal position.

Examining the pulsed laser TCAD simulations provides insight into the differences between the focal positions. Figures V.18 and V.19 show the conduction band potential and electric field cuts from -5 V and -90 V pulsed laser simulations at two different time points during the transients. Three laser conditions are shown to highlight how focal position and amount of charge generated affect device response: 990 pJ at 3.5 μm, 750 pJ at 3.5 μm, and 990 pJ at 21 μm. The two 990 pJ laser conditions generate similar amounts of charge in the diode's active region (~15 pC), while the two 3.5 μm focal position conditions generate different amounts of charge in the same region (9 pC for the 750 pJ condition).

From the experimental results, it is seen that different focal positions with similar generated charges result in different rise and fall times. From the TCAD simulations (the blue and black curves), these focal positions result in differences in potential modulation, with the 3.5 μm focal position pushing the electric field further into the silicon and the 21 μm focal position pushing the electric field closer to the device contact. At -5 V, the differences between the two curves are most prominent 1 ns post peak injection, after the charge has had time to diffuse outward from its initial location. At -90 V, on the other hand, the differences between the two focal positions are most notable at the time of peak charge injection, before the nominal electric field can redistribute.

Comparing the two 3.5 μm focal positions conditions (the blue and red curves) shows similar amounts of potential modulation and a similar time profile of potential modulation, which agrees with the experimental data. Both conditions push the electric field further into the device, closer to the substrate. The three laser conditions show the most similarities at -90 V, which is consistent with the experimental data and demonstrates the dominant role the strong nominal electric field plays in the device response. Overall, the pulsed laser experimental data and TCAD simulations demonstrate that focal position plays a larger role in device response than amount of generated charge in determining device response from pulsed laser-induced SEEs.

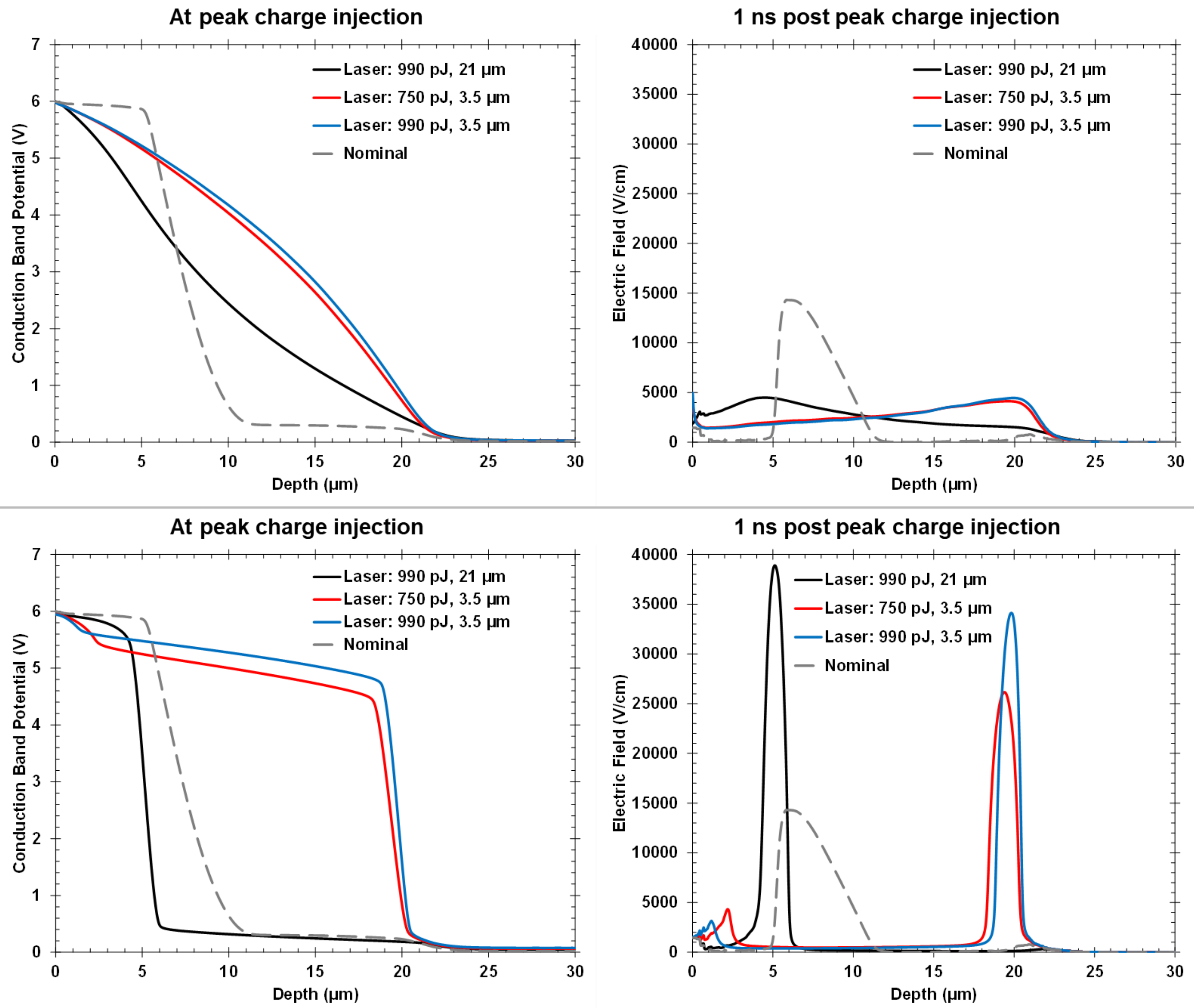

Figure V.18. Pulsed laser TCAD simulation results from the -5 V bias condition. Conduction band potential (left) and electric field (right) are shown at two time steps: at peak charge injection (top) and 1 ns post peak charge injection (bottom). Nominal conditions are denoted by the dashed grey lines.

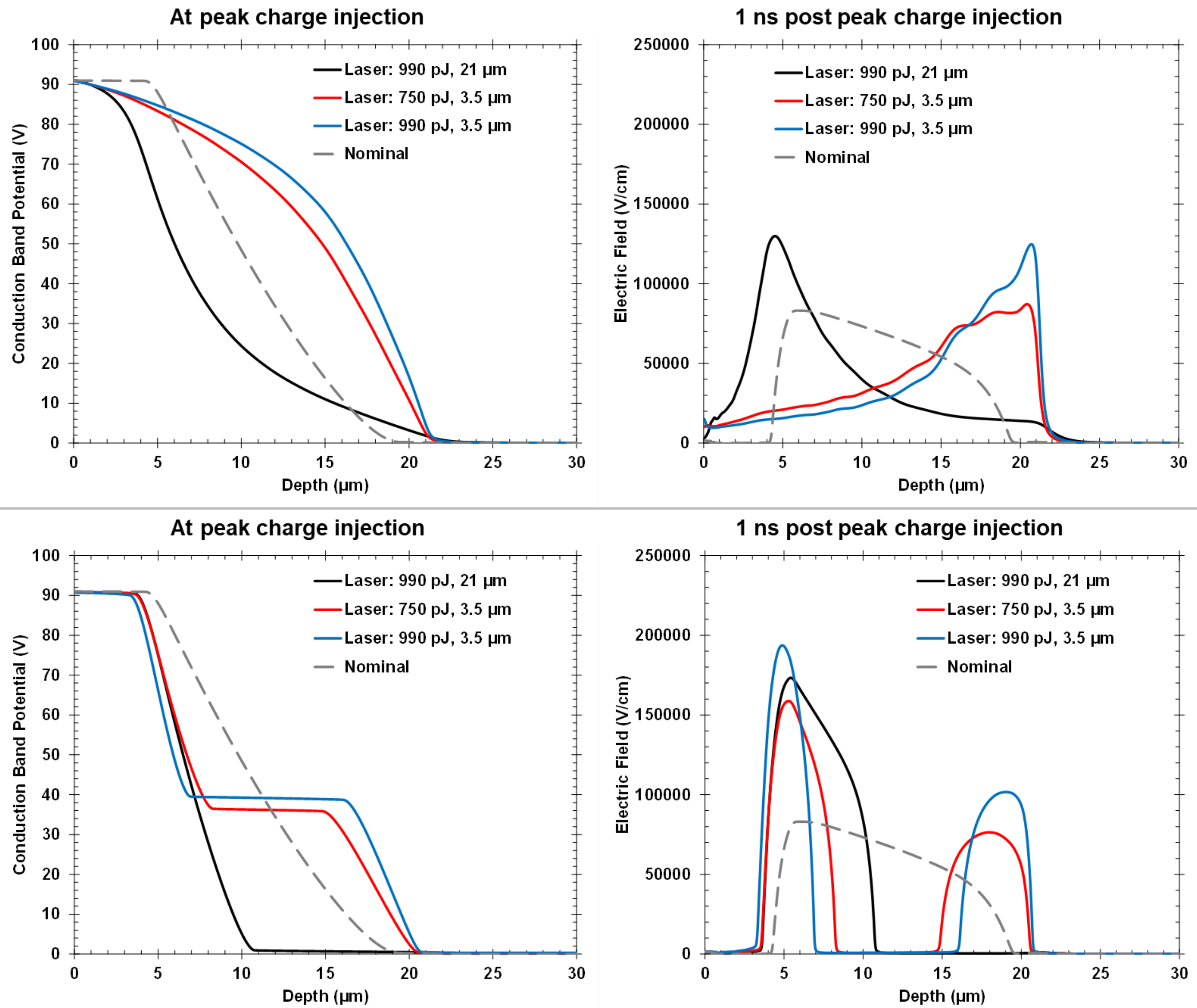

Figure V.19. Pulsed laser TCAD simulation results from the -90 V bias condition. Conduction band potential (left) and electric field (right) are shown at two time steps: at peak charge injection (top) and 1 ns post peak charge injection (bottom). Nominal conditions are denoted by the dashed grey lines.

C. Focused X-Ray

Focused X-ray-induced collected charge is shown in Figure V.20 and peak current in Figure V.21. Focused X-ray data is organized by both photon energy and bias condition. Different photon energies are denoted by different colors and shapes: black circles for 8 keV, red squares for 10 keV, and green triangles for 12 keV photons. Bias conditions are denoted by open or closed shapes, with -5 V results being closed shapes and -90 V results being open shapes.

As with the other radiation sources, both collected charge and peak current show linear relationships with charge generated and increase with increased reverse bias. There is no

discernable dependence on photon energy. The collection efficiency increases from 0.62 at -5 V to 0.77 at -90 V, a 24% increase. It is interesting to note that the collection efficiency never reaches 1.0, as it did for the other radiation sources; this will be discussed further in ***Chapter VI***. Overall, there is not much change in collected charge as bias condition increases. Peak current does show significant increase with increased reverse bias, with the peak current to charge generated ratio increasing from 0.07 mA/pC at -5 V to 0.29 mA/pC at -90 V, a 314% increase.

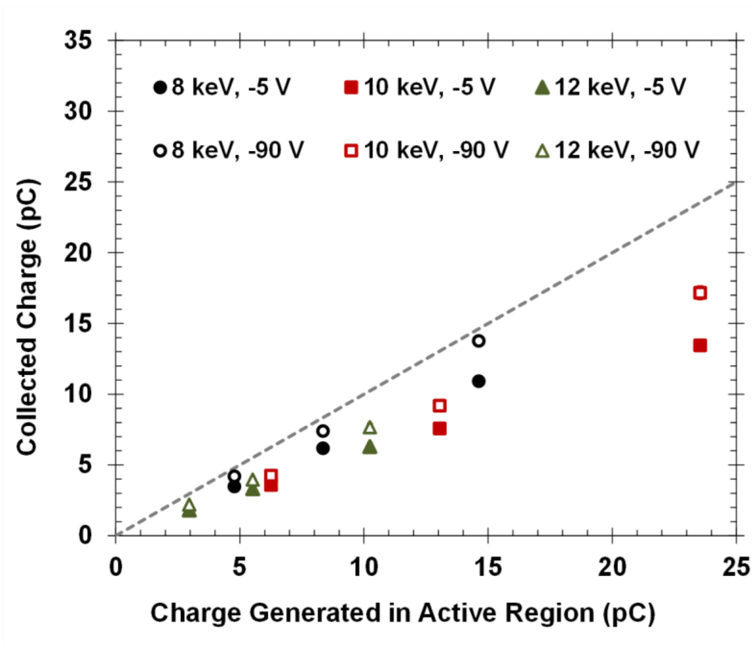

Figure V.20. Focused X-ray-induced collected charge as a function of charge generated for 8 keV (black circles), 10 keV (red squares), and 12 keV (green triangles) photon energies. Closed shapes show -5 V data, while open shapes show -90 V. Collected charge shows a linear relationship with charge generated.

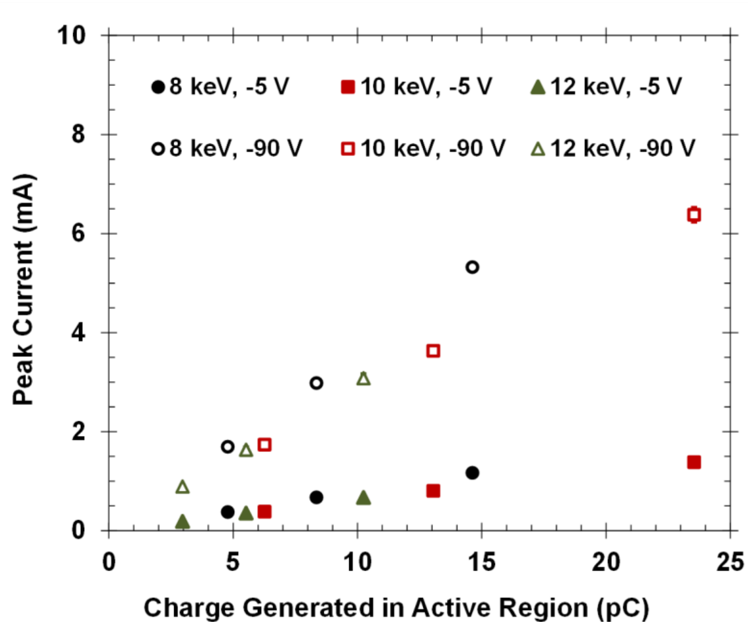

Figure V.21. Focused X-ray-induced peak current as a function of charge generated for 8 keV (black circles), 10 keV (red squares), and 12 keV (green triangles) photon energies. Closed shapes show -5 V data, while open shapes show -90 V. Peak current shows a linear relationship with charge generated.

Transient rise time, fall time, and FWHM for the focused X-ray experiments are shown in Figures V.22 – V.24, respectively. All three timing characteristics share similar trends with respect to both charge generated and bias condition; there is no discernable dependence on photon energy. In general, the transient rise time, fall time, and FWHM are constant with respect to charge generated and photon energy, and decrease with increased reverse bias. The decrease in timing characteristics with increased reverse bias is expected due to the stronger internal electric field, while the consistency across charge generated suggests that the X-ray-induced timing characteristics are dominated by the diode’s nominal electric field. The lack of perturbations to the internal electric field is consistent with the small change in collection efficiency, which is indicative of less potential modulation.

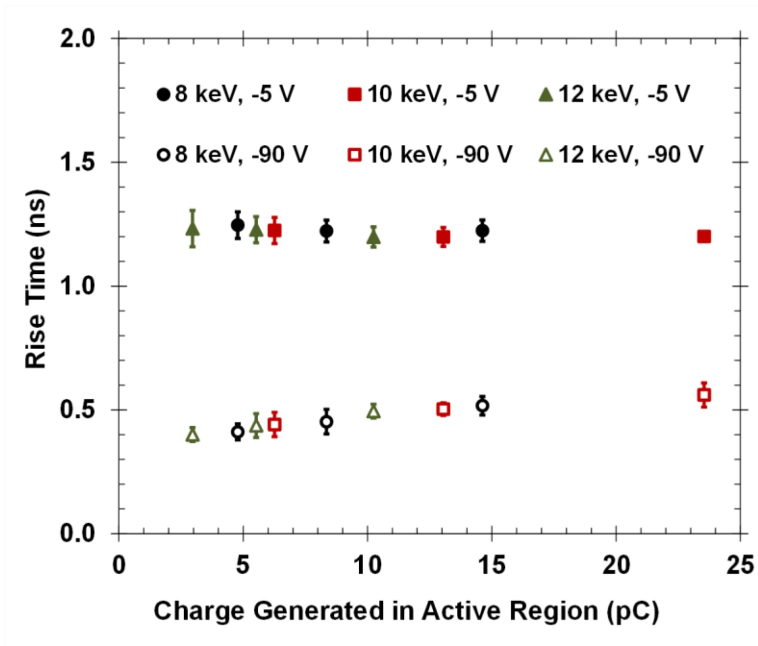

Figure V.22. Focused X-ray-induced transient rise time as a function of charge generated for 8 keV (black circles), 10 keV (red squares), and 12 keV (green triangles) photon energies. Closed shapes show -5 V data, while open shapes show -90 V. Rise time is constant with respect to charge generated.

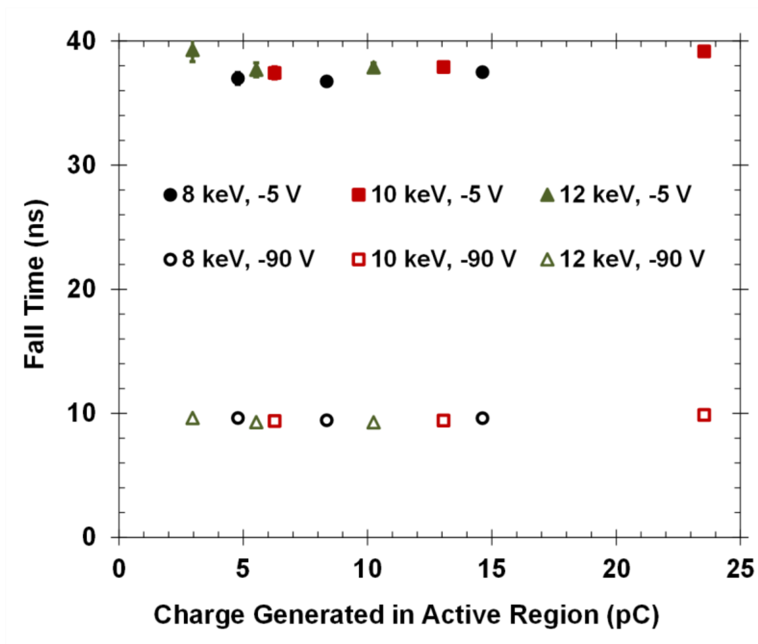

Figure V.23. Focused X-ray-induced transient fall time as a function of charge generated for 8 keV (black circles), 10 keV (red squares), and 12 keV (green triangles) photon energies. Closed shapes show -5 V data, while open shapes show -90 V. Fall time is constant with respect to charge generated.

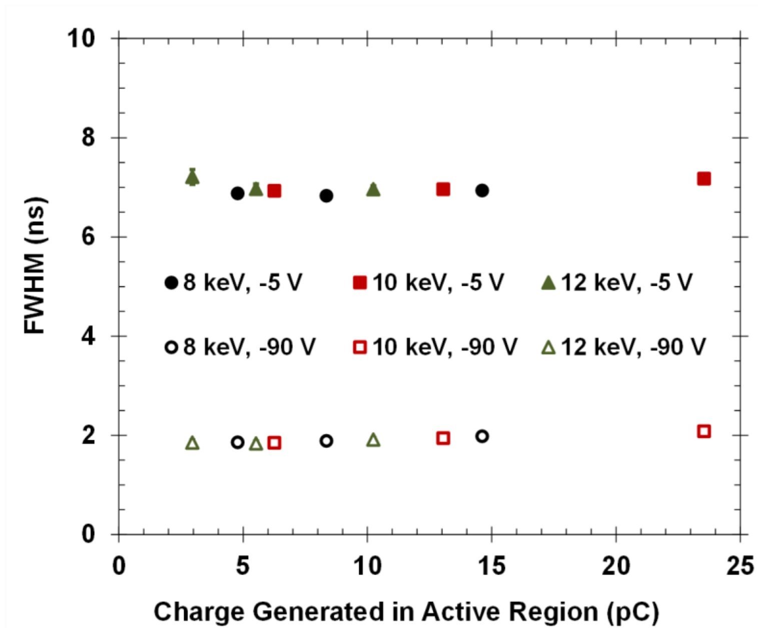

Figure V.24. Focused X-ray-induced transient FWHM as a function of charge generated for 8 keV (black circles), 10 keV (red squares), and 12 keV (green triangles) photon energies. Closed shapes show -5 V data, while open shapes show -90 V. FWHM is constant with respect to charge generated.

As with the other radiation sources, analyzing the band diagrams and electric fields within TCAD supports the experimental observations. Figures V.25 and V.26 show the conduction band energy (left) and electric field (right) at -5 V and -90 V, respectively, for three X-ray pulses at different times during the simulations. The X-ray photon energies and fluxes chosen to be shown encompass the X-ray conditions with the most amount of generated charge (10 keV full flux, 24 pC), the least amount of charge generated (12 keV ¼ flux, 3 pC), and an amount in between (8 keV ½ flux, 8 pC). Despite the wide range in amounts of charge generated in the diode's active region, the three X-ray conditions result in very similar amounts of potential modulation at the time of peak injection at -5 V (top of Figure V.25). This uniformity in potential modulation, demonstrated by both the conduction band potential and the electric field at "Time = 0 s", is consistent with the experimental rise time, which show little to no variation with charge generated. By 1 ns post peak charge injection (bottom of Figure V.25), the differences in potential modulation amongst the different X-ray pulses are still minimal, resulting in the fall time's observed lack of dependence on charge generated.

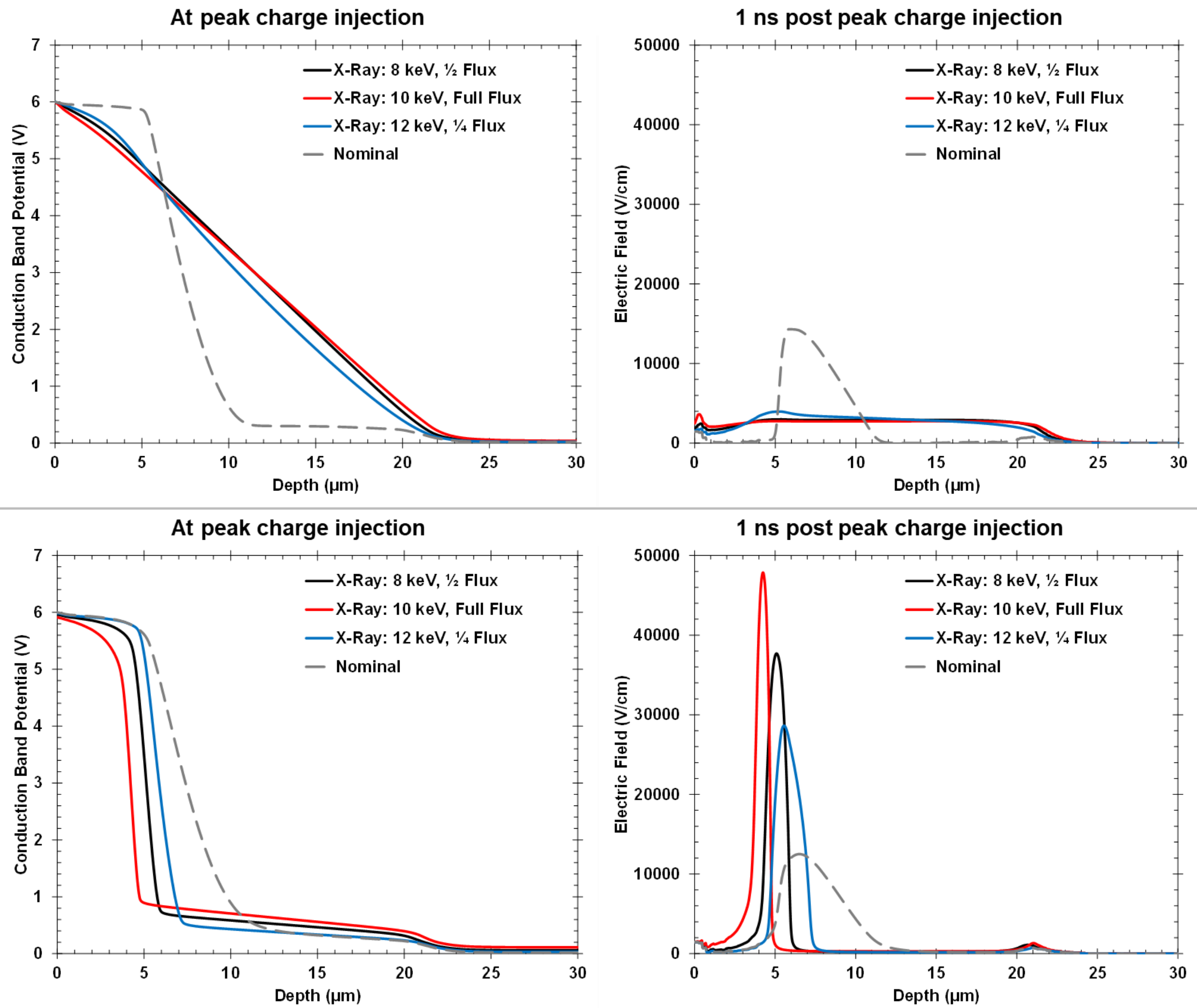

Figure V.25. Focused X-ray TCAD simulation results from the -5 V bias condition. Conduction band potential (left) and electric field (right) are shown at two time steps: at peak charge injection (top) and 1 ns post peak charge injection (bottom). Nominal conditions are denoted by the dashed grey lines.

At -90 V (Figure V.26), there is more deviation in the amount of potential modulation from each of the X-ray pulses, both at the time of peak charge injection and 1 ns post peak injection. The 10 keV full flux X-ray pulse, which has the largest amount of generated charge, results in the most modulation, while the 12 keV ¼ flux pulse results in the least amount of modulation. This results in the observed trends in both rise and fall time, where there is a slight change in both with respect to charge generated. As was observed with the other radiation sources, the potential modulation collapses back to nominal conditions faster at -90 V than at -5 V, which is expected.

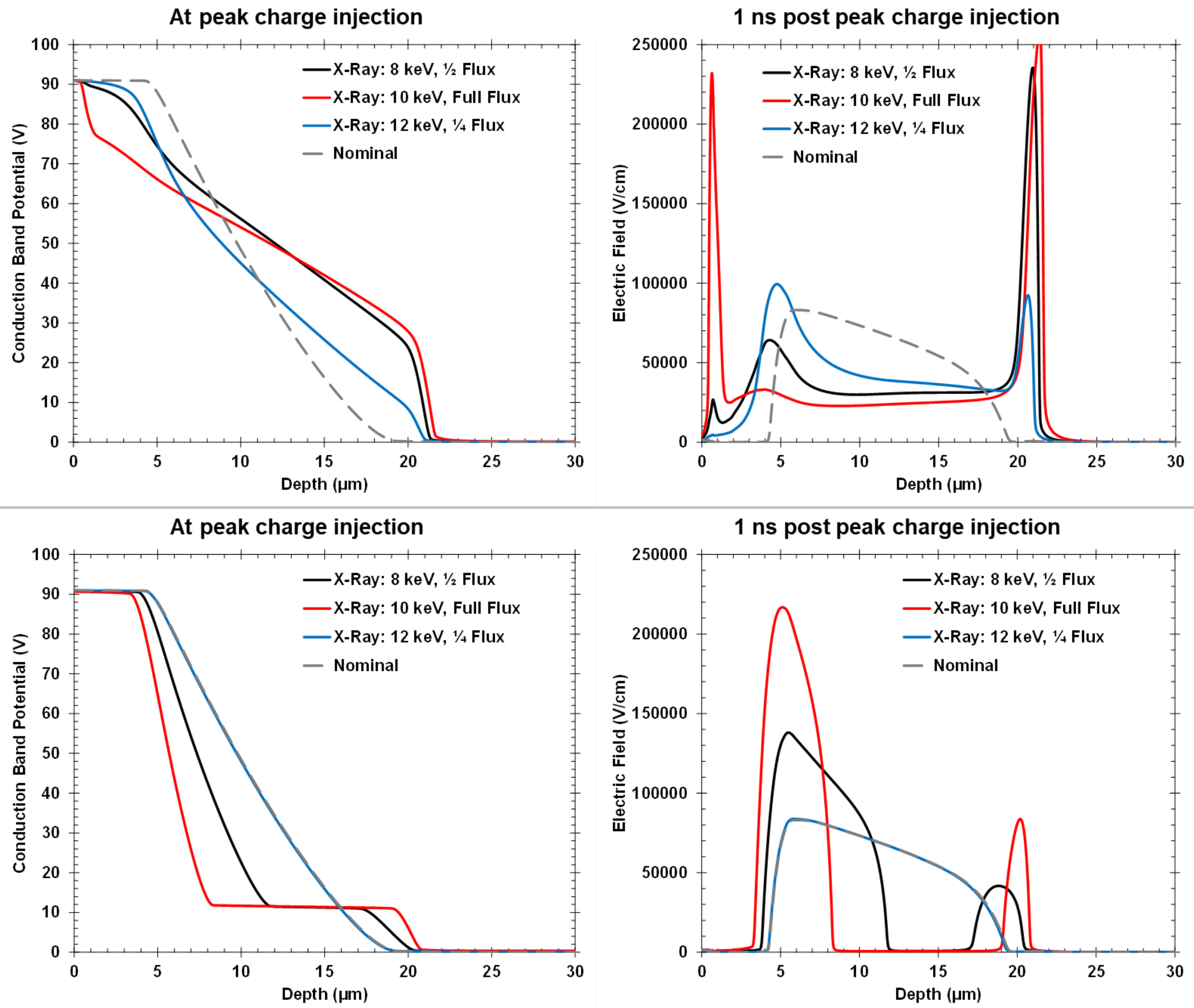

Figure V.26. Focused X-ray TCAD simulation results from the -90 V bias condition. Conduction band potential (left) and electric field (right) are shown at two time steps: at peak charge injection (top) and 1 ns post peak charge injection (bottom). Nominal conditions are denoted by the dashed grey lines.

CHAPTER VI

COMPARISON OF RESULTS FROM DIFFERENT RADIATION SOURCES

Experimental results from each of the radiation sources is presented in ***Chapter V – Experimental Results from each Radiation Source***. Here, results from the radiation sources are compared to each other and differences are highlighted. Sentaurus TCAD simulation results are used to support the experimental observations and provide insight into mechanisms. Heavy ion- and pulsed laser-induced sensitive volumes were originally compared in [60]; an update is presented here to include the X-ray-induced sensitive volumes. SETs produced with similar amounts of generated charge from each radiation source are examined, and overall trends in SET shape characteristics as functions of generated charge and bias are investigated. Finally, TCAD simulations are used to investigate the primary mechanisms behind the observed differences.

Adapted with permission from K. L. Ryder *et al.*, "Comparison of Sensitive Volumes Associated with Ion- and Laser-Induced Charge Collection in an Epitaxial Silicon Diode," *IEEE Trans. Nucl. Sci.*, vol. 67, no. 1, pp. 57-62, Jan. 2020 and K. L. Ryder *et al.*, "Comparison of Single Event Transients in an Epitaxial Silicon Diode Resulting from Heavy Ion-, Focused X-Ray-, and Pulsed Laser-Induced Charge Generation," *IEEE Trans. Nucl. Sci.*, vol. 68, no. 5, pp. 626-633, May 2021.

A. Comparison of Sensitive Volumes

Sensitive volumes have been used since 1978 by the radiation effects community as a method of relating energy deposition from ions to circuit responses in space radiation environments [115]. Typically, sensitive volumes are used to relate collected charge, single event upset cross sections, and other single event effects to energy deposited and charge generated by ions. Multiple sensitive volume models have been developed over time with varying levels of complexity, from the most basic rectangular parallelepiped (RPP) [115, 116] to elaborate multi-region geometries [117, 118]. The most prominent use of sensitive volumes is as inputs to error rate calculations, using simulators such as MRED [117, 118] and CRÈME96 [119, 120]. Sensitive volumes are representative of the

time-integrated device response and examining them gives insight into the overall response from a radiation source.

A collected charge sensitive volume is defined in this work as the volume necessary to produce the experimentally observed collected charge, and a simple rectangular parallelepiped is used for the sensitive volume geometry due to the radial symmetry of the diode. The entire surface area of the diode is equally sensitive to radiation, so the only unknown dimension is the lateral extent, called the sensitive volume depth (SD_x). If both the experimental collected charge and charge generation profiles are known, the sensitive volume depth can be found by modifying the charge generation equations from ***Chapter III***, shown as Equations VI.1 – VI.3 below. Solving for SD_x gives the sensitive volume depth for each of the radiation sources.

$$Q_{collected,ion} = \frac{q\rho}{E_{ehp}} \int_{SD_{ion}} LET(x)dx \qquad (VI.1)$$

$$Q_{collected,laser} = \int_{SD_{laser}} \frac{dQ_{gen,laser}}{dx} dx \qquad (VI.2)$$

$$Q_{collected,X-ray} = \frac{E_p}{E_{ehp}} \cdot (1 - e^{-\alpha SD_{X-ray}}) \qquad (VI.3)$$

For each experimental condition, the sensitive volume depth was calculated using the appropriate collected charge (***Chapter V***) and charge generation profile (***Chapter IV***); the average for each radiation source was computed. The funnel length [107, 108] for each sensitive volume depth was found by subtracting the depletion depth for that bias condition from the sensitive volume depth. Depletion depth is the depth of the bottom of the depletion region, 11.5 µm for -5 V and 20.7 µm for -90 V. Table VI.1 summarizes the sensitive volume depths and funnel lengths for each of the radiation sources and bias conditions. Figure VI.1 shows the sensitive volumes with the nominal depletion region represented by the translucent grey box. The heavy ion sensitive volumes shown in black, pulsed laser shown in blue, and the focused X-ray in red. Only the depths of the sensitive volumes are to scale with the diode structure (dimensions are shown to the right), because the sensitive volume area encompasses the whole device area for all radiation sources.

The heavy ion-induced sensitive volume increased by 67% with increased reverse bias, while its funnel length only increased by 23%. Pulsed laser- and focused X-ray-induced sensitive volumes show less of an increase with bias, 13% and 19%, respectively, and their funnel lengths decrease by 54% and 138%, respectively.

Table VI.1. Summary of sensitive volume depths and funnel lengths

Radiation Source	-5 V SD (μm)	-5 V Funnel Length (μm)	-90 V SD (μm)	-90 V Funnel Length (μm)
Heavy Ions	15	3.5	25	4.3
Pulsed Laser	23	11.5	26	5.3
Focused X-rays	16	4.5	19	-1.7

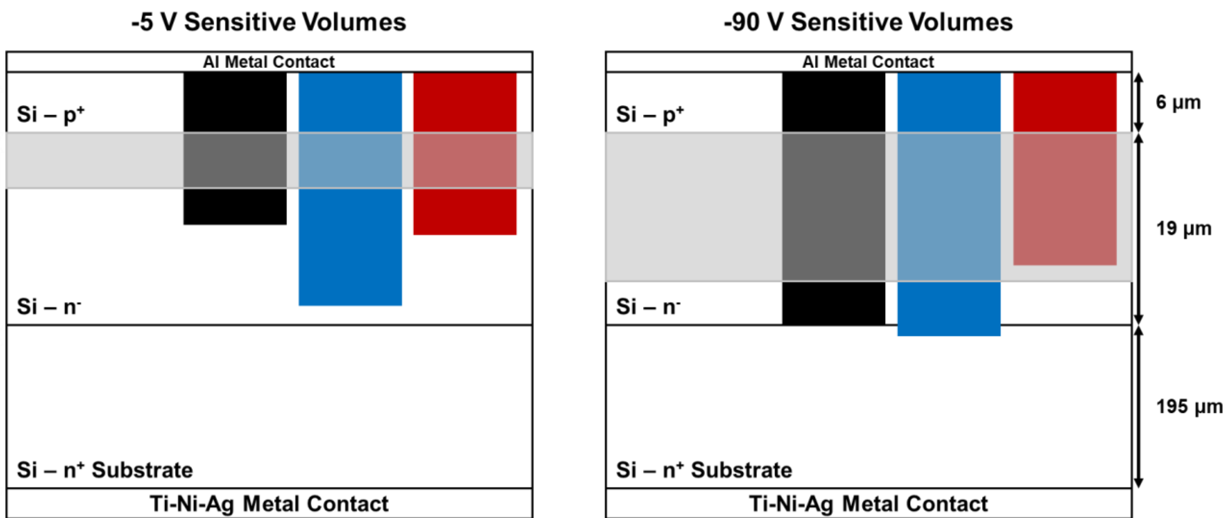

Figure VI.1. Sensitive volumes for the -5 V (left) and -90 V (right) experiments. Heavy ion volumes are shown in black, pulsed laser volumes in blue, and focused X-ray volumes in red. The translucent grey boxes show the nominal depletion region at that bias condition.

The heavy ion-induced sensitive volumes and funnel lengths display a bias dependence that is absent from the other radiation sources and demonstrates a dependence on the nominal internal electric field. On the other hand, the pulsed laser-induced sensitive volumes appear to be nearly independent of bias condition. This could be due to truncation of potential modulation by the heavily doped substrate at the higher reverse bias. The focused X-ray-induced sensitive volumes

also show less change with respect to bias than the heavy ions but fail to fully deplete the epitaxial layer like the pulsed laser. The nominal depletion region appears to drive the focused X-ray-induced sensitive volumes, while the other radiation sources are less dependent on nominal operating conditions. In short, the time-averaged device response from the different radiation sources differs, with the focused X-ray perturbing the nominal electrostatics the least and the pulsed laser perturbing it the most.

The concepts of *funnel length* and *potential modulation* are intricately tied, particularly in discussions involving sensitive volumes. Because sensitive volumes represent the time-integrated device response from SEEs, *funnel length* inherently refers to a time-integrate abstraction of changes in the electric field throughout a transient event. *Potential modulation*, as it pertains to *funnel length*, is conventionally thought of as the change in the width of the depletion modulation. However, as was seen in the TCAD simulations in ***Chapter V*** and will be seen later in this chapter, *potential modulation* can also refer to perturbations of the internal potential and electric field from the nominal conditions at a given point in time. For the other comparisons in this chapter, the latter definition of *potential modulation* is used.

B. Comparison of SETs at Comparable Charge Generated Values

Across all experimental conditions, there were several that resulted in equivalent amounts of generated charge in the diode's active region. Comparing the transients that result from the different radiation sources with similar amounts of generated charge provides insight into the temporal differences of the radiation sources. There were three experimental conditions that resulted in approximately 6 pC of charge generated in the active region and three that resulted in 15 pC of generated charge, one from each radiation source.

Three SEE experimental conditions resulted in roughly 6 pC of generated charge in the diode's active region: the copper heavy ion, the 750 pJ pulsed laser at a focal position of -1 µm outside the silicon, and the 12 keV ½ flux focused X-ray. Averaged SETs from the -5 V experiments are shown in Figure VI.2, Table VI.2 provides the numerical data associated with the SETs. The ion- and X-ray-induced SETs are more similar to each other than the pulsed laser-induced SET at -5 V, with the pulsed laser-induced SET being nearly twice as large (by both peak current and collected charge) than SETs from the other radiation sources. Fall times are the most notable timing

characteristic difference, with the X-ray SET having a much longer fall time than the other transients.

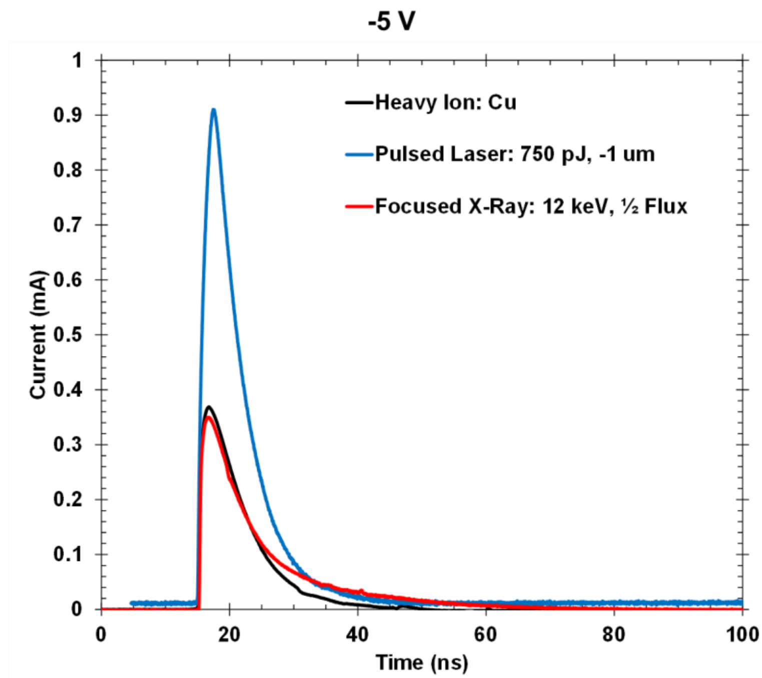

Figure VI.2. Averaged transients from the copper heavy ion (black), 750 pJ pulsed laser at a focal position of -1 µm (blue), and 12 keV, ½ flux focused X-ray (red) at a reverse bias of 5 V. Each of these radiation sources generated approximately 5.8 pC of charge in the diode's active region.

Table VI.2. Summary of -5 V SETs resulting from ~5.8 pC of generated charge

SEE Source	Ion: Cu	Laser: 750 pJ, -1 µm	X-ray: 12 keV, ½ Flux
Generated Charge (pC)	5.8	5.8	5.5
Peak Current (mA)	0.4	0.9	0.4
Collected Charge (pC)	3.1	6.4	3.3
Rise Time (ns)	1.8	2.4	1.2
Fall Time (ns)	28.3	21.7	37.7
FWHM (ns)	6.3	6.3	7.0

Comparing the potential modulation from the TCAD simulations provides insights into these differences. Figure VI.3 provides the conduction band potential and electric field cuts for these simulations at two different points in time during the transients. The differences between the radiation sources are clearest at 1 ns post peak charge injection, after the injected charge has had time to begin diffusing outward from its initial location. Both the ion and X-ray SEEs push the electric field closer to the device contact, while the laser SEE pushes the electric field further into the silicon near the substrate. The electric field in the laser simulation is also weaker and more spread out than the other simulations. These differences are consistent with the observed

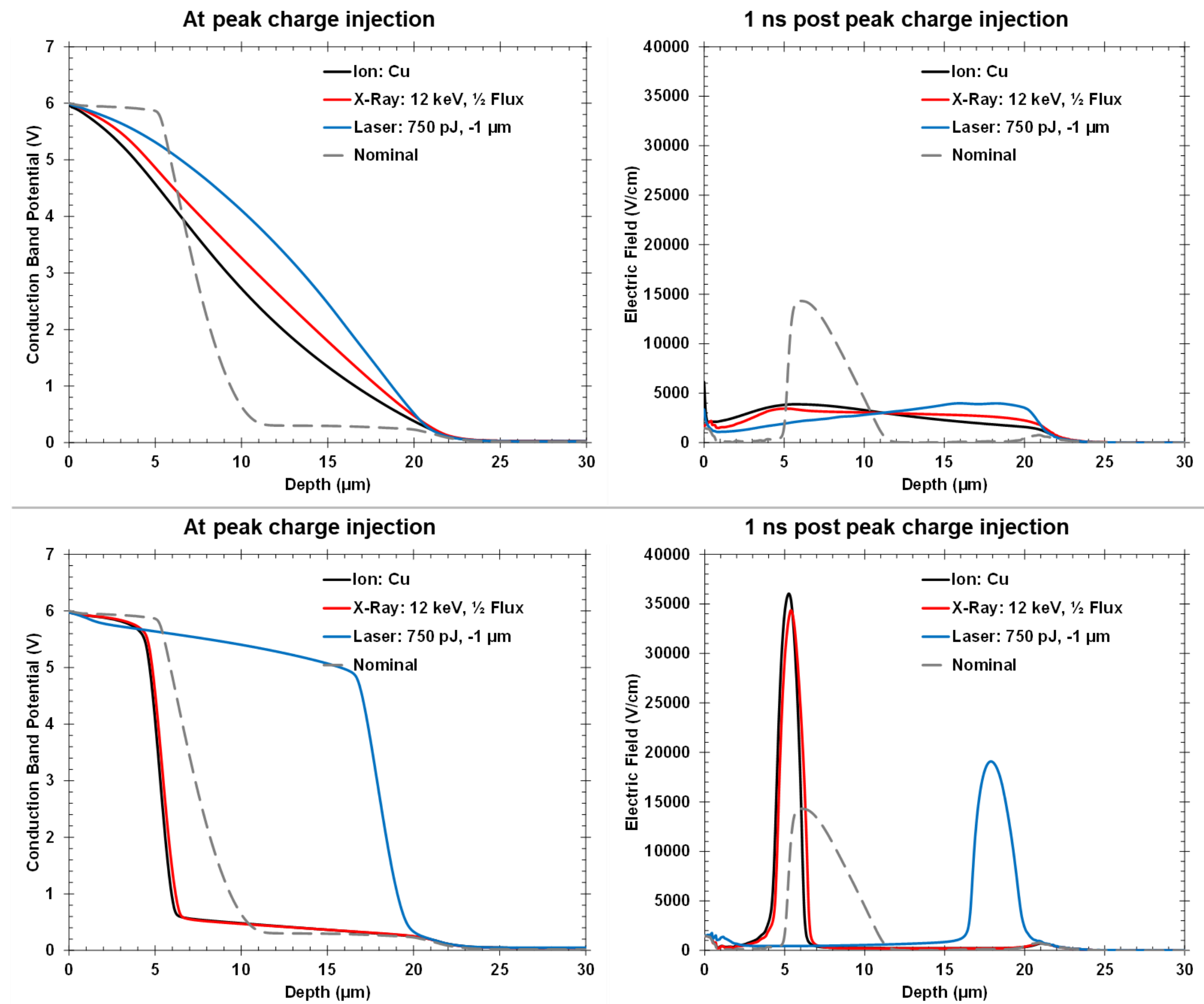

Figure VI.3. Copper heavy ion (black), 12 keV ½ flux focused X-ray (red), and 750 pJ -1 µm pulsed laser (blue) TCAD simulation results from the -5 V bias condition. Conduction band potential (left) and electric field (right) are shown at two time steps: at peak charge injection (top) and 1 ns post peak charge injection (bottom). Nominal conditions are denoted by the dashed grey lines.

differences in the experimental results. The weaker electric field over a larger area from the laser SEE results in more charge being collected through drift, albeit a slower drift, than the other radiation sources. Discrepancies in location of injected charge causes the variations in electric field region locations; both the heavy ion and focused X-ray inject charge deep into the diode's substrate, while the pulsed laser's injected charge is confined to the active region of the diode. Overall, the TCAD simulations support the conclusions drawn from experimental data.

Similarly, SETs from the -90 V experiments were compared and the averaged SETs from the Cu ion, 12 keV ½ flux focused X-ray, and 750 pJ pulsed laser at a focal position of -1 µm are shown in Figure VI.4 for this bias condition. Table VI.3 provides the numerical data associated with the SETs. Differences are observed in these SETs, as they were for the -5 V bias condition, with the laser-induced SET now being more similar to the ion-induced SET and the X-ray-induced SET being smaller. On the whole, however, these SETs are all more consistent with each other due to how the stronger nominal electric field dominates the device response. This is evident from the TCAD simulated potentials and electric fields, shown in Figure VI.5, which are far more similar in terms of electric field strength and electric field region than the -5 V simulations.

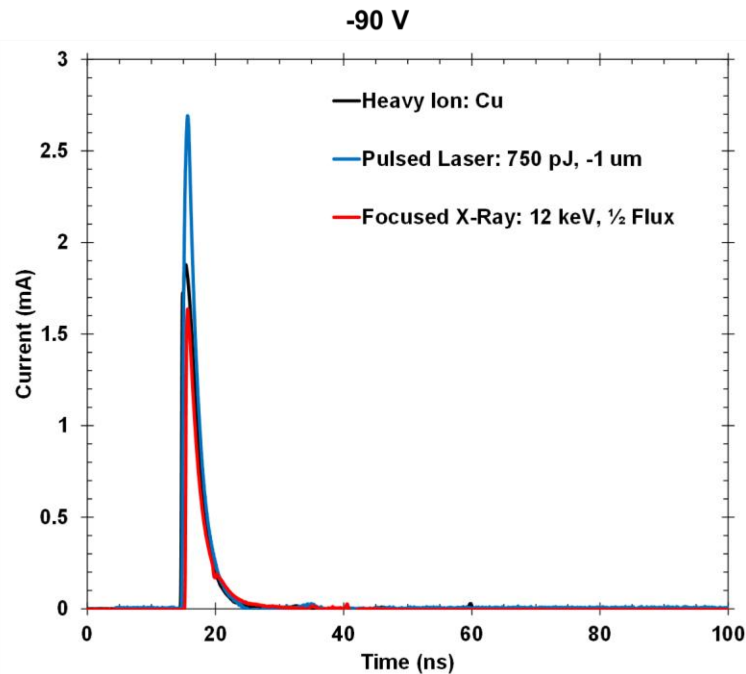

Figure VI.4. Averaged transients from the copper heavy ion (black), 750 pJ pulsed laser at a focal position of -1 µm (blue), and 12 keV, ½ flux focused X-ray (red) at a reverse bias of 90 V. Each of these radiation sources generated approximately 5.8 pC of charge in the diode's active region.

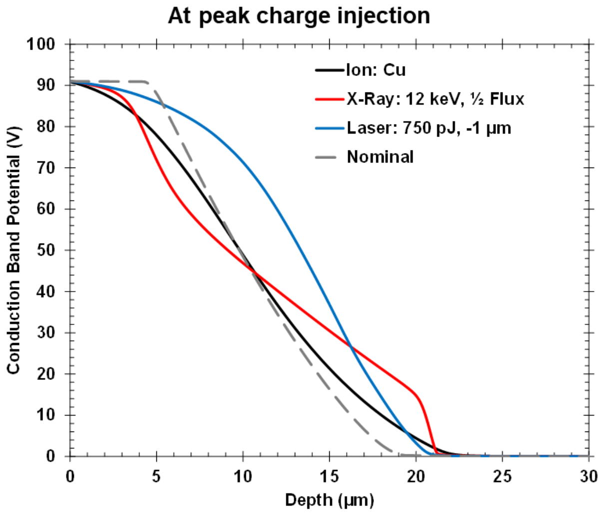

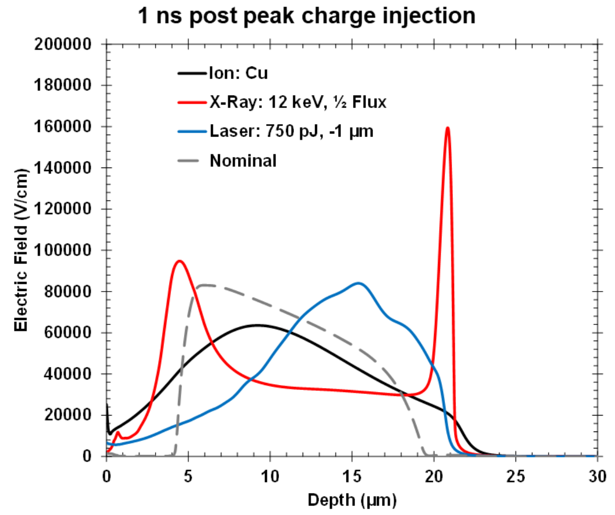

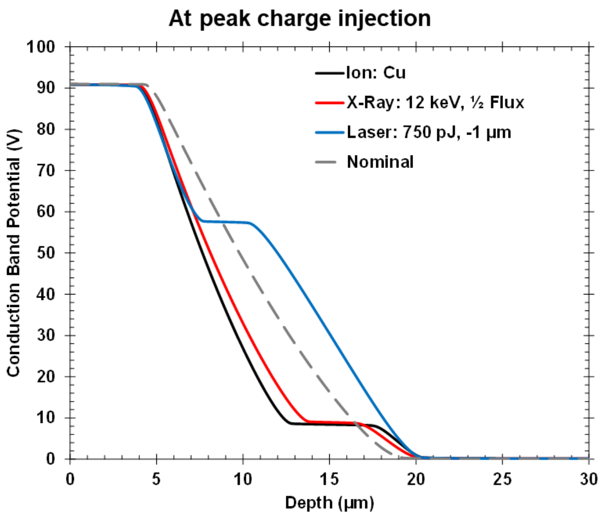

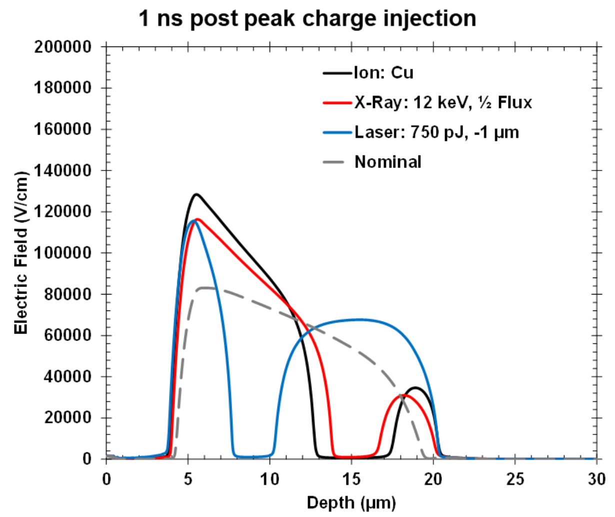

Figure VI.5. Copper heavy ion (black), 12 keV ½ flux focused X-ray (red), and 750 pJ -1 µm pulsed laser (blue) TCAD simulation results from the -90 V bias condition. Conduction band potential (left) and electric field (right) are shown at two time steps: at peak charge injection (top) and 1 ns post peak charge injection (bottom). Nominal conditions are denoted by the dashed grey lines.

Table VI.3. Summary of -90 V SETs resulting from ~5.8 pC of generated charge

SEE Source	Ion: Cu	Laser: 750 pJ, -1 µm	X-ray: 12 keV, ½ Flux
Generated Charge (pC)	5.8	5.8	5.5
Peak Current (mA)	2.0	2.6	1.6
Collected Charge (pC)	5.7	6.7	4.0
Rise Time (ns)	0.8	0.8	0.4
Fall Time (ns)	9.3	7.8	9.3
FWHM (ns)	2.4	2.2	1.8

Three SEE experimental conditions resulted in roughly 15 pC of generated charge in the diode's active region: the xenon heavy ion, the 8 keV full flux focused X-ray, and the 990 pJ pulsed laser at a focal position of 3.5 µm in the silicon. Experimental averaged SETs and the associated TCAD simulations for the -5 V bias condition are shown in Figure VI.6 and VI.7, respectively, and Table VI.4 contains the numerical data. The -90 V experimentally averaged SETs and TCAD simulation results are given in Figures VI.8 and VI.9, and the numerical data is provided in Table VI.5. Overall, the observations from the larger amount of generated charge are consistent with those seen at the lower charge generated value and the TCAD simulations provide similar support. The pulsed laser perturbs the nominal electric field more than the heavy ions or focused X-rays, especially at the lower bias condition, resulting in larger transients with slower drift-driven rise times and faster diffusion-driven fall times. Meanwhile, the focused X-rays produce less potential modulation, resulting in smaller transients with faster drift-driven rise times and slower diffusion-driven fall times. These observations are consistent with those derived from the sensitive volumes, further supporting the claim that the pulsed laser modulates the potential more than heavy ions, while the focused X-ray minimally perturbs the nominal depletion region.

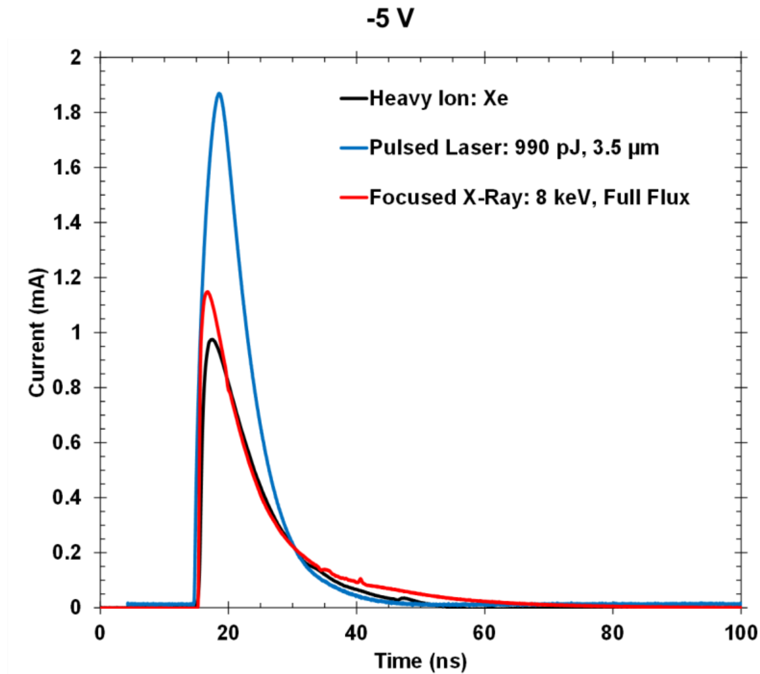

Figure VI.6. Averaged transients from the xenon heavy ion (black), 990 pJ pulsed laser at a focal position of 3.5 µm (blue), and 8 keV, full flux focused X-ray (red) at a reverse bias of 5 V. Each of these radiation sources generated approximately 15 pC of charge in the diode's active region.

Table VI.4. Summary of -5 V SETs resulting from ~15 pC of generated charge

SEE Source	Ion: Xe	Laser: 990 pJ, 3.5 µm	X-ray: 8 keV, Full Flux
Generated Charge (pC)	15.9	15.0	14.6
Peak Current (mA)	1.0	1.8	1.2
Collected Charge (pC)	10.5	16.1	10.9
Rise Time (ns)	2.0	3.3	1.2
Fall Time (ns)	37.9	21.9	37.5
FWHM (ns)	8.0	8.1	6.9

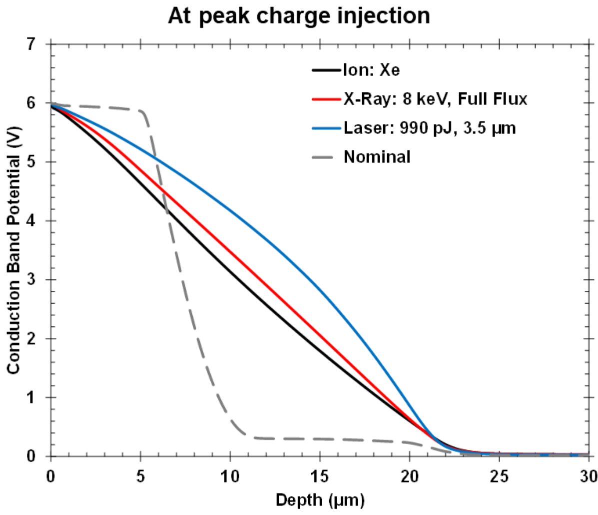

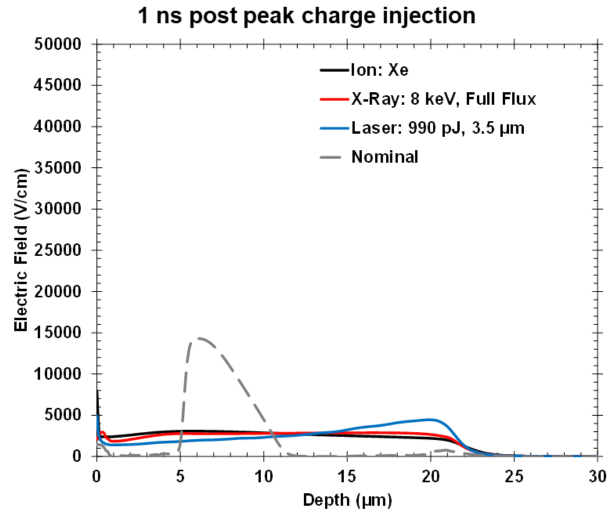

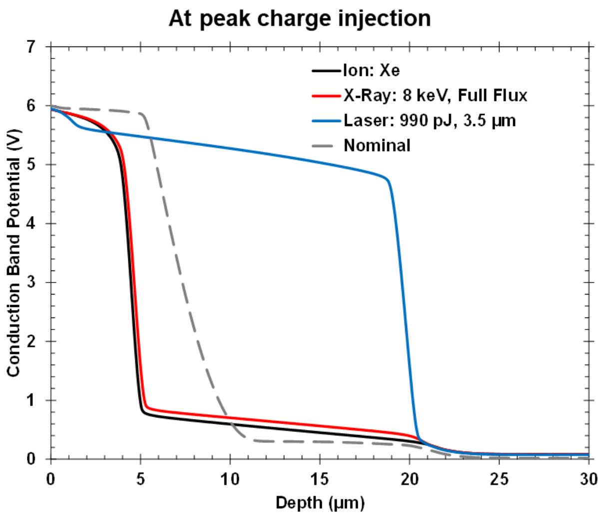

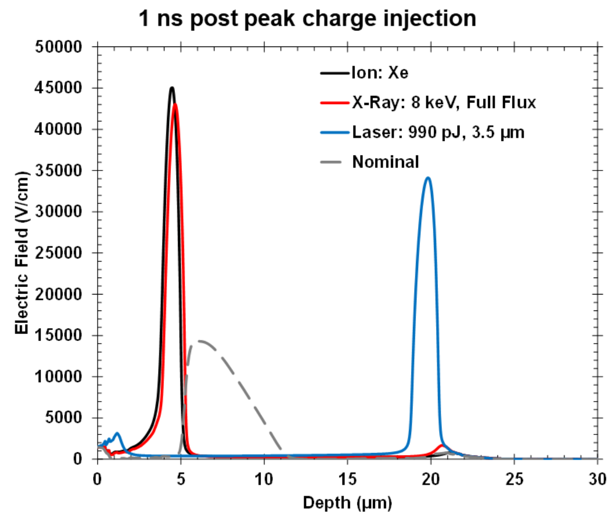

Figure VI.7. Xenon heavy ion (black), 8 keV full flux focused X-ray (red), and 990 pJ 3.5 µm pulsed laser (blue) TCAD simulation results from the -5 V bias condition. Conduction band potential (left) and electric field (right) are shown at two time steps: at peak charge injection (top) and 1 ns post peak charge injection (bottom). Nominal conditions are denoted by the dashed grey lines.

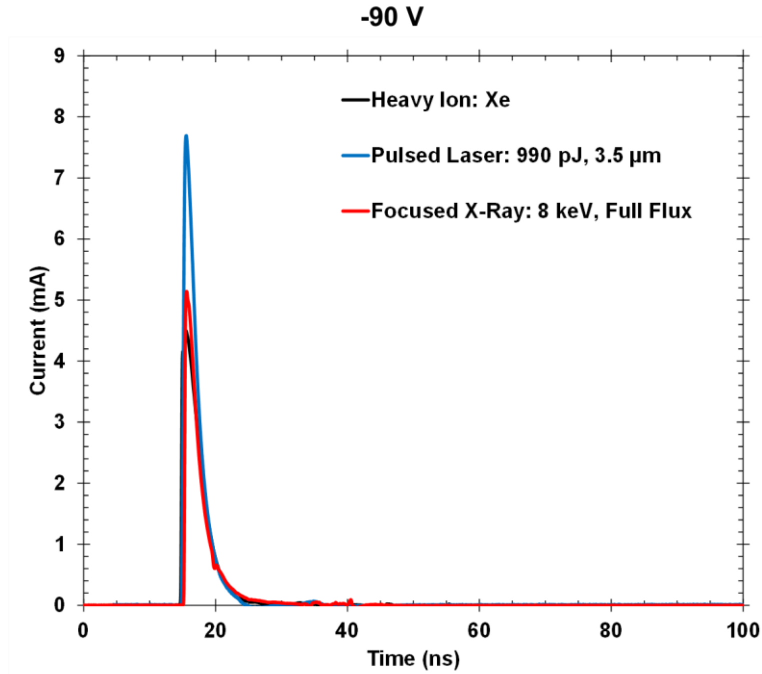

Figure VI.8. Averaged transients from the xenon heavy ion (black), 990 pJ pulsed laser at a focal position of 3.5 µm (blue), and 8 keV, full flux focused X-ray (red) at a reverse bias of 90 V. Each of these radiation sources generated approximately 15 pC of charge in the diode's active region.

Table VI.5. Summary of -90 V SETs resulting from ~15 pC of generated charge

SEE Source	Ion: Xe	Laser: 990 pJ, 3.5 µm	X-ray: 8 keV, Full Flux
Generated Charge (pC)	15.9	15.0	14.6
Peak Current (mA)	4.8	7.6	5.3
Collected Charge (pC)	16.1	20.0	13.8
Rise Time (ns)	0.9	0.8	0.5
Fall Time (ns)	11.1	8.2	9.6
FWHM (ns)	2.7	2.1	2.0

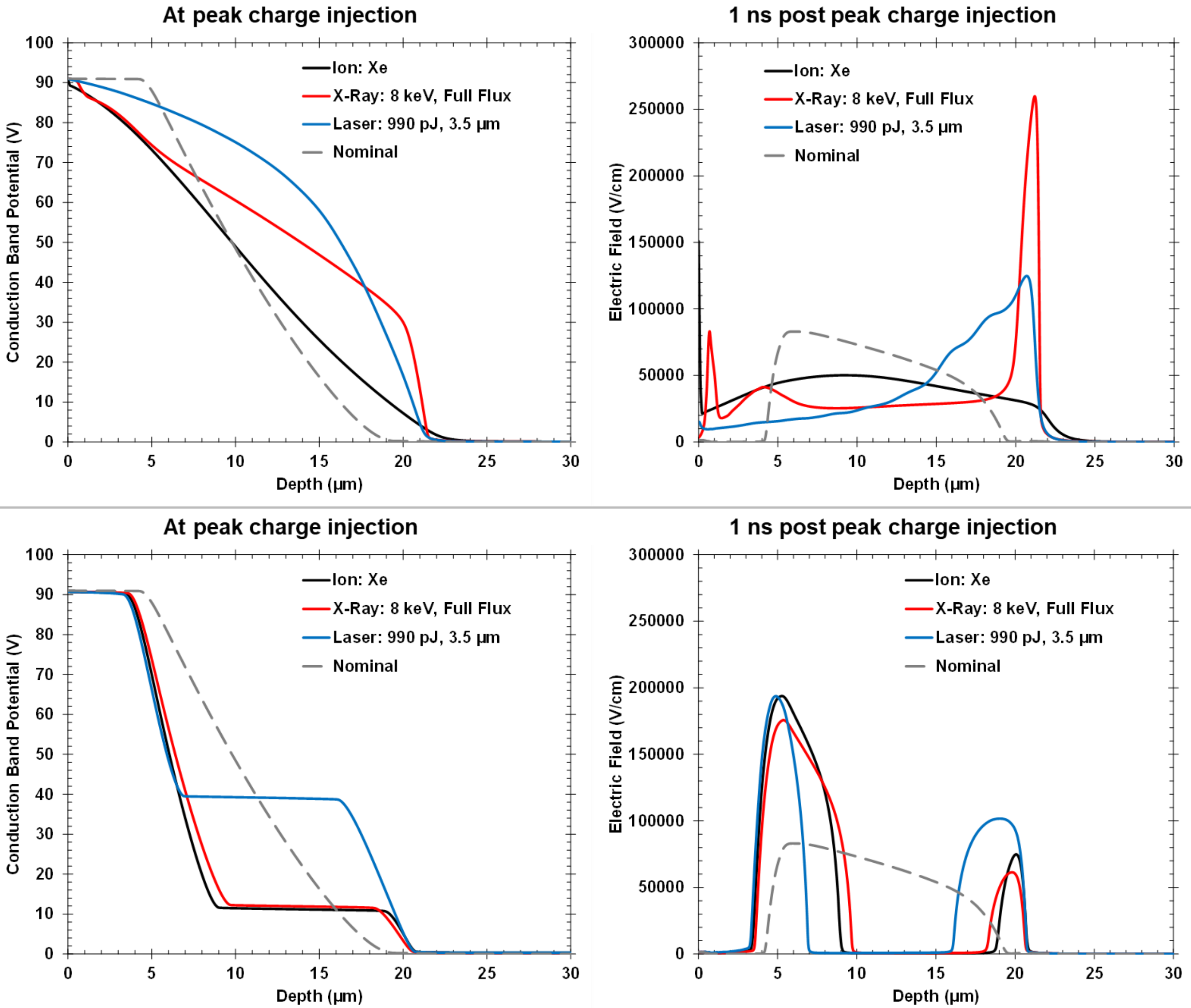

Figure VI.9. Xenon heavy ion (black), 8 keV full flux focused X-ray (red), and 990 pJ 3.5 µm pulsed laser (blue) TCAD simulation results from the -90 V bias condition. Conduction band potential (left) and electric field (right) are shown at two time steps: at peak charge injection (top) and 1 ns post peak charge injection (bottom). Nominal conditions are denoted by the dashed grey lines.

The trends in SET shape seen here are consistent with those seen in the sensitive volumes; radiation sources with larger sensitive volumes have more collected charge. Given that collected charge is used in the calculation of sensitive volumes, this is expected. The differences observed in the transient rise and fall times provide insight into the time-dependent behavior of the electric field. The faster rise times are indicative of a stronger electric field, which would result from less modulation. Longer fall times are also indicative of less modulation, as more charge is generated outside the depletion region and must diffuse before being collected. These conclusions are supported by the TCAD simulated potentials and electric field cuts.

C. Comparison of SET Shape Trends Across Radiation sources

Peak current, collected charge, transient rise time, transient fall time, and transient FWHM were examined as a function of collected charge and bias condition for each of the radiation sources. Here, the trends in SET shape characteristics are compared between the three radiation sources. It is observed that each radiation source results in different SET shape characteristic trends across generated charge and bias conditions. For the following figures heavy ion results are denoted by black circles, all focused X-ray photon energies are grouped together as red squares, and pulsed laser results are designated by triangles, with the color denoting the pulse energy: blue for 400 pJ, green for 750 pJ, and purple for 990 pJ.

All radiation sources showed a linear relationship between charge generated and peak current, with increased peak currents at the larger reverse bias condition. Figure VI.10 shows the -5 V (left) and -90 V (right) peak currents for all radiation sources. The pulsed laser, regardless of pulse energy, had greater peak currents per charge generated compared to the other sources, but increased the least with increased reverse bias. The focused X-ray-induced SETs, on the other hand, had the smallest peak current per generated charge. The heavy ion-induced peak current per generated charge is most similar to the peak currents generated by the focused X-rays at -5 V but

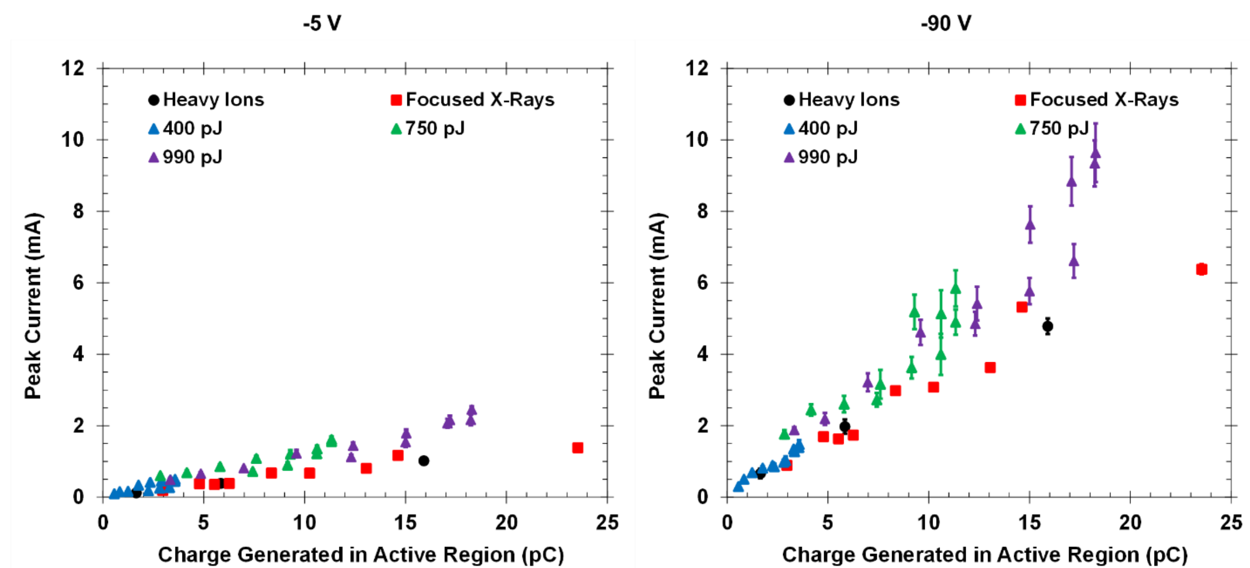

Figure VI.10. Peak current as a function of charge generated at -5 V (left) and -90 V (right) for heavy ion-, focused X-ray-, and pulsed laser-induced SETs.

shows a slightly greater increase with increased reverse bias. Despite the heavy ions showing the greatest increase in peak current per generated charge with increased reverse bias, pulsed laser-induced SETs still have substantially larger peak currents at -90 V.

As with peak current, collected charge shows a linear relationship to charge generated for all radiation sources. Figure VI.11 shows the -5 V (left) and -90 V (right) collected charge as a function of charge generated. The dashed grey line shows the unity collection efficiency. At -5 V, both heavy ion- and focused X-ray-induced SETs have similar collection efficiencies that are less than unity, while all laser pulse energies have collection efficiencies near unity. Increasing the reverse bias to -90 V causes the heavy ion-induced collection efficiency to increase to unity, while the focused X-ray-induced collection efficiency remains below unity. Pulsed laser-induced collection efficiency increases slightly above unity and shows the least amount of change with bias condition. These trends are consistent with those observed in the sensitive volumes and are demonstrative of differing amounts of potential modulation occurring between the radiation sources.

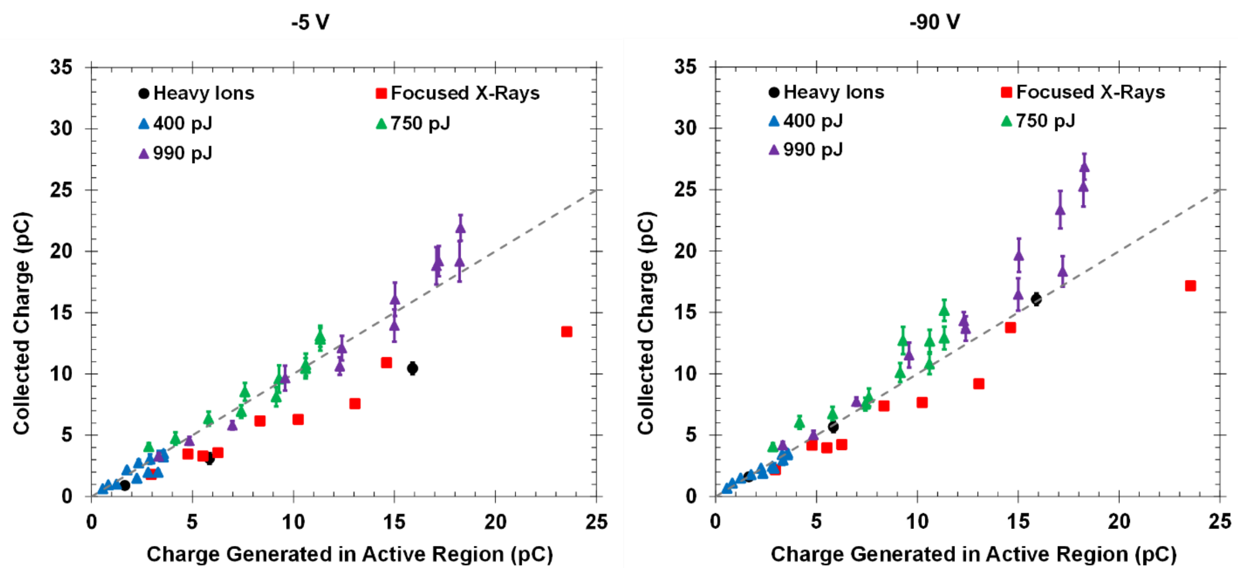

Figure VI.11. Collected charge as a function of charge generated at -5 V (left) and -90 V (right) for heavy ion-, focused X-ray-, and pulsed laser-induced SETs.

Transient rise times differ drastically between the radiation sources. Figure VI.12 shows the transient rise times at -5 V (left) and -90 V (right). The most distinctive feature in Figure VI.12 is

the multivalued nature of the pulsed laser-induced rise times, which is a unique by-product of the Gaussian-like charge generation profile (see ***Chapter IV.2*** for one-dimensional profiles). Heavy ion and focused X-ray, due to the linearity of their charge generated profiles, are unable to produce such a trend. The multivalued function of the pulsed laser-induced rise times demonstrates the importance focal position plays in device response. The second interesting feature is the lack of dependence the focused X-ray-induced rise times have with charge generated. Both other radiation sources display a distinct dependence on generated charge, particularly at -5 V. The focused X-ray also results in the fastest rise times, suggesting a stronger electric field than the other radiation sources. At -90 V, the transient rise times are more consistent amongst the radiation sources, which demonstrates the dominance of the increased nominal electric field.

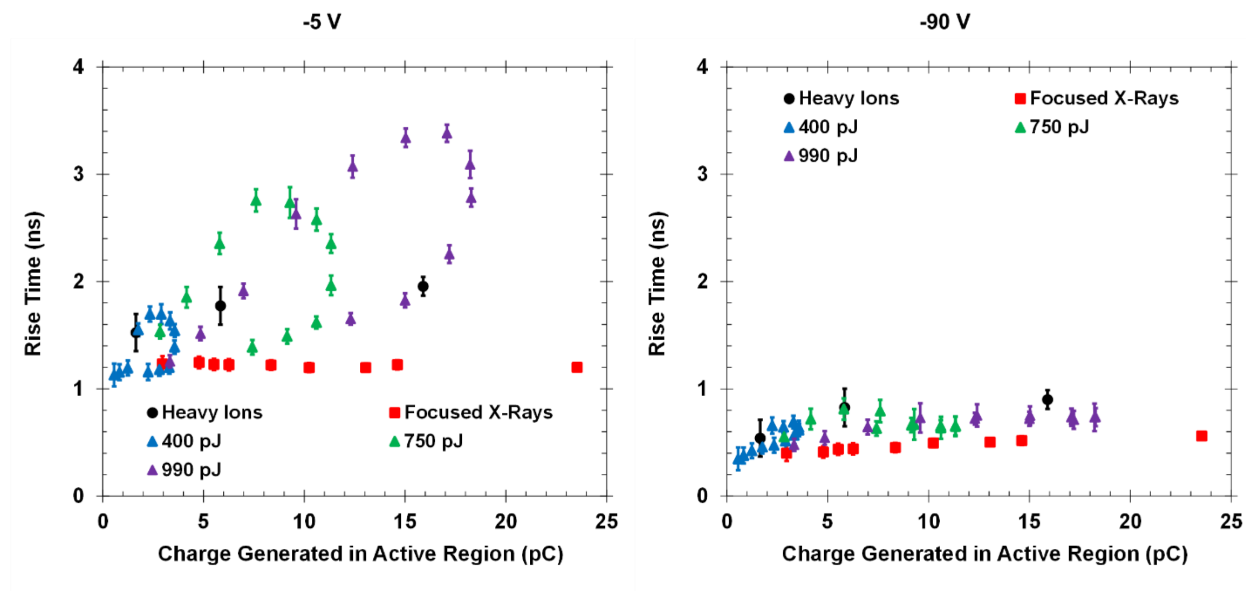

Figure VI.12. Transient rise time as a function of charge generated at -5 V (left) and -90 V (right) for heavy ion-, focused X-ray-, and pulsed laser-induced SETs.

Transient fall times, shown in Figure VI.13, show trends similar to those observed with the rise times. The pulsed laser once again shows a dependence on both charge generated and focal position, while the focused X-ray shows a lack of dependence on charge generated. Heavy ion-induced fall times fall somewhere between the pulsed laser and focused X-ray fall times. The focused X-ray also results in the longest fall times of the radiation sources, suggesting more charge collection through diffusion. As with the rise times, the transient fall times are more consistent at

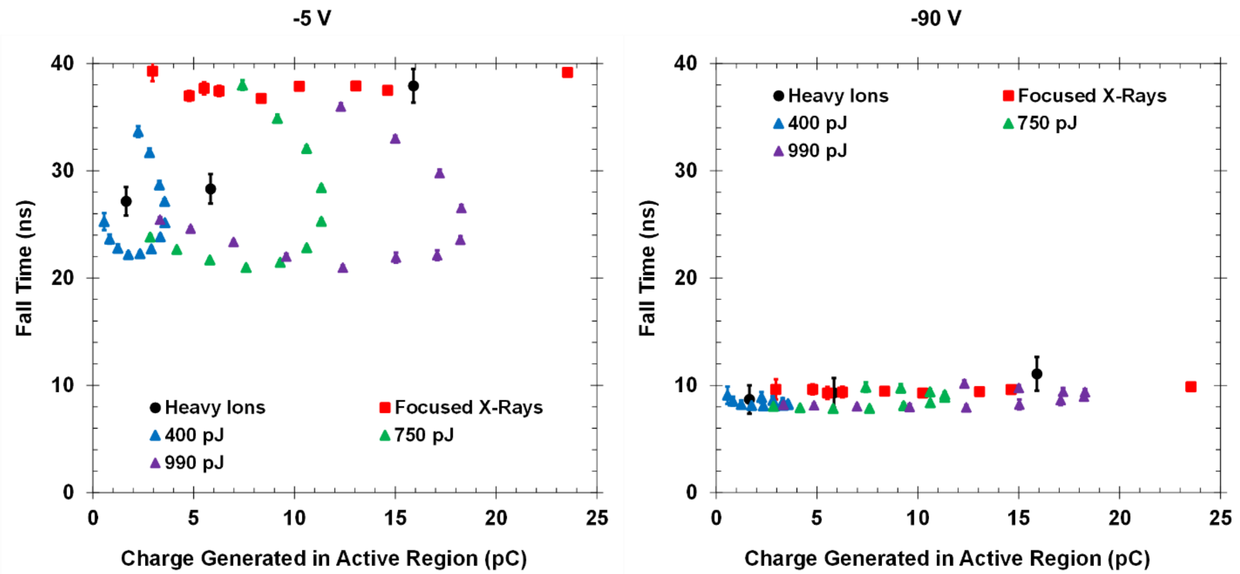

Figure VI.13. Transient fall time as a function of charge generated at -5 V (left) and -90 V (right) for heavy ion-, focused X-ray-, and pulsed laser-induced SETs.

the higher reverse bias condition, once again demonstrating the dominance of the nominal electric field on the device response.

Transient FWHMs are shown in Figure VI.14. Despite the differences in transient rise and fall time between the radiation sources, the FWHMs show more consistency. The pulsed laser-induced FWHMs shown some multivalued features, and the focused X-ray-induced FWHMs are more consistent with charge generated, but the absolute differences are smaller. The heavy ion-induced FWHMs are more consistent with the pulsed laser values than the focused X-ray. At -90 V, the FWHMs are faster and nearly identical due to the role the larger nominal electric field plays.

The observations obtained from SET shape comparisons are consistent with those from the sensitive volume and direct SET comparisons. At similar amounts of charge generated, pulsed laser-induced SETs have larger peak currents, more collected charge, slower transient rise times, and faster transient fall times compared to the other radiation sources. This is consistent with more potential modulation, resulting in a larger sensitive volume and a weaker electric field. The weaker electric field causes the slower rise time, but the larger sensitive volume results in more charge being collected by drift and therefore the faster fall times. The opposite is observed with the X-ray-induced SETs, which are smaller than those from the other radiation sources and have faster rise times and slower fall times. The smaller sensitive volume results in less charge collection, but

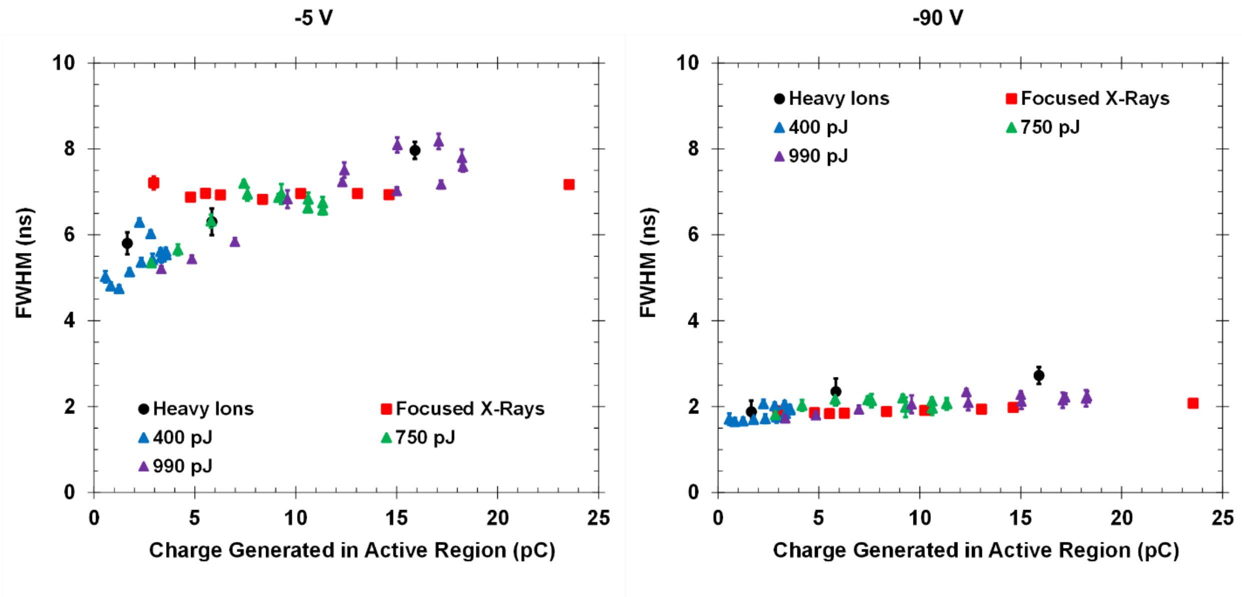

Figure VI.14. Transient FWHM as a function of charge generated at -5 V (left) and -90 V (right) for heavy ion-, focused X-ray-, and pulsed laser-induced SETs.

a stronger electric field and faster rise times. However, less charge is collected through drift and so the slower fall times result from the increased role of diffusion.

Comparing the TCAD simulated electric field cut trends for the different radiation sources from ***Chapter V*** confirms the experimentally derived conclusions. These electric field cuts have been reprinted in Figures VI.15 and VI.16 for the -5 V and -90V conditions, respectively. The differences in electric field strength between the various radiation sources at -5 V is most clear at 1 ns post peak charge injection, wherein the ion and X-ray electric fields are more similar to each other than the laser electric fields and are much stronger. In the -90 V simulations, discrepancies are clearest at the time of peak injection, with the ion and laser having the most similar strength in electric fields and the X-ray having stronger peak electric fields. Also in the -90 V simulations, all radiation sources show similar electric fields by 1 ns post peak charge injection, demonstrating the role the stronger nominal field plays in the device response. For both sets of simulations, the laser demonstrates a dependence on location of injected charge that cannot be observed in the cases of ion and X-ray injected charge, and a dependence on amount of charge generated is seen in all radiation sources. In summary, both the experimental results and the TCAD simulations show that the device response is dependent on the radiation source.

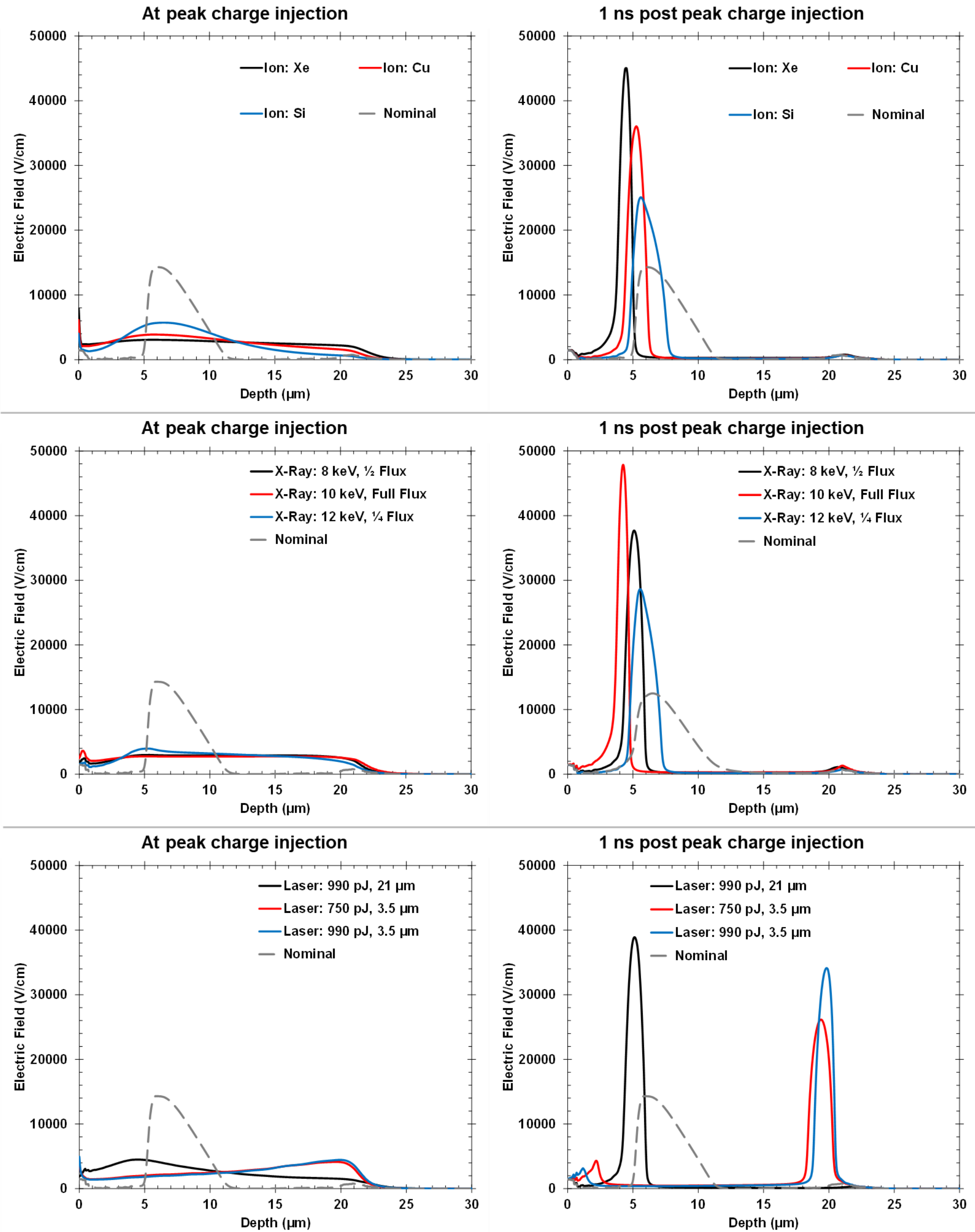

Figure VI.15. Electric field cuts from the -5 V TCAD simulations at the time of peak injection (left) and 1 ns post peak injection (right) for heavy ions (top), focused X-ray (middle), and pulsed laser (bottom).

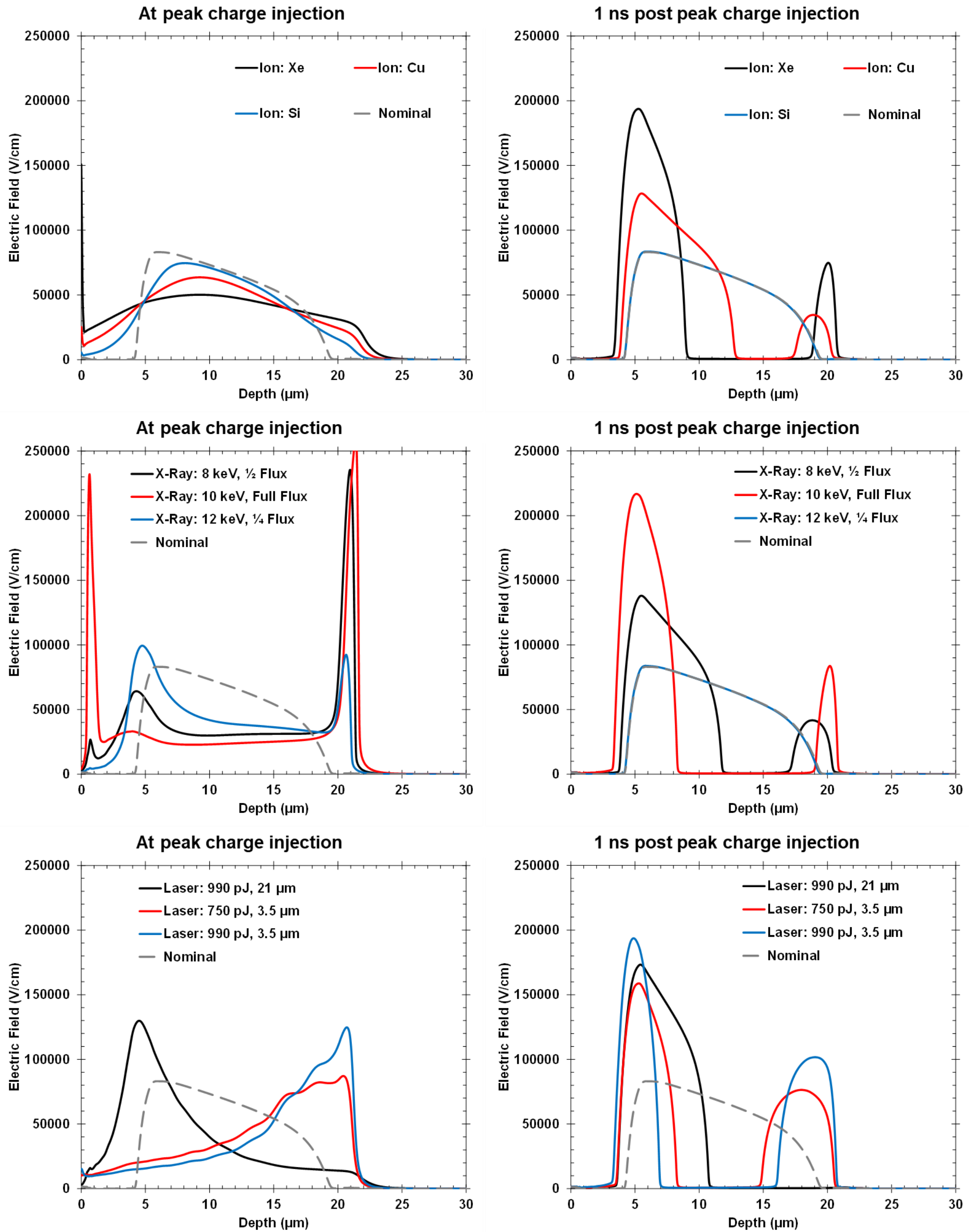

Figure VI.16. Electric field cuts from the -90 V TCAD simulations at the time of peak injection (left) and 1 ns post peak injection (right) for heavy ions (top), focused X-ray (middle), and pulsed laser (bottom).

D. Mechanisms

It was established previously in this chapter that the diode's SEE response is dependent on the radiation source. Based on the experimental results and TCAD simulations heavy ion-, focused X-ray-, and pulsed laser-induced charge generation result in differing amounts of potential modulation. While each radiation source displayed some device response dependence on amount of charge generated, which is expected due to changes in carrier density, this does not account for the disparities in potential modulation amongst the radiation sources. Given that the radiation sources all generated similar ranges of charge generated amounts, the observed variations in potential modulation must be due to differences in the charge generation profiles. The general shape of the charge generation profiles from each source was discussed in ***Chapter 4.A***, and there are several distinct features of each radiation source. Figure VI.17 shows linearly normalized charge generation profiles for each of the radiation sources as an illustration. The direction of propagation for the radiation sources is shown by the white arrow, starting at the surface of the device and moving further into the silicon. The charge generation is normalized from maximum (red) to minimum (blue) for each radiation source. Heavy ions (top) produce a long, nearly linear charge generation track with a very narrow radial width, typically approximated to be on the order of 50 to 100 nm, that inject charge over a time scale of ~500 fs. Focused X-rays (2nd to top) produce a long, nearly linear charge generation profile that is very similar to that of the heavy ions but has

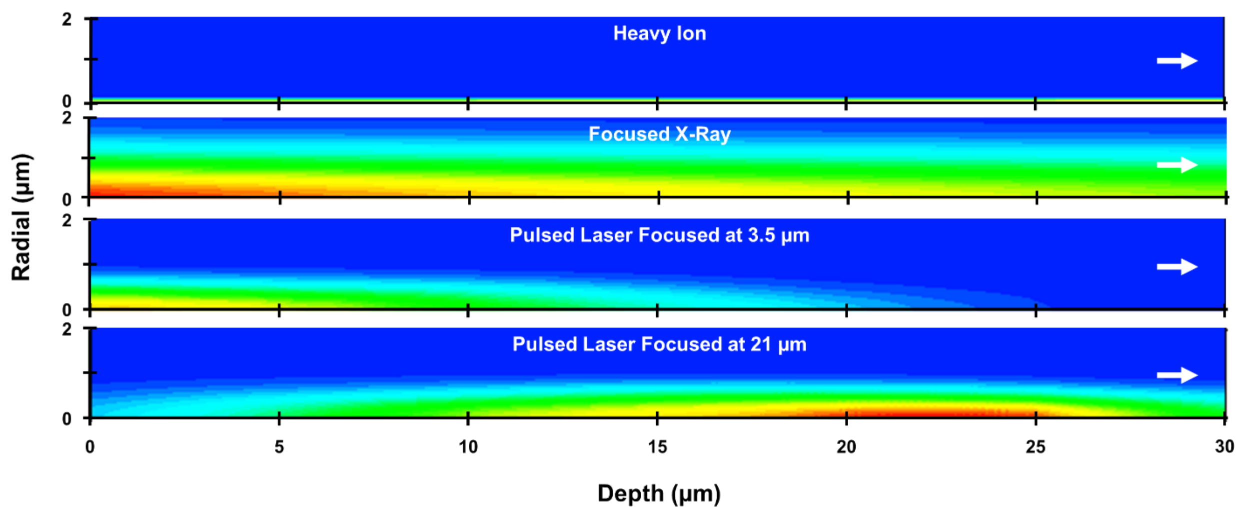

Figure VI.17. Normalized 2D charge generation profiles for heavy ions (top), focused X-rays (2nd to top), pulsed laser focused at3.5 µm into the silicon (2nd to bottom), and pulsed laser focused at 21 µm into the silicon (bottom).

a wider radial width, on the order of ~1 μm, and is injected over a longer time scale, ~100s of ps. The pulsed laser setup used in this work results in a charge generation profile that is roughly Gaussian in both the radial and lateral dimensions over a time scale akin to the ions; two focal positions are shown in Figure VI.17 (bottom two), demonstrating the effect the focal position has on location of generated charge.

Because there are multiple differing aspects of the charge generation profiles from the radiation sources, simplified TCAD simulations were performed to ascertain which of the charge generation profile aspects are most important to the observed differences in potential modulation. Using the same diode structure and simulation space presented in ***Chapter 4.C***, four sets of transient simulations were performed to explore the main differing aspects of charge injection, illustrated in Figure VI.18: (1) temporal duration, (2) radial width, (3) range, and (4) starting location. For all the simulations, the amount of charge generated in the diode's active region was kept constant at 15 pC and a Gaussian radial distribution was used.

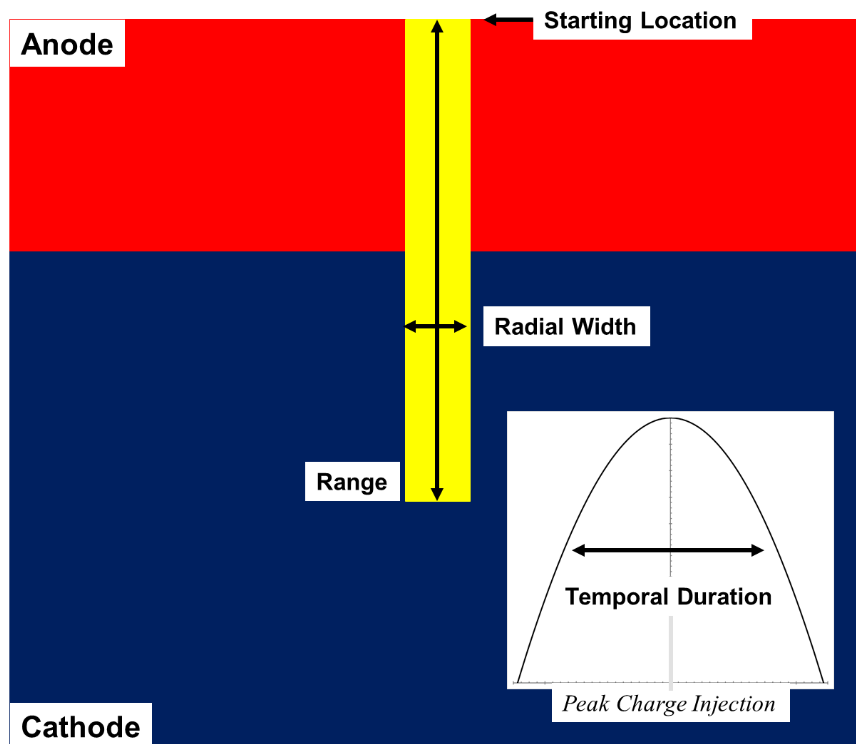

Figure VI.18. Illustration of the charge generation profile aspects. Temporal duration refers to the length of time over which the charge is injected and is Gaussian in shape. Range refers to how long the charge generation profile is. Radial width refers to the radial Gaussian width of the initial charge injection. Starting location refers to the location in the diode where the charge injection begins.

1) *Temporal Duration of Charge Injection*

Six sets of simulations were run to explore the effect the temporal duration of charge injection has on device response. The simulations use TCAD's *HeavyIon* statement for simplicity, with a range of 90 µm, a constant LET of 0.6 pC/µm, and a radial FWHM of 83 nm. Heavy ions in TCAD are injected over a Gaussian distributed time with a default $1/e^2$ time envelope of 4 ps; in these simulations, the time envelope was varied over several orders of magnitude at values of 40 fs, 4 ps, and 400 ps. Bias conditions of -5 V and -90 V were used.

Electric field cuts were taken at several time points during the transients and are shown in Figure VI.19. The top set of curves are from the -5 V simulations and the bottom set of curves are

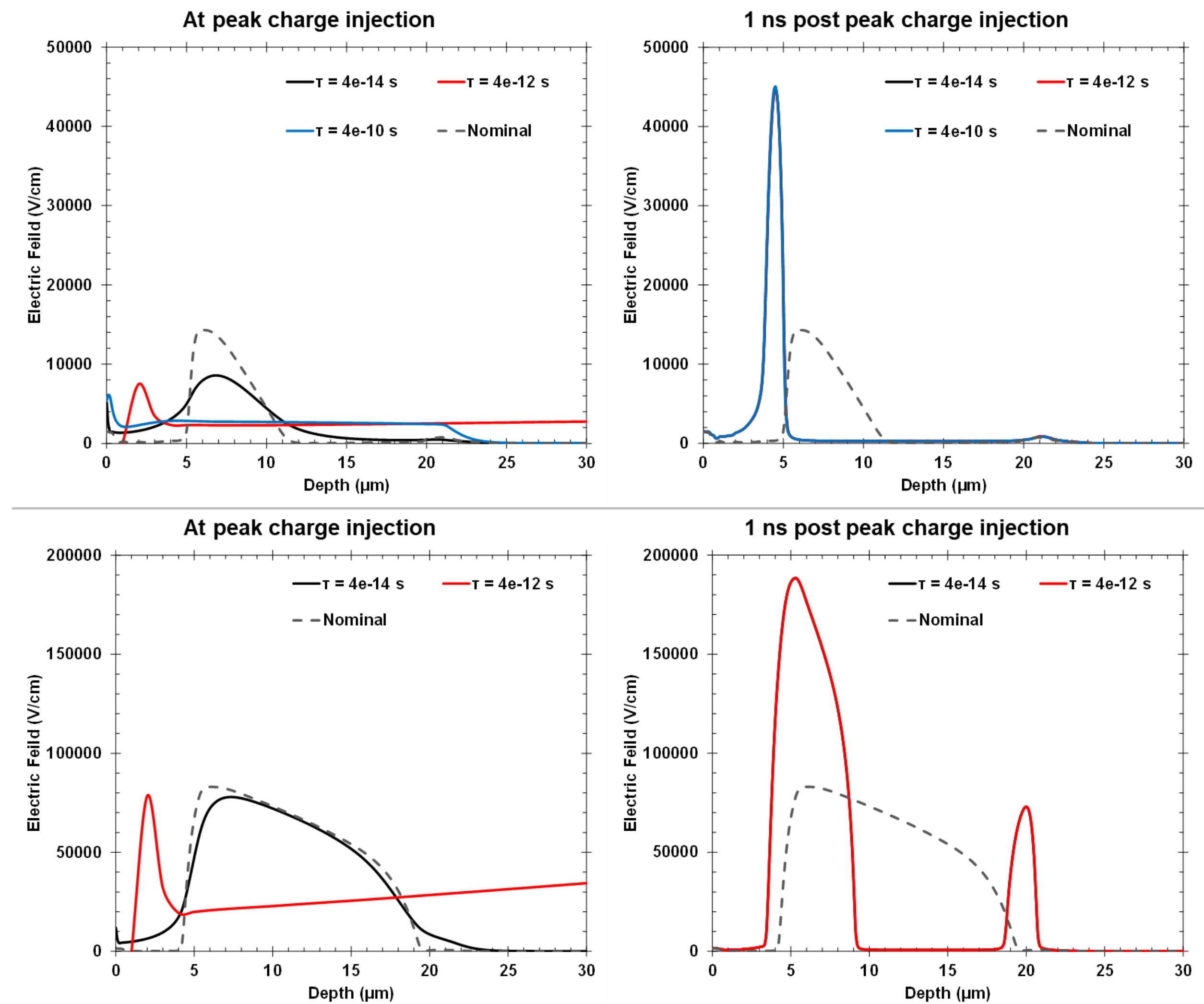

Figure VI.19. Electric field cuts for the -5 V (top) and -90 V (bottom) TCAD simulations examining pulse duration at the time of peak charge injection (left) and 1 ns post peak injection (right).

for the -90 V simulations. For both bias conditions, there is some variation in electric field modulation between the different injection duration for the peak-injection cases, but the overall magnitude of the electric field is consistent. By 1 ns post peak injection the electric fields are indistinguishable. It should be noted that the 400 ps temporal duration is not shown in the -90 V results; this simulation was experiencing convergence errors that prevented it from running. However, based on the results from the other simulations it is expected that the results would not be significantly different from the other -90 V simulations.

Given that the range of injection duration used here is wider than those occuring in real experimental conditions, it can be presumed that the injection duration has little to no effect on the overall device response in the experiments performed in this work. However, caution should be taken when working with high speed devices. The focused X-ray has a $1/e^2$ pulse duration of 144 ps, which could affect devices operating at frequencies higher than approximately 7 GHz.

2) *Radial Width of Charge Injection*

Six sets of simulations were run to explore the effect the radial width of charge injection has on device response. The simulations use TCAD's *HeavyIon* statement for simplicity, with a range of 90 µm, a constant LET of 0.6 pC/µm, and $1/e^2$ Gaussian distributed time envelope of 4 ps. Radial FWHM values of 83 nm, 830 nm, and 4.2 µm were used to explore the effects of radial width. The radial FWHM value of 83 nm is one of the common widths used when simulating heavy ion SEEs in TCAD and corresponds to the 1/e radius of 100 nm. Bias conditions of -5 V and -90 V were used.

Electric field cuts were taken at several time points during the transients and are shown in Figure VI.20. The top set of curves are from the -5 V simulations and the bottom set of curves are for the -90 V simulations. The differences in the -5 V simulations are most notable at 1 ns post peak charge injection, in which the wider radial districutions result in weaker electrics field that are distributed over a wider area. At -90 V, discrepancies can be seen at both time steps, though they are most promient at the time of peak injection. Overall, the high bias simulations show the same trends as the lower bias condition: a wider radial distribution results in less potential modulation. This can be expected, as the same amount of charge is being injected over a wider area, resulting in lower carrier densities.

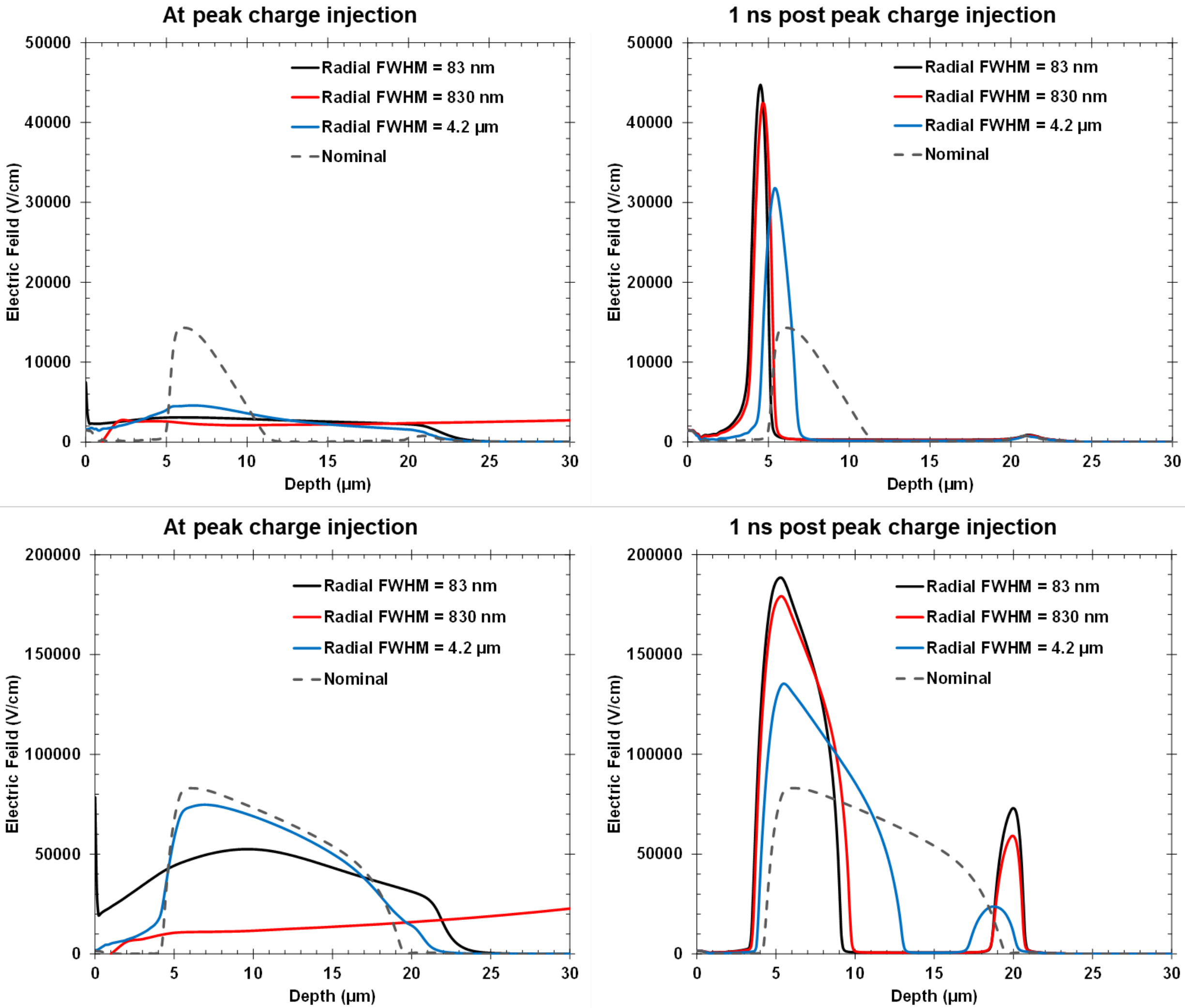

Figure VI.20. Electric field cuts for the -5 V (top) and -90 V (bottom) TCAD simulations examining radial distribution width at the time of peak charge injection (left) and 1 ns post peak injection (right).

Based on the conclusions from these simulations, the most of observed differences between the heavy ion and focused X-ray experiments, and some of the differences between the heavy ion and pulsed laser experiments can be attributed to the differences in radial widths.

3) Range of Charge Injection

Six sets of simulations were run to explore the effect the starting location of charge injection has on device response. The simulations use TCAD's *HeavyIon* statement with a radial FWHM of 83 nm and $1/e^2$ Gaussian distributed time envelope of 4 ps. The ranges of the injected charge were 90 µm, 10 µm, and 5 µm. The constant LET was adjusted for each range to maintain 15 pC of

generated charge in the active region, resulting in LETs of 0.6 pC/μm, 1.5 pC/μm, and 3 pC/μm, respectively. Bias conditions of -5 V and -90 V were used.

Electric field cuts were taken at several time points during the transients and are shown in Figure VI.21. The top set of curves are from the -5 V simulations and the bottom set of curves are for the -90 V simulations. Both bias conditions show a dependence on the range of the injected charge, with the long range charge injection modulating the electric field toward the surface of the device and the short range charge injection modulating the electric field toward the substrate. In all cases, the electric field is being pushed away from the regions with the highest density of excess carriers. The short range charge injection conditions generate all the excess carriers in the upper

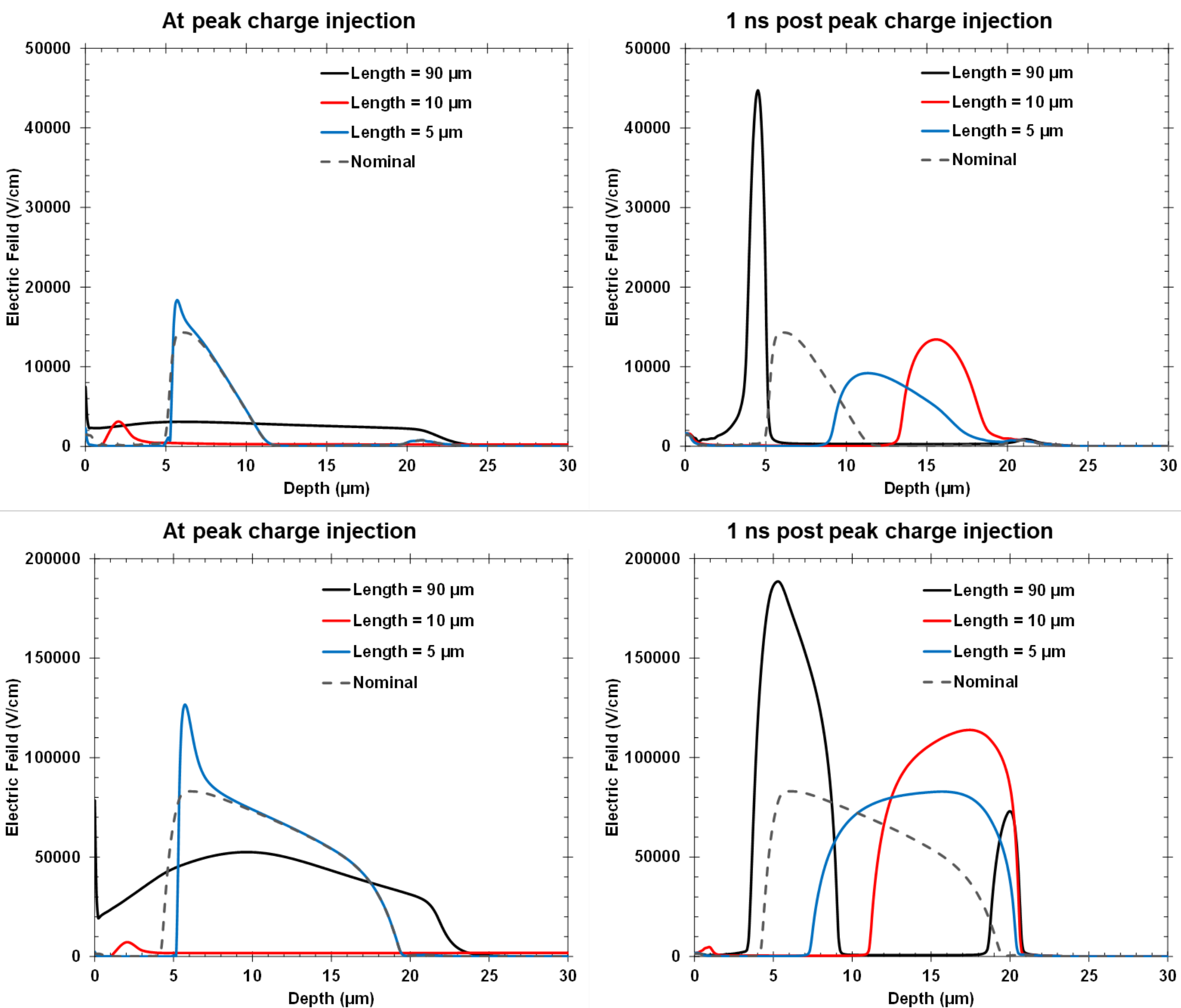

Figure VI.21. Electric field cuts for the -5 V (top) and -90 V (bottom) TCAD simulations examining the range of charge injection at the time of peak charge injection (left) and 1 ns post peak injection (right).

portion of the diode, near the contact, while the long range injection condition generates most of its charge in the epitaxial layer and substrate.

Both the ions and X-rays generate charge over a long range, penetrating deep into the substrate, while the laser has a more confined range similar to the short range simulations seen here. Based on these simulations, the differences observed between the heavy ion and pulsed laser experiments, and the focused X-ray and pulsed laser experiments are impacted heavily by the differences in charge injection range.

4) Starting Location of Charge Injection

Six sets of simulations were run to explore the effect the starting location of charge injection has on device response. The simulations use TCAD's *HeavyIon* statement, with a range of 10 µm, constant LET of 1.5 pC/µm, radial FWHM of 83 nm, and $1/e^2$ Gaussian distributed time envelope of 4 ps. The starting location for charge injection was set to 0 µm (device surface) 10 µm, and 20 µm. Bias conditions of -5 V and -90 V were used.

Electric field cuts were taken at several time points during the transients and are shown in Figure VI.22. The top set of curves are from the -5 V simulations and the bottom set of curves are for the -90 V simulations. For both bias conditions, the location of the electric field region is dependent on the starting location of charge injection, with the potential being modulated away from the excess carriers. For the surface starting location that means the electric field region is pushed towards the substrate, while the other starting locations push the electric field region into the p+ region toward the device contact.

These simulations most closely resemble the different pulsed laser focal positions, and based on these simulations, the observed differences between focal positions comes down to location of injected charge. Given that the heavy ions and focused X-rays always begin their charge injection at the suface of the device, location of charge is not a major factor in their device responses.

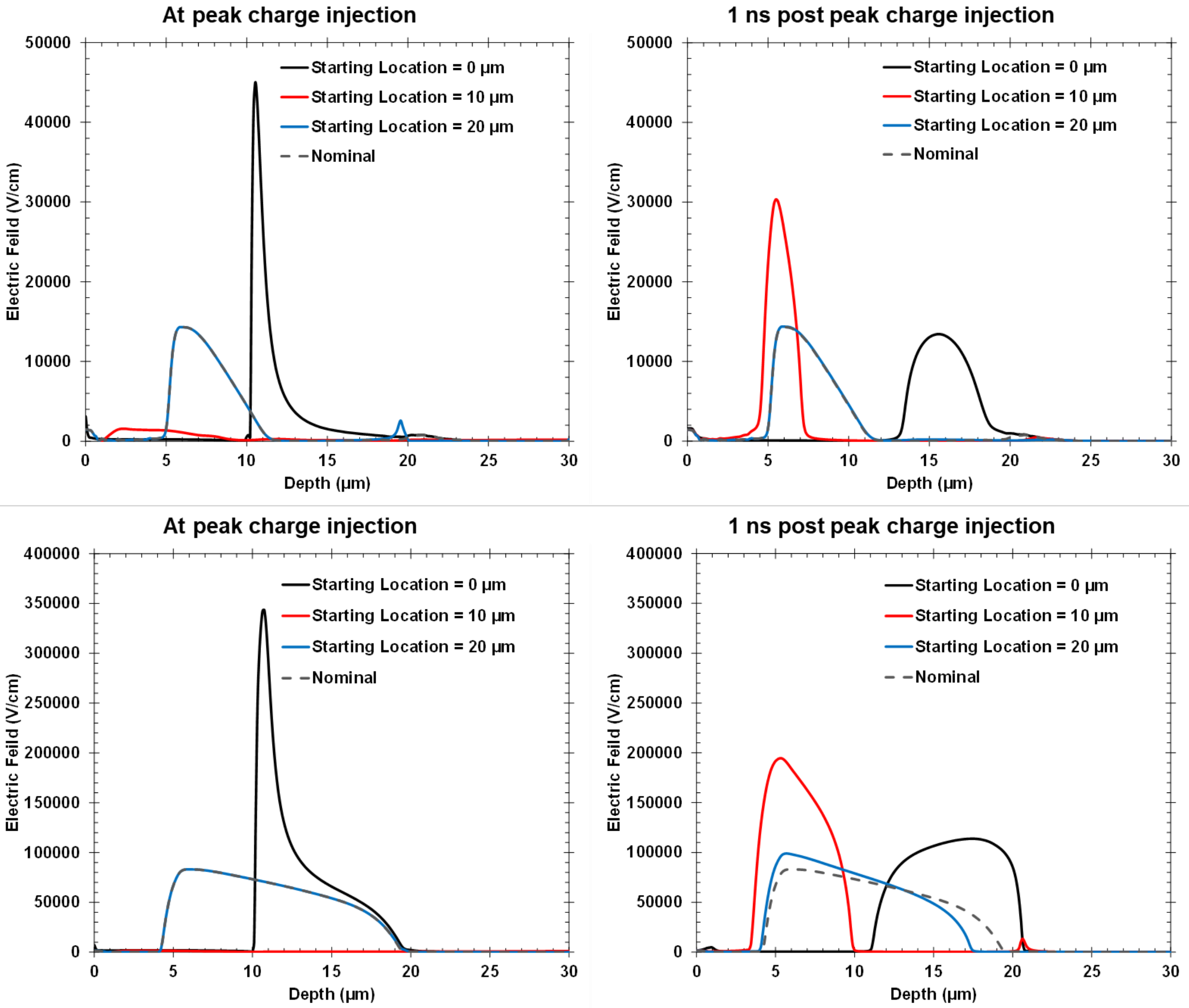

Figure VI.22. Electric field cuts for the -5 V (top) and -90 V (bottom) TCAD simulations examining starting location of charge injection at the time of peak charge injection (left) and 1 ns post peak injection (right).

CHAPTER VII

CONCLUSIONS AND FUTURE WORK

As the demand for spacecraft increases, so too will the demand for radiation effects testing. The availability of high energy particle accelerators is already struggling to meet current demand, and alternative SEE testing methods are being investigated as possible ways to meet demand. Two of these alternative methods are the picosecond focused X-ray and femtosecond pulsed laser, which generate charge through the absorption of photons. Both of these alternative radiation sources have distinct testing advantages over heavy ions and each other, such as improved spatial and temporal control over charge generation, motivating interest in their use separately from the conventional facility shortage. However, their ability to replace conventional heavy ions for spacecraft validation remains to be seen.

This work used a large area, epitaxial silicon diode to explore the charge collection mechanisms from heavy ion-, pulsed laser-, and focused X-ray-induced charge generation. SET experiments were performed using all three radiation sources over similar ranges of charge generated in the diode's active region. The experimental data was compared three ways: (1) comparing sensitive volumes, (2) comparing SETs from each source at comparable generated charge values, and (3) comparing the trends in SET shape as a function of bias condition and amount of generated charge. All three comparisons resulted in the same conclusions; each SEE modulates the diode's internal potential differently, resulting in the observed variations in device response.

Sentaurus TCAD simulations were used to first verify the differences in potential modulation from the experimental results, and then were used to explore which aspects of the radiation sources were responsible for the differences. By varying individual aspects of the charge generation profiles, it could be seen that the most important features to affect the device response were the range and starting location of the injected charge, with radial distribution contributing a small amount of variation and temporal duration having almost no effect on this device. The range and starting location of injected charge heavily affect the location of excess carriers, which in turn effects where and by how much the potential is modulated. The radial width of charge injection is a factor in the density of the excess carriers but is less significant in the overall device response than range and starting location.

While this work focused on the SET response of a large area, epitaxial diode, the conclusions can be generalized to other SEEs and device types. For instance, SEGR and SEB are heavily dependent on the electric fields within power devices. Because the various charge generation profiles modulate the potential and electric field differently for the same amount of generated charge, there could be discrepancies in the amount of generated charge necessary to induce gate rupture and burnout. On the other hand, SEUs in SOI technologies will probably occur under very similar charge generated circumstances due to smaller sensitive volumes and confined regions for modulation to occur. High speed devices, operating at frequencies greater than 7 GHz, may experience different device responses when being exposed to the long X-ray pulsed compared to the faster ions and laser pulses. Finally, the wider radial spot sizes of laser and X-ray pulses can generate charge in multiple transistors simultaneously in high density chips, which may complicate testing efforts.

This work has demonstrated that different charge generation sources result in different device responses, even when the amount of generated charge is equivalent. The differences in device response are caused by variations in the excess carrier density and location, which affect how the potential and electric field are modulated during the transient event, and complicate efforts for developing a universal, predictive correlation methods for the radiation sources. There are still many benefits to using the alternative radiation sources compared to conventional ion facilities, and the necessity of them will increase as demand for SEE testing increases. In the end, alternative SEE testing methods show promise for basic research and *ad hoc* correlations to heavy ion testing.

References

[1] Explorer 1 Overview, NASA. [Online] Available at: https://www.nasa.gov/mission_pages/explorer/explorer-overview.html.

[2] R-Gentic Commonly Used Acronyms in Radiation Analysis Accessed: Jan. 2021 [Online] Available: https://vanguard.isde.vanderbilt.edu/RGentic/.

[3] The National Academies of Sciences, Engineering, Medicine, “Testing at the Speed of Light: The State of U.S. Electronic Parts Space Radiation Testing Infrastructure,” Consensus Study Report, 2018.

[4] J. S. Melinger, S. Buchner, D. McMorrow, W. J. Stapor, T. R. Weatherford, and A. B. Campbell, “Critical Evaluation of the Pulsed Laser Method for Single Event Effects Testing and Fundamental Studies,” *IEEE Trans. Nucl. Sci.*, vol. 41, no. 6, pp. 2574-2584, Dec. 1994.

[5] [Online] Available at: https://www.technologyreview.com/2019/06/26/134510/asteroid-mining-bubble-burst-history/.

[6] [Online] Available at: https://telanganatoday.com/race-for-space-wealth.

[7] [Online] Available at: https://news.watercloudsolutions.com/news/86284/space-tourism-a-market-worth-observing-growth-space-adventures-eads-astrium-virgin-galactic/.

[8] [Online] Available at: https://www.cnn.com/2020/05/05/investing/virgin-galactic-earnings-stock-scn/index.html.

[9] [Online] Available at: https://www.nasa.gov/topics/moon-to-mars.

[10] [Online] Available at: https://exploration.esa.int/web/mars/.

[11] [Online] Available at: http://mmx.isas.jaxa.jp/en/.

[12] Nikkei Science, Inc. of Japan, image by K. Endo.

[13] S. Bourdarie and M. Xapsos, “The Near-Earth Space Radiation Environment,” *IEEE Trans. Nucl. Sci.*, vol. 55, no. 4, pp. 1810-1832, Aug. 2008.

[14] E. G. Stassinopoulos and J. P. Raymond, “The Space Radiation Environment for Electronics,” *Proceedings of the IEEE*, vol. 76, no. 11, pp. 1423-1442, Nov. 1988.

[15] J. L. Barth, C. S. Dyer, and E. G. Stassinopoulos, “Space, Atmospheric, and Terrestrial Radiation Environments,” *IEEE Trans. Nucl. Sci*, vol. 55, no. 3, pp. 466-482, Jun. 2003.

[16] T. R. Oldham and F. B. McLean, "Total ionizing dose effects in MOS oxides and devices," *IEEE Trans. Nucl. Sci.*, vol. 50, no. 3, pp. 483-499, Jun. 2003.

[17] J. R. Srour, C. J. Marshall, and P. W. Marshall, “Review of displacement damage effects in silicon devices,” *IEEE Trans. Nucl. Sci.*, vol. 50, no. 3, pp. 653–670, Jun. 2003.

[18] D. Binder, E. C. Smith, and A. B. Holman, "Satellite Anomalies from Galactic Cosmic Rays," *IEEE Trans. Nucl. Sci.*, vol. 22, no. 6, pp. 2675-2680. Dec. 1975.

[19] W. A. Kolasinski, J. B. Blake, J. K. Anthony, W. E. Price, and E. C. Smith, "Simulation of Cosmic-Ray Induced Soft Errors and Latchup in Integrated-Circuit Computer Memories," *IEEE Trans. Nucl. Sci.*, vol. 26, no. 6, pp. 5087-5091. Dec. 1979.

[20] SPENVIS – The Space Environment Information System Accessed: Jan. 2021 [Online] Available: https://www.spenvis.oma.be/.

[21] P. E. Dodd and L. W. Massengill, "Basic mechanisms and modeling of single-event upset in digital microelectronics," *IEEE Trans. Nucl. Sci.*, vol. 50, no. 3, pp. 583-602, Jun. 2003.

[22] R. Reed, "Fundamental Mechanisms for Single Particle-Induced Soft Errors," *IEEE NSREC Short Course Notebook*, J. D. Black, Ed., Tucson, Arizona, Jul. 14 2008, Ch. 1.

[23] G. C. Messenger, "Collection of charge on junction nodes from ion tracks," *IEEE Trans. Nucl. Sci.*, vol. 29, no. 6, pp. 2024-2031, Dec. 1982.

[24] NASA Goddard. Radiation Effects & Analysis: Single Event Effects. Accessed on: May 20, 2020. [Online] Available at: https://radhome.gsfc.nasa.gov/radhome/see.htm.

[25] G. H. Johnson, J. M. Palau, C. Dachs, K. F. Galloway, and R. D. Schrimpf, "A Review of the Techniques Used for Modeling Single-Event Effects in Power MOSFET's," *IEEE Trans. Nucl. Sci.*, vol. 43, no. 2, pp. 546-560, Apr. 1996.

[26] S. Liu, M. Boden, D. A. Girdhar, and J. L. Titus, "Single-Event Burnout and Avalanche Characteristics of Power DMOSFETs," *IEEE Trans. Nucl. Sci.*, vol. 53, no. 6, pp. 3379-3385, Dec. 2006.

[27] L. W. Massengill, "SEU modeling and prediction techniques," *IEEE NSREC Short Course Notebook*, A. Johnston, Ed., Snowbird, Utah, Jul. 19, 1993, Ch. 3.

[28] P. J. McNulty, W. J. Beauvais, and D. R. Roth, "Determination of SEU parameters of NMOS and CMOS SRAMs," *IEEE Trans. Nucl. Sci.*, vol. 38, pp. 1463-1470, Dec. 1991.

[29] L. W. Massengill, "Cosmic and terrestrial single-event radiation effects in dynamic random access memories," *IEEE Trans. Nucl. Sci.*, vol. 43, pp. 576-593, Apr. 1996.

[30] P. E. Dodd, J. R. Schwank, M. R. Shaneyfelt, J. A. Felix, P. Paillet, V. Ferlet-Carvrois, J. Baggio, R. A. Reed, K. M. Warren, R. A. Weller, R. D. Schrimpf, G. L. Hash, S. M. Dalton, K. Hirose, and H. Saito, "Impact of Heavy Ion Energy and Nuclear Interactions on Single-Event Upset and Latchup in Integrated Circuits," *IEEE Trans. Nucl. Sci.*, vol. 54, no. 6, pp. 2303-2311, Dec. 2007.

[31] J. A. Zoutendyk, L. D. Edmonds, and L. S. Smith, "Characterization of multiple-bit errors from single-ion tracks in integrated circuits," *IEEE Trans. Nucl. Sci.*, vol. 36, no. 6, pp. 2267-2274, Dec. 1989.

[32] O. Musseau, F. Gardic, P. Roche, T. Corbiere, R. A. Reed, S. Buchner, P. McDonald, J. Melinger, L. Tran, and A. B. Campbell, "Analysis of Multiple Bit Upsets (MBU) in a CMOS SRAM," *IEEE Trans. Nucl. Sci.*, vol. 43, no. 6, pp. 2879-2888, Dec. 1996.

[33] D. G. Mavis and P. H. Eaton, "SEU and SET Modeling and Mitigation in Deep Submicron Technologies," *IEEE 45th Annual International Reliability 293 Physics Symposium*, Phoenix, 2007.

[34] R. Koga, S. H. Penzin, K. B. Crawford, and W. R. Crain, "Single Event Functional Interrupt (SEFI) Sensitivity in Microcircuits," *4th European Conference on Radiation and its Effects on Components and Systems (RADECS)*, Cannes, France, pp. 331-318, 1997.

[35] G. H. Johnson, J. M. Palau, C. Dachs, K. F. Galloway, and R. D. Schrimpf, "A review of the techniques used for modeling single-event effects in power MOSFETs," *IEEE Trans. Nucl. Sci.*, vol. 43, no. 2, pp. 546-560, Apr. 1996.

[36] J. L. Titus and C. F. Wheatley, "Experimental studies of single-event gate rupture and burnout in vertical power MOSFETs," *IEEE Trans. Nucl. Sci.*, vol. 43, no. 2, pp. 533-545, Apr. 1996.

[37] J. L. Titus, "An Updated Perspective of Single Event Gate Rupture and Single Event Burnout in Power MOSFETs," *IEEE Trans. Nucl. Sci.*, vol. 60, no. 3, pp. 1912-1928, Jun. 2013.

[38] S. Liu, J. L. Titus, and M. Boden, "Effect of buffer layer on single-event burnout of power DMOSFETs*," IEEE Trans. Nucl. Sci.*, vol. 54, no. 6, pp. 2554-2560, Dec. 2007.

[39] M. N.Darwish, M. A. Shibib, M. R. Pinto, and J. L. Titus, "Single event gate rupture of power DMOS transistors," in *Tech Dig. Int. Electron Devices Meet. (IEDM)*, pp. 671-674, 1993.

[40] M. Allenspach, C. Dachs, G. H. Johnson, R. D. Schrimpf, E. Lorfevre, J.M. Palau, J. R. Brews, K. F. Galloway, J. L. Titus, and C. F.Wheatley, "SEGR and SEB in N-channel power MOSFETs," *IEEE Trans. Nucl. Sci.*, vol. 43, no. 6, pp. 2927-2931, Dec. 1996.

[41] W. Morris, "Latchup in CMOS," *2003 IEEE International Reliability Physics Symposium Proceedings*, 41st Annual., Dallas, TX, USA, pp. 76-84, 2003.

[42] J. M. Hutson, R. D. Schrimpf and L. M. Massengill, "The Effects of Scaling and Well and Substrate Contact Placement on Single Event Latchup in Bulk CMOS Technology," *2005 8th European Conference on Radiation and Its Effects on Components and Systems*, Cap d'Agde, pp. PC24-1-PC24-5, 2005.

[43] J. F. Ziegler, SRIM - The Stopping and Range of Ions in Matter Accessed: Jul. 2019 [Online] Available: http://www.srim.org/.

[44] 88-Inch Cyclotron, Berkeley Accelerator Space Effects [Online] Available at: https://cyclotron.lbl.gov/.

[45] Texas A&M University Cyclotron Institute, Texas A&M University [Online] Available at: https://cyclotron.tamu.edu/.

[46] RADiation Effects Facility, University of Jyväskylä [Online] Available at: https://www.jyu.fi/science/en/physics/research/infrastructures/accelerator-laboratory/radiation-effects-facility.

[47] Cyclotron Resource Centre, Université Catholique de Louvain [Online] Available at: https://uclouvain.be/en/research-institutes/irmp/crc.

[48] D. M. Hiemstra and E. W. Blackmore, “LET Spectra of Proton Energy Levels from 50 to 500 MeV and Their Effectiveness for Single Event Effects Characterization of Microelectronics,” *IEEE Trans. Nucl. Sci.*, vol. 50, no. 6, pp. 2245-2250, Dec. 2003.

[49] S. Kirkpatrick, “Modeling diffusion and collection of charge from ionizing radiation in silicon devices,” *IEEE Trans. Electron Devices*, vol. 26, no. 11, pp. 1742-1753, Nov. 1979.

[50] N. C. Hooten, L. D. Edmonds, W. G. Bennett, J. Ahlbin, N. Dodds, R. A. Reed, R. D. Schrimpf, and R. A. Weller, “The significance of high-level carrier generation conditions for charge collection in irradiated devices,” *IEEE Trans. Nucl. Sci.*, vol. 59, no. 6, pp. 2710-2721, Dec. 2012.

[51] C. M. Hsieh, P. C. Murley, and R. R. O’Brien, “A field-funneling effect on the collection of alpha-particle-generated carriers in silicon devices,” *IEEE Electron Device Lett.*, vol. 2, no. 4, pp. 103-105, Apr. 1981.

[52] C.-M. Hsieh, P. C. Murley, and R. R. O’Brien, “Collection of charge from alpha-particle tracks in silicon devices,” *IEEE Trans. Electron Devices*, vol. 30, no. 6, pp. 686-693, Jun. 1983.

[53] S. Buchner, A. R. Knudson, K. Kang, and A. B. Campbell, “Charge Collection from Focused Picosecond Laser Pulses,” *IEEE Trans. Nucl. Sci.*, vol. 35, no. 6, pp. 1517-1522, Dec. 1988.

[54] M. A. Green and M. Keevers, "Optical Properties of Intrinsic Silicon at 300 K," *Progress in Photovoltaics,* vol. 3, no. 3, pp. 189-192, 1995.

[55] R. W. Boyd, Nonlinear Optics. Elsevier, 2007.

[56] L. R. Ryder, “Simulation of Optical Energy Deposition for Pulsed Laser-Induced Single Event Effects Testing in Microelectronic Devices,” M. S. Thesis, College of Eng., Vanderbilt Univ., Nashville, TN, Feb. 2020. Accessed on: May 18, 2020. [Online] Available: https://ir.vanderbilt.edu/bitstream/handle/1803/9826/RYDER-THESIS-2020.pdf?sequence=1&isAllowed=y

[57] CREOL – The College of Optics & Photonics: Jan. 2021 [Online] Available: https://nlo.creol.ucf.edu/Research.aspx.

[58] Lumerical FDTD: Jan. 2021 [Online] Available: https://www.lumerical.com/tcad-products/fdtd/.

[59] L. D. Ryder, K. L. Ryder, A. L. Sternberg, J. A. Kozub, H. Gong, E. X. Zhang, D. Linten, J. Mitard, R. A. Weller, R. D. Schrimpf, S. M. Weiss, and R. A. Reed, “Polarization Dependence of Pulsed Laser-Induced SEEs in SOI FinFETs,” *IEEE Trans. Nucl. Sci*., vol. 67, no. 1, pp. 38-43, Jan. 2020.

[60] K. L. Ryder, L. D. Ryder, A. L. Sternberg, J. A. Kozub, E. X. Zhang, A. Khachatrian, S. P. Buchner, D. McMorrow, J. M. Hales, Y. Zhao, L. Wang, C. Wang, R. A. Weller, R. D. Schrimpf, S. M. Weiss, and R. A. Reed, “Comparison of Sensitive Volumes Associated with Ion- and Laser-Induced Charge Collection in an Epitaxial Silicon Diode,” *IEEE Trans. Nucl. Sci.,* vol. 67, no. 1, pp. 57-62, Jan. 2020.

[61] S. Buchner, N. Roche, J. Warner, D. McMorrow, F. Miller, S. Morand, V. Pouget, C. Larue, V. Ferlet-Cavrois, F. El Mamouni, H. Kettunen, P. Adell, G. Allen, and D. Aveline, "Comparison of Single Event Transients Generated at Four Pulsed-Laser Test Facilities-NRL, IMS, EADS, JPL," *IEEE Trans. Nucl. Sci.,* vol. 59, no. 4, pp. 988-998, Aug. 2012.

[62] J. M. Hales, A. Khachatrian, S. Buchner, J. Warner, A. Ildefonso, G. N. Tzintzarov, D. Nergui, D. M. Monahan, S. D. LaLumondiere, J. D. Cressler, and D. McMorrow, "New Approach for Pulsed-Laser Testing that Mimics Heavy-Ion Charge Deposition Profiles," *IEEE Trans. Nucl. Sci.,* vol. 67, no. 1, pp. 81-90, Jan. 2020.

[63] S. C. Moss and S. J. Humphrey, "Development of a System for Producing Tightly Focused X-ray Pulsed to Generate Single Event Effects in Microelectronic Devices," *Proc. Eleventh Biennial Single-Event Effects (SEE) Symposium*, pp. 472-488, Apr. 1998.

[64] S. LaLumondiere, "The Current Status and Future Prospects for Pulsed X-ray SEE Testing," *IEEE NSREC Short Course Notebook*, S. C. Moss, Ed., San Antonio, Texas, Jul. 8 2019, Ch. 4B.

[65] Sandia National Laboratories – Ion Beam Laboratory [Online] Available at: https://www.sandia.gov/research/facilities/technology_deployment_centers/ion_beam_lab/.

[66] GSI [Online] Available at: https://www.gsi.de/en/researchaccelerators.htm.

[67] Buenos Aires TANDAR Laboratory [Online] Available at: http://www.tandar.cnea.gov.ar/.

[68] P. Chu, D. L. Hansen, B. L. Doyle, K. Jobe, R. Lopez-Aguado, M. Shoga, and D. S. Walsh, "Ion-Microbeam Probe of High-Speed Shift Registers for SEE Analysis – Part 1: SiGe," *IEEE Trans. Nucl. Sci.*, vol. 53, no. 3, pp. 1574-1582, June 2006.

[69] C. Martinella, T. Ziemann, R. Stark, A. Tsibizov, K. O. Voss, R. G. Alia, Y. Kadi, U. Grossner, and A. Javanainen, "Heavy-Ion Microbeam Studies of Single-Even Leakage Current Mechanism in SiC VD-MOSFETs," *IEEE Trans. Nucl. Sci.*, vol. 67, no. 7, pp. 1381-1389, July 2020.

[70] A. Fontana, S. Pazos, F. Aguirre, N. Vega, N. Müller, E. De la Fourniere, F. Silveria, M. E. Debray, F. Palumbo, "Pulse Quenching and Charge-Sharing Effects on Heavy-Ion Microbeam Induced ASET in a Full-Custom CMOS OpAmp," *IEEE Trans. Nucl. Sci.*, vol. 66, no. 7, pp. 1473-1482, July 2019.

[71] A. H. Johnston, "Charge Generation and Collection in p-n Junctions Excited with Pulsed Infrared Lasers," *IEEE Trans. Nucl. Sci.*, vol. 40, no. 6, pp. 1694-1702, Dec. 1993.

[72] D. McMorrow, W. T. Lotshaw, J. S. Melinger, S. Buchner, and R. L. Pease, "Subbandgap Laser-Induced Single Event Effects: Carrier Generation via Two-Photon Absorption," *IEEE Trans. Nucl. Sci.*, vol. 49, no. 6, pp. 3002-3008, Dec. 2002.

[73] N. C. Hooten, "Characterization of the Two-Photon Absorption Carrier Generation Region in Bulk Silicon Diodes," M. S. Thesis, College of Eng., Vanderbilt Univ., Nashville, TN, Aug. 2011. Accessed on: May 18, 2020. [Online] Available: https://etd.library.vanderbilt.edu/available/etd-07222011-143800/unrestricted/hooten.pdf

[74] D. Cardoza, S. D. LaLumondiere, and W. T. Lotshaw, "Prospects for Single Event Effects Testing with an Ultrashort Pulse X-Ray Apparauts," *Aerospace Technical Report*, ATR-2009(8129)-4, 10 Nov. 2009.

[75] D. M. Cardoza, S. D. LaLumondiere, M. A. Tockstein, S. C. Witczak, Y. Sin, B. J. Foran, W. T. Lotshaw, and S. C. Moss, "Single Event Transients Induced by Picosecond Pulsed X-Ray Absorption in III-V Hererojunction Transistors," *IEEE Trans. Nucl. Sci.*, vol. 59, no. 6, pp. 2729-2738, Dec. 2012.

[76] S. Duzellier, D. Falguere, L. Guibert, V. Pouget, P. Fouillat and R. Ecoffet, "Application of laser testing in study of SEE mechanisms in 16-Mbit DRAMs," *IEEE Trans. Nucl. Sci.*, vol. 47, no. 6, pp. 2392-2399, Dec. 2000.

[77] A. M. Chugg, A. J. Burnell, M. J. Moutrie, R. Jones and R. Harboe-SØrensen, "Laser SEE Sensitivity Mapping of SRAM Cells," *IEEE Trans. Nucl. Sci.*, vol. 54, no. 6, pp. 2106-2112, Dec. 2007.

[78] A. M. Chugg, J. Ward, J. McIntosh, N. Flynn, P. H. Duncan, T. S. Barber, and C. Poivey, "Improved Fine-Scale Laser Mapping of Component SEE Sensitivity," *IEEE Trans. Nucl. Sci.*, vol. 59, no. 4, pp. 1007-1014, Aug. 2012.

[79] N. A. Dodds, N. C. Hooten, R. A. Reed, R. D. Schrimpf, J. H. Warner, N. J.-H. Roche, D. McMorrow, S. Buchner, S. Jordan, J. A. Pellish, W. G. Bennett, N. J. Gaspard, and M. P. King, "SEL-Sensitive Area Mapping and the Effects of Reflection and Diffraction from Metal Lines on Laser SEE Testing," *IEEE Trans. Nucl. Sci.*, vol. 60, no. 4, pp. 2550-2558, Aug. 2013.

[80] D. McMorrow, W. T. Lotshaw, J. S. Melinger, S. Buchner, Y. Boulghassoul, L. W. Massengill, and R. L. Pease, "Three-Dimensional Mapping of Single-Event Effects Using Two Photon Absorption," *IEEE Trans. Nucl. Sci.*, vol. 50, no. 6, pp. 2199-2207, Dec. 2003.

[81] D. McMorrow, S. Buchner, W. T. Lotshaw, J. S. Melinger, M. Maher, and M. W. Savage, "Demonstration of Single-Event Effects Induced by Through-Wafer Two-Photon Absorption," *IEEE Trans. Nucl. Sci.*, vol. 51, no. 6, pp. 3553-3557, Dec. 2004.

[82] D. M. Cardoza, S. D. LaLumondiere, M. A. Tockstein, S. C. Witczak, Y. Sin, B. J. Foran, W. T. Lotshaw, and S. C. Moss, "Single Event Transients Induced by Picosecond Pulsed X-Ray Absorption in III-V Heterojunction Transistors," *IEEE Trans. Nucl. Sci.*, vol. 59, no. 6, pp. 2729-2738, Dec. 2012.

[83] S. P. Buchner, F. Miller, V. Pouget, and D. P. McMorrow, "Pulsed-Laser Testing for Single-Event Effects Investigations," *IEEE Trans. Nucl. Sci.*, vol. 60, no. 3, pp. 1852-1875, June 2013.

[84] D. Cardoza, S. D. LaLumondiere, N. P. Wells, M. A. Tockstein, D. L. Brewe, W. T. Lotshaw, and S. C. Moss, "Investigating Pulsed X-ray Induced SEE in Analog Microelectronic Devices," *IEEE Trans. Nucl. Sci.*, vol. 62, no. 6, pp. 2458-2467, Dec. 2015.

[85] Y. P. Chen, T. D. Loveless, A. L. Sternberg, E. X. Zhang, J. S. Kauppila, B. L. Bhuva, W. T. Holman, M. L. Alles, R. A. Reed, D. McMorrow, R. D. Schrimpf, and L. W. Massengill, "Persistent Laser-Induced Leakage in a 20 nm Charge-Pump Phase-Locked Loop (PLL)," *IEEE Trans. Nucl. Sci.*, vol. 64, no. 1, pp. 512-518, Jan. 2017.

[86] H. Gong, K. Ni, E. X. Zhang, A. L. Sternberg, J. A. Kozub, K. L. Ryder, R. F. Keller, L. D. Ryder, S. M. Weiss, R. A. Weller, M. L. Alles, R. A. Reed, D. M. Fleetwood, R. D. Schrimpf, A. Vardi, and J. A. del Alamo, "Scaling Effects on Single-Event Transients in InGaAs FinFETs," *IEEE Trans. Nucl. Sci.*, vol. 65, no. 1, pp. 296-303, Jan. 2018.

[87] A. Khachatrian, N. J-H Roche, S. P. Buchner, A. D. Koehler, T. J. Anderson, D. McMorrow, S. D. LaLumondiere, J. P. Bonsall, E. C. Dillingham, and D. L. Brewe, "Investigation of Single-Event Transients in AlGaN/GaN MIS-Gate HEMTs Using a Focused X-Ray Beam," *IEEE Trans. Nucl. Sci.*, vol. 66, no. 1, pp. 368-375, Jan. 2019.

[88] C. Liang, R. Ma, K. Li, Y. Su, H. Gong, K. L. Ryder, P. Wang, A. L. Sternberg, E. X. Zhang, M. L. Alles, R. A. Reed, S. J. Koester, D. M. Fleetwood, and R. D. Schrimpf, "Laser-Induced Single-Event Transients in Black Phosphorus MOSFETs," *IEEE Trans. Nucl. Sci.*, vol. 66, no. 1, pp. 384-388, Jan. 2019.

[89] R. A. Johnson, A. F. Witulski, D. R. Ball, K. F. Galloway, A. L. Sternberg, E. Zhang, L. D. Ryder, R. A. Reed, R. D. Schrimpf, J. A. Kozub, J.-M. Lauenstein, and A. Javanainen, "Enhanced Charge Collection in SiC Power MOSFETs Demonstrated by Pulse-Laser Two-Photon Absorption SEE Experiments *IEEE Trans. Nucl. Sci.*, vol. 66, no. 7, pp. 1694-1701, July 2019.

[90] D. Nergui, A. Ildefonso, G. N. Tzintzarov, A. Omprakash, Z. E. Fleetwood, S. D. LaLumondiere, D. M. Monahan, J. P. Bonsall, H. Kettering, D. L. Brewe, and J. D. Cressler, "Single-Event Transients in SiGe HBTs Induced by Pulsed X-ray Microbeam," IEEE Trans. Nucl. Sci., vol. 67, no. 1, pp.91-98, Jan. 2020.

[91] R. L. Pease, A. L. Sternberg, Y. Boulghassoul, L. W. Massengill, S. Buchner, D. McMorrow, D. S. Walsh, G. L. Hash, and S. D. LaLumondiere, "Comparison of SETs in Bipolar Linear Circuits Generated with an Ion Microbeam, Laser Light, and Circuit Simulation," *IEEE Trans. Nucl. Sci.*, vol. 49, no. 6, pp. 3163-3170. Dec. 2002.

[92] F. Miller, N. Buard, T. Carrière, R. Dufayel, R. Gaillard, P. Poirot, J.-M. Palau, B. Sagnes, and P. Fouillat, "Effects of Beam Spot Size on the Correlation Between Laser and Heavy Ion SEU Testing," *IEEE Trans. Nucl. Sci.*, vol. 51, no. 6, pp. 3708-3715, Dec. 2004

[93] D. Cardoza, S. D. LaLumondiere, M. A. Tockstein, D. L. Brewe, N. P. Wells, R. Koga, K. M. Gaab, W. T. Lotshaw, and S. C. Moss, "Comparison of Single Event Transients Generated by Short Pulsed X-Rays, Lasers, and Heavy Ions," *IEEE Trans. Nucl. Sci.*, vol. 61, no. 6, pp. 3154-3162, Dec. 2014.

[94] A. Khachatrian, N. J-H. Roche, S. P. Buchner, A. D. Koehler, T. J. Anderson, J. H. Warner, P. D. Cunningham, J. S. Melinger, D. McMorrow, S. D. LaLumondiere, N. P. Wells, M. A. Tockstein, D. L. Brewe, E. C. Dillingham, J. P. Bonsall, P. Karuza, W. T. Lotshaw, and S. C. Moss, "Comparison of single event transients in AlGan/GaN Schottky-gate and MIS-gate HEMTs using single-photon absorption and focused X-ray techniques," *16th European Conference on Radiation and Its Effects on Components and Systems (RADECS)*, Bremen, pp. 1-4, 2016.

[95] A. Khachatrian, N. J-H Roche, S. Buchner, A. D. Koehler, T. J. Anderson, K. D. Hobart, D. McMorrow, S. D. LaLumondiere, N. P. Wells, M. A. Tockstein, E. C. Dillingham, J. P. Bonsall, P. Karuza, W. T. Lotshaw, S. C. Moss, D. L. Brewe, V. Ferlet-Cavrois, and M. Mushitiello, "Comparison of Single Event Transients in AlGaN/GaN Schottky-Gate HEMTs Using Four Sources for Charge Injection," *2017 17th European Conference on Radiation and Its Effects on Components and Systems (RADECS)*, Geneva, Switzerland, pp. 1-4, 2017.

[96] A. Ildefonso, G. N. Tzintzarov, D. Nergui, A. P. Omprakash, P. S. Goley, J. M. Hales, A. Khachatrian, S. P. Buchner, D. McMorrow, J. H. Warner, and J. D. Cressler, "Comparison of Single-Event Transients in SiGe HBTs on Bulk and Thick-Film SOI," *IEEE Trans. Nucl. Sci.*, vol. 67, no. 1, pp. 71-80, Jan. 2020.

[97] J. M. Hales, D. McMorrow, N. J-H Roche, A. Khachatrian, J. H. Warner, S. P. Buchner, J. S. Melinger, J. W. Perry, W. T. Lotshaw, and V. Dubikovsky, "Simulation of Light-Matter Interaction and Two-Photon Absorption Induced Charge Deposition by Ultrashort Optical Pulsed in Silicon," *IEEE Trans. Nucl. Sci.*, vol. 61, no. 6, pp. 3504-3511, Dec. 2014.

[98] J. M. Hales, A. Khachatrian, N. J-H. Roche, J. H. Warner, S. P. Buchner, and D. McMorrow, "Simulation of Light-Based Two-Photon Absorption Induced Charge Carrier Generation in Silicon," *IEEE Trans. Nucl. Sci.*, vol. 62, no. 4, pp. 1550-1557, Aug. 2015.

[99] J. M. Hales, N. J-H. Roche, A. Khachatrian, D. McMorrow, S. Buchner, J. Warner, M. Turowski, K. Lilja, N. C. Hooten, E. X. Zhang, R. A. Reed, and R. D. Schrimpf, "Two-Photon Absorption Induced Single-Event Effects: Correlation Between Experiment and Simulation," *IEEE Trans on Nucl. Sci.*, vol. 62, no. 6, pp. 2867-2873, Dec. 2015.

[100] Z. E. Fleetwood, N. E. Lourenco, A. Ildefonso, J. H. Warner, M. T. Wachter, J. M. Hales, G. N. Tzintzarov, N. J. Roche, A. Khachatrian, S. P. Buchner, D. McMorrow, P. Paki, and J. D. Cressler, "Using TCAD Modeling to Compare Heavy-Ion and Laser-Induced Single Event Transients in SiGe HBTs," *IEEE Trans. Nucl. Sci.*, vol. 64, no. 1, pp. 398-405, Jan. 2017.

[101] J. M. Hales, N. J-H. Roche, A. Khachatrian, D. McMorrow, S. Buchner, J. Warner, M. Turowski, K. Lilja, N. C. Hooten, E. X. Zhang, R. A. Reed, and R. D. Schrimpf, "Strong Correlation Between Experiment and Simulation for Two-Photon Absorption Induced Carrier Generation," *IEEE Trans. Nucl. Sci.*, vol. 64, no. 5, pp.1133-1136, May 2017.

[102] J. M. Hales, A. Khachatrian, S. Buchner, N. J-H. Roche, J. Warner, and D. McMorrow, "A Simplified Approach for Predicting Pulsed-Laser-Induced Carrier Generation in Semiconductors," *IEEE Trans. Nucl. Sci.*, vol. 64, no. 3, pp. 1006-1013, Mar. 2017.

[103] J. M. Hales, A. Khachatrian, S. Bucnher, N. J. Roche, J. Warner, Z. E. Fleetwood, A. Ildefonso, J. D. Cressler, V. Ferlet-Cavrois, and D. McMorrow, "Experimental Validation of an Equivalent LET Approach for Correlating Heavy-Ion and Laser-Induced Charge Deposition," *IEEE Trans. Nucl. Sci.*, vol. 65, no. 8, pp. 1724-1733, Aug. 2018.

[104] A. Ildefonso, Z. E. Fleetwood, G. N. Tzintzarov, J. M. Hales, D. Nergui, M. Frounchi, A. Khachatrian, S. P. Buchner, D. McMorrow, J. H. Warner, J. Harms, A. Erickson, K. Voss, V. Ferlet-Cavrois, and J. D. Cressler, "Optimizing Optical Parameters to Facilitate Correlation of Laser- and Heavy-Ion-Induced Single-Event Transients in SiGe HBTs," *IEEE Trans. Nucl. Sci.*, vol. 66, no. 1, pp. 359-367, Jan. 2019.

[105] K. L. Ryder, L. D. Ryder, A. L. Sternberg, J. A. Kozub, E. X. Zhang, S. D. LaLumondiere, D. M. Monahan, J. P. Bonsall, A. Khachatrian, S. P. Buchner, D. McMorrow, J. M. Hales, Y. Zhao, L. Wang, C. Wang, R. A. Weller, R. D. Schrimpf, S. M. Weiss, and R. A. Reed, "Comparison of Single Event Transients in an Epitaxial Silicon Diode Resulting from Heavy Ion-, Focused X-Ray-, and Pulsed Laser-Induced Charge Generation," *IEEE Trans. Nucl. Sci.*, vol. 68, no. 5, pp. 626-633, May 2021.

[106] Synopsys TCAD Accessed: Mar. 2021 [Online] Available: https://www.synopsys.com/silicon/tcad.html.

[107] K. L. Ryder, "Comparison of Heavy Ion- and Laser-Induced Sensitive Volumes in an Epitaxial Silicon Diode," M. S. Thesis, College of Eng., Vanderbilt Univ., Nashville, TN, Sept. 2019. Accessed: January 2021. [Online] Available: https://etd.library.vanderbilt.edu/available/etd-08292019-114750/unrestricted/KLR_Masters_formatted.pdf

[108] F. B. McLean and T. R. Oldham, "Charge Funneling in N- and P-Type Si Substrates," *IEEE Trans. Nucl. Sci.*, vol. NS-29, no. 6, pp. 2018-2023, Dec. 1982.

[109] K. W. Golke, “Determination of Funnel Length from Cross Section versus LET Measurements,” *IEEE Trans. Nucl. Sci.*, vol. 40, no. 6, pp. 1910-1917, Dec. 1993.

[110] I. K. Samsel, E. X. Zhang, N. C. Hooten, E. D. Funkhouser, W. G. Bennett, R. A. Reed, R. D. Schrimpf, M. W. McCurdy, D. M. Fleetwood, R. A. Weller, G. Vizkelethy, X. Sun, T.-P. Ma, O. I. Saadat, and T. Palacios, "Charge Collection Mechanisms in AlGaN/GaN Mos High Electron Mobility Transistors," *IEEE Trans. Nucl. Sci.*, vol. 60, no. 6, pp. 4439-4445, Dec. 2013

[111] J. A. Pellish, R. A. Reed, D. McMorrow, G. Vizkelethy, V. F. Cavrois, J. Baggio, P. Paillet, O. Duhamel, K. A. Moen, S. D. Phillips, R. M. Diestelhorst, J. D. Cressler, A. K. Sutton, A. Raman, M. Turowski, P. E. Dodd, M. L. Alles, R. D. Schrimpf, P. W. Marshall, and K. A. Label, “Heavy ion microbeam- and broadbeam-induced transients in SiGe HBTs,” *IEEE Trans. Nucl. Sci.*, vol. 56, no. 6, pp. 3078-3084, Dec. 2009.

[112] A. Khachatrain, N. J.-H. Roche, D. McMorrow, J. H. Warner, S. P. Buchner, and J. S. Melinger, “A Dosimetry Methodology for Two-Photon Absorption Induced Single-Event Effects Measurements,” *IEEE Trans. Nucl. Sci.*, vol. 61, no. 6, pp. 3416-3423, Dec. 2014.

[113] Sentaurus Device User Guide, Version G-2012.06, June 2012.

[114] Tektronix, private communication, Apr. 2018.

[115] J. C. Pickel and J. T. Blandford Jr., “Cosmic ray induced errors in MOS memory cells,” *IEEE Trans. Nucl. Sci.*, vol. 25, no. 6, pp. 1166-1171, Dec. 1978.

[116] E. L. Petersen, “Predictions and observations of SEU rates in space,” *IEEE Trans. Nucl. Sci.*, vol. 44, no. 6, pp. 2174-2187, Dec. 1997.

[117] B. D. Sierawski, J. A. Pellish, R. A. Reed, R. D. Schrimpf, K. M. Warren, R. A. Weller, M. H. Mendenhall, J. D. Black, A. D. Tipton, M. A. Xapsos, R. C. Baumann, X. Deng, M. J. Campola, M. R. Friendlich, H. S. Kim, A. M. Phan, and C. M. Seidleck, "Impact of Low-Energy Proton Induced Upsets on Test Methods and Rate Predictions," *IEEE Trans. Nucl. Sci.*, vol. 56, pp. 3085-3092, Dec. 2009.

[118] K. M. Warren, R. A. Weller, B. D. Sierawski, R. A. Reed, M. H. Mendenhall, R. D. Schrimpf, L. W. Massengill, M. E. Porter, J. D. Wilkinson, K. A. LaBel, and J. H. Adams, "Application of RADSAFE to Model the Single Event Upset Response of a 0.25 um CMOS SRAM," *IEEE Trans. Nucl. Sci.*, vol. 54, pp. 898-903, Aug. 2007.

[119] A. J. Tylka, J. H. Adams, Jr., P. R. Boberg, B. Brownstein, W. F. Dietrich, E. O. Flueckiger, E. L. Petersen, M. A. Shea, D. F. Smart, and E. C. Smith, "CRÈME96: A Revision of the Cosmic Ray Effects on Micro-Electronics Code," *IEEE Trans. Nucl. Sci.*, vol. 4, no. 6, pp. 2150-2160, Dec. 1997.

[120] M. H. Mendenhall and R. A. Weller, "A probability-conserving cross-section biasing mechanism for variance reduction in Monte Carlo particle transport calculations," *Nucl. Inst. & Meth. A*, vol. 667, pp. 38-43, Mar. 2012, doi:10.1016/j.nima.2.

APPENDIX A – SET CHARACTERISTICS PROCESSING CODE

```
def dblexp(tv,td1,tau1,tau2,I,off,bias):
    y = []
    for t in tv:
        try:
            i1 = math.exp(-tau1*(t-td1))-math.exp(-tau2*(t-td1))
            if t<td1:
                y.append(off+t*bias)
            else:
                y.append(off+t*bias+I*i1)
        except OverflowError:
            y.append(0.0)
    return y

def fitDouble(x,y,w1,w2,w3,w4):
    try:
        popt, pcov = curve_fit(
                    dblexp, x,y,p0=[w1,w2,w3,w4,0.0,0.0],maxfev=5000,method='lm',factor=0.1)
        perr = np.sqrt(np.diag(pcov))
        c1,c2,c3,c4,c5,c6=popt
        fits = perr[0]
    except RuntimeError:
        c1 = w1
        c2 = w2
        c3 = w3
        c4 = w4
        c5 = 0.0
        c6 = 0.0
        fits = 1.0
    return c1,c2,c3,c4,c5,c6

def charge_coll(x,y,off,bias):
    charge   = 0.0
    temp  = 0.0
    for i in range(0,len(y)-1):
        charge   = charge + (0.5*(x[i+1]-x[i])*(y[i+1]+y[i]))
        temp  = temp + (0.5*(x[i+1]-x[i])*((off+x[i+1]*bias)+(off+x[i]*bias)))
    charge = charge-temp
    return charge




def riseTime(a,b):
    pc     = np.max(y1)
    j      = np.argmax(y1)
```

```
    rise_lb = 0.0
    for i in range(0,j):
        diff = y1[i]-(0.01*pc)
        if ((diff==0) or (diff*(y1[i+1]-(0.01*pc))<0)):
            rise_lb = x1[i]
    rise_time = rise_lb-x1[j]
    return rise_time

def fallTime(x1,y1):
    pc      = np.max(y1)
    j       = np.argmax(y1)
    fall_rb = 0.0
    for i in range(j,len(y1)-1):
        diff = y1[i]-(0.01*pc)
        if ((diff==0) or (diff*(y1[i+1]-(0.01*pc))<0)):
            fall_rb = x1[i]
    fall_time = fall_rb-x1[j]
    return fall_time

def fwhm(x1,y1):
    pc      = np.max(y1)
    j       = np.argmax(y1)
    fwhm_lb = 0.0
    fwhm_rb = 0.0
    for i in range(0,j):
        diff = (0.5*pc)-y1[i]
        if ((diff==0) or (diff*(0.5*pc-y1[i+1])<0)):
            fwhm_lb = x1[i]
    for i in range(j,len(y1)-1):
        diff = (0.5*pc)-y1[i]
        if ((diff==0) or (diff*(0.5*pc-y1[i+1])<0)):
            fwhm_rb = x1[i]
    fwhm_time = fwhm_rb-fwhm_lb
    return fwhm_time

def r_squared(y,y_fit):
    ss_res     = np.sum((y-y_fit)**2)
    ss_tot     = np.sum((y-np.mean(y))**2)
    r2     = 1.0 - (ss_res/ss_tot)
    return r2
```

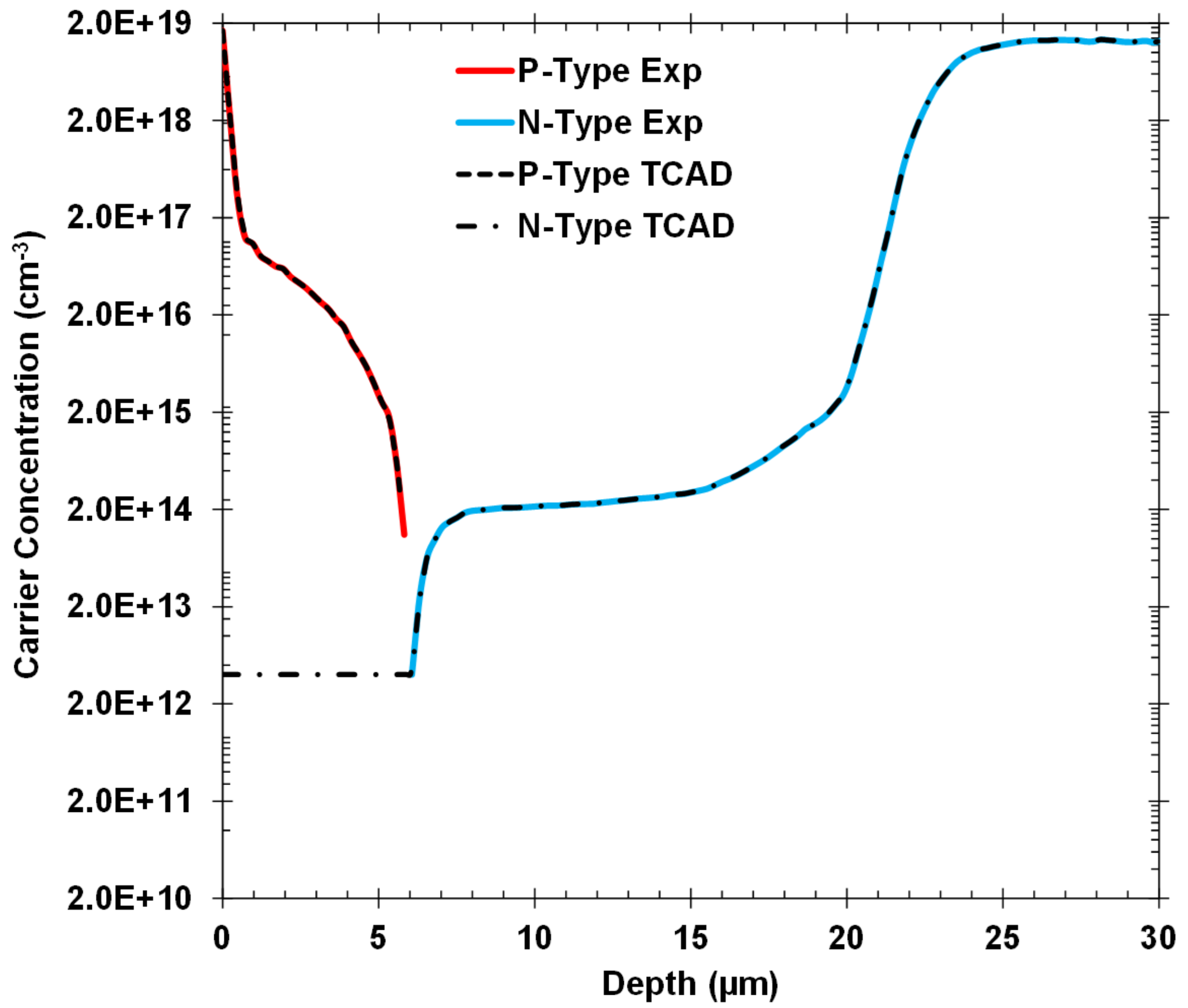
P-Type Exp
N-Type Exp
P-Type TCAD
N-Type TCAD
Carrier Concentration (cm-3)
2.0E+19
2.0E+18
2.0E+17
2.0E+16
2.0E+15
2.0E+14
2.0E+13
2.0E+12
2.0E+11
2.0E+10
0
5
10
15
20
25
30
Depth (μm)

From [113], Sentaurus Device User Guide, Version G-2012.06, June 2012.

Table 46 Philips unified mobility model: Electron and hole parameters (silicon)

Symbol	Parameter name	Electrons (arsenic)	Electrons (phosphorus)	Holes (boron)	Unit
μ_{max}	mumax_*	1417	1414	470.5	cm^2/Vs
μ_{min}	mumin_*	52.2	68.5	44.9	cm^2/Vs
θ	theta_*	2.285	2.285	2.247	1
$N_{\{e,h\},ref}$	n_ref_*	9.68×10^{16}	9.2×10^{16}	2.23×10^{17}	cm^{-3}
α	alpha_*	0.68	0.711	0.719	1

Page 314.

Table 63 Default parameters for doping- and temperature-dependent SRH lifetime

Symbol	Parameter name	Electrons	Holes	Unit
τ_{min}	taumin	0	0	s
τ_{max}	taumax	1×10^{-5}	3×10^{-6}	s
N_{ref}	Nref	1×10^{16}	1×10^{16}	cm^{-3}
γ	gamma	1	1	1
T_α	Talpha	–1.5	–1.5	1
C	Tcoeff	2.55	2.55	1
E_{trap}	Etrap	0	0	eV

Page 363.

Table 65 Default coefficients of Auger recombination model

Symbol	A_A [cm^6s^{-1}]	B_A [cm^6s^{-1}]	C_A [cm^6s^{-1}]	H [1]	N_0 [cm^{-3}]
Parameter name	A	B	C	H	N0
Electrons	6.7×10^{-32}	2.45×10^{-31}	-2.2×10^{-32}	3.46667	1×10^{18}
Holes	7.2×10^{-32}	4.5×10^{-33}	2.63×10^{-32}	8.25688	1×10^{18}

Page 376.

Table 67 Coefficients for Okuto–Crowell model (Eq. 372)

Symbol	Parameter name	Electrons	Holes	Unit
a	a	0.426	0.243	V^{-1}
b	b	4.81×10^{5}	6.53×10^{5}	V/cm
c	c	3.05×10^{-4}	5.35×10^{-4}	K^{-1}
d	d	6.86×10^{-4}	5.67×10^{-4}	K^{-1}
γ	gamma	1	1	1
δ	delta	2	2	1

Page 379.

Table 102 Coefficients for carrier generation by heavy ion (HeavyIon parameter set)

	s_{hi}	a_1	a_2	a_3	a_4	k	c_1	c_2	c_3	c_4
Keyword	s_hi	a_1	a_2	a_3	a_4	k_hi	c_1	c_2	c_3	c_4
Default value	2e-12	0	0	0	0	1	0	1	0	1
Default unit	s	pairs/cm^3	pairs/cm^3/cm	pairs/cm^3	cm^{-1}	1	pairs/cm^3	1	cm^{-1}	1
Unit if PicoCoulomb is chosen	s	pairs/cm^3	pairs/cm^3/μm	pairs/cm^3	μm^{-1}	1	pC/μm	1	μm^{-1}	1

Page 577.